Aerodynamic and aeroelastic characteristics of cable-supported bridges with roadway wind barriers

Buljac, Andrija

University of Zagreb

Faculty of Mechanical Engineering and Naval Architecture

Andrija Buljac

AERODYNAMIC AND AEROELASTIC CHARACTERISTICS OF CABLE-SUPPORTED BRIDGES WITH ROADWAY WIND BARRIERS

PhD thesis

Zagreb, 2019

University of Zagreb

Faculty of Mechanical Engineering and Naval Architecture

Andrija Buljac

AERODYNAMIC AND AEROELASTIC CHARACTERISTICS OF CABLE-SUPPORTED BRIDGES WITH ROADWAY WIND BARRIERS

PhD thesis

Supervisors:

Prof. Hrvoje Kozmar, PhD

Prof. Stanislav Pospíšil, PhD

Zagreb, 2019

Sveučilište u Zagrebu

Fakultet strojarstva i brodogradnje

Andrija Buljac

AERODINAMIČKA I AEROELASTIČNA SVOJSTVA VISEĆIH I OVJEŠENIH MOSTOVA S CESTOVNIM VJETROBRANIMA

Doktorski rad

Mentori:

Prof. dr. sc. Hrvoje Kozmar

Prof. dr. sc. Stanislav Pospíšil

Zagreb, 2019.

BIBLIOGRAPHY DATA

Keywords:	Cable-supported bridges; roadway wind barriers; aerodynamic forces and moments; flutter; galloping; wind-tunnel experiments.
Scientific area:	Technical sciences
Scientific field:	Mechanical Engineering
Institution:	Faculty of Mechanical Engineering and Naval Architecture (FMENA), University of Zagreb
Supervisors:	Prof. Hrvoje Kozmar, PhD Prof. Stanislav Pospíšil, PhD
Number of pages:	127
Number of figures:	56
Number of tables:	4
Number of references:	93
Date of oral examination:	01.07.2019.
Jury members:	Prof. Zdravko Virag, PhD Prof. Ivica Kožar, PhD Prof. Ahsan Kareem, PhD
Archive:	FMENA, University of Zagreb

:

Preface

This thesis was developed in collaboration of the Faculty of Mechanical Engineering and Naval Architecture, University of Zagreb, Croatia and the Institute of Theoretical and Applied Mechanics in Prague, Czech Republic. The experiments were performed in the climatic boundary-layer wind tunnel of the Institute of Theoretical and Applied Mechanics in Prague, Czech Republic.

The thesis is based on the following journal articles:

Buljac A., Kozmar H., Pospíšil S. and Macháček M. (2017) Flutter and galloping of cable-supported bridges with porous wind barriers. Journal of Wind Engineering and Industrial Aerodynamics 171, 304-318.

Buljac A., Kozmar H., Pospíšil S. and Macháček M. (2017) Aerodynamic and aeroelastic characteristics of typical bridge decks equipped with wind barriers at the windward bridge-deck edge. Engineering Structures 137, 310-322.

Pospíšil S., Buljac A., Kozmar H., Kuznetsov S., Macháček M. and Král R. (2017) Influence of stationary vehicles on bridge aerodynamics and aeroelasticity. Journal of Bridge Engineering 22, 05016012-1-05016012-13.

Buljac A., Kozmar H., Pospíšil S., Macháček M. and Kuznetsov S. (2019) Effects of wind-barrier layout and wind turbulence on aerodynamic stability of cable-supported bridges. Submitted.

Acknowledgement

The support of the Croatian Science Foundation and the Erasmus+ program is gratefully acknowledged.

I would like to express my sincere gratitude to my advisors Professor Hrvoje Kozmar and Professor Stanislav Pospíšil for their valuable advices, support and companionship in performing this research and writing the thesis. They are not only my supervisors, but also dear colleagues and friends. I am also thankful to the examiners of the thesis, Professor Zdravko Virag (University of Zagreb), Professor Ivica Kožar (University of Rijeka) and Professor Ahsan Kareem (University of Notre Dame), for their valuable comments and suggestions.

I wish to express my great appreciation to Professor Sergey Kuznetsov, Head of the wind-tunnel facility of the Institute of Theoretical and Applied Mechanics in Prague (ITAM), Czech Republic, where the laboratory experiments were performed. He offered support and guidance with respect to wind-tunnel experiments and was a great friend during my research stays at ITAM. A special thanks to the ITAM technical staff, Ing. Pavel Ondrák, Ing. Pavel Chvátal and Radek Čábel, for their support concerning the experiments.

I like to extend my gratitude to a group of colleagues and friends: Marušić, Luks, Tigar, and Mihael. It needs to be mentioned though that our joint coffee breaks were taking me away from work. I am also thankful for the valuable advices and conversations with colleagues and friends from the office: Vedrana, Mihael and Ivan.

Finally, I wish to express love and gratitude to my family - mother Sanka, father Perica, sister Ružica, brother Ante as well as to my fiancée Jelena and lifelong friends for their unconditional love and support.

Contents

Contents iii

Abstract vi

Prošireni sažetak viii

List of Figures xv

List of Tables xix

List of Symbols xx

Introduction 1

1.1. Design of cable-supported bridges 2

1.2. Wind effects on cable-supported bridges 3

1.2.1. Wind characteristics around cable-supported bridges 3

1.2.2. Aerodynamic loading of cable-supported bridges 4

1.2.3. Aeroelasticity of cable-supported bridges 5

1.2.4. Vortex-Induced-Vibration 6

1.2.5. Galloping instability 7

1.2.6. Flutter instability 8

1.3. State-of-the-art of wind effects on cable-supported bridges 10

1.4. Research objectives and hypotheses 15

Mathematical models for wind effects on cable-supported bridges 16

2.1. Aerodynamic forces and moments 17

2.2. Galloping 18

2.3. Flutter 21

2.4. Dynamic response identification 28

2.5. Eigenvalue analysis of the bridge-wind system 30

Experimental setup.....32

3.1. Wind tunnel.....33

3.2. Bridge-deck section and wind-barrier models.....34

3.3. Flow measurements.....39

3.4. Aerodynamic force and moment measurements 41

3.5. Aeroelastic dynamic measurements.....44

Experimental results and discussion.....52

4.1. Flow characteristics around bridge-deck section models.....53

4.1.1. Mean velocity field around bridge-deck sections.....53

4.1.2. Vorticity field around bridge-deck sections.....58

4.2. Aerodynamic forces and the pitch moment acting on bridge-deck sections ..63

4.2.1. Effects of wind-barrier height and porosity on aerodynamic forces and the pitch moment of bridge-deck sections.....63

4.2.2. Effects of wind-barrier arrangement on aerodynamic forces and the pitch moment of bridge-deck sections.....71

4.3. Galloping stability of bridge-deck sections with wind barriers.....76

4.4. Flutter sensitivity of bridge-deck sections with wind barriers 78

4.4.1. Effects of wind-barrier height and porosity on flutter sensitivity of bridge-deck sections with wind barriers.....78

4.4.2. Effects of wind-barrier arrangement on flutter sensitivity of bridge-deck sections with wind barriers.....90

4.4.3. Critical flow velocity for bridge-deck flutter.....95

4.4.4. Effects of incident flow turbulence on flutter sensitivity of bridge-deck sections with wind barriers.....102

Conclusions..... 105

References 108

Curriculum vitae 117

Bibliography 118

Appendix 121

Abstract

Strong cross-winds on bridges and viaducts may cause dynamic instabilities for passing vehicles. To protect vehicles from those adverse cross-wind effects, wind barriers are commonly placed on bridges. While these barriers proved to be successful in sheltering vehicles from cross-winds, their influence on bridge aerodynamic and aeroelastic characteristics is still fairly unknown. This is particularly important for long-span cable-supported bridges that are susceptible to dynamic instabilities due to wind effects.

Hence, the present thesis focuses on the effects of wind barriers on aerodynamic characteristics of three typical long-span cable-supported bridge decks and their sensitivity to self-excited vibrations. Experiments were carried out in the climatic boundary-layer wind tunnel of the Institute of Theoretical and Applied Mechanics in Prague, Czech Republic. Experiments were performed on sectional models of the Golden Gate Bridge (USA), Kao-Pin Hsi Bridge (Taiwan), and Great Belt Bridge (Denmark). Wind-barrier models of different porosities and heights were placed at the bridge-deck section models in various arrangements (windward, leeward and both windward and leeward). Flow characteristics around bridge-deck section models and their average aerodynamic loads (drag force, lift force and pitch moment) were determined for various flow incidence angles. Galloping instability was analyzed using the quasi-steady approach. Flutter sensitivity was studied via dynamic free-vibration tests and eigenvalue analysis of a two-degree-of-freedom system.

The obtained results generally indicate a substantial influence of wind barriers on aerodynamic loads and stability of studied bridge decks.

The drag force coefficient increases as the porosity of the wind barrier decreases, and as the height of the wind barrier increases. Wind barriers change the trends and absolute values of the lift force coefficient of bridge decks, which is more exhibited for more solid and higher wind barriers. The pitch moment of bridge decks decreases when the wind barriers are in place, while the influence of the porosity is more dominant than the wind-barrier height.

The effects of wind barriers on galloping vibration of bridge-deck sections are rather negligible; however, bridge decks become quite prone to flutter when wind barriers are in place. For the windward wind barrier only, flutter susceptibility of bridge decks is more

exhibited for less-porous wind barriers. The effects of increasing wind-barrier height are not unambiguous, as they are simultaneously influenced by the aerodynamic shape of bridge-deck sections.

The wind-barrier arrangement has a major influence as well. For the configurations with the windward wind barrier only as well as both windward and leeward wind barriers, the flutter sensitivity of bridge decks increases substantially, as the critical flow velocity for bridge-deck flutter in those experiments decreased significantly in comparison with the respective empty bridge-deck sections. For the leeward wind barrier only, the flutter susceptibility of bridge-deck sections did not change and remained the same as it was for the empty bridge-deck sections.

Keywords:
Cable-supported bridges; roadway wind barriers; aerodynamic forces and moments; flutter; galloping; wind-tunnel experiments.

Prošireni sažetak

Snažni bočni vjetrovi mogu uzrokovati dinamičku nestabilnost vozila na mostovima, prevrnuti vozila ili uzrokovati sudar s drugim vozilima. Da bi se vozila zaštitila od utjecaja bočnog vjetra, na mostove se postavljaju zaštitni vjetrobrani. Prethodno je pokazano da vjetrobrani uspješno štite vozila od bočnog vjetra na mostovima, ali njihov utjecaj na aerodinamička i aeroelastična svojstva mostova dosad nije istražen, što je izrazito bitno ispitati za viseće i ovješene koji su karakterizirani niskim vlastitim frekvencijama i malim mehaničkim prigušenjem i time izuzetno osjetljivi na djelovanje vjetra.

Djelovanje vjetra na mostove se ispituju u okviru aerodinamike i aeroelastičnosti, koja se bavi međudjelovanjem elastičnih, inercijskih i aerodinamičkih sila koje djeluju na sekcije mosta izložene strujanju zraka. Utjecaj vjetra na mostove se nije posebno pučavao sve do urušavanja mosta Tacoma Narrows u SAD-u u studenom 1940. godine. Nakon tada provedene analize dokazano je da se most urušio zbog vibracija uzorokovanih djelovanja vjetra, pa su se ispitivanja aeroelastičnih svojstava mostova od tada počela provoditi kod projektiranja mostova. Vibracije uzrokovane gibanjem tijela uslijed puhanja vjetra su najčešći oblik vibracija kod mostova. Ova vrsta nestabilnosti može se podijeliti na treperenje (engl. *flutter*) i galopiranje (engl. *galloping*).

Treperenje mosta nastaje uslijed djelovanja pulzirajućih aerodinamičkih sila koje unose energiju u dinamički sustav mosta pri svakoj oscilaciji, pri čemu se treperenje umanjuje mehaničkim prigušenjem sustava. Kada se ostvari kritična brzina strujanja zraka, ukupno prigušenje (suma mehaničkog prigušenja konstrukcije i aerodinamičkog prigušenja uslijed utjecaja vjetra) postiže nultu vrijednost, te sustav postaje dinamički nestabilan. Ako brzina strujanja zraka postane veća od kritične, postiže se negativno ukupno prigušenje, te svaka daljnja pobuda sustava rezultira divergentnim oscilacijama sekcije mosta.

Galopiranje je dinamička nestabilnost tipična za vitke sekcije mosta s pravokutnim ili 'D' poprečnim presjekom, gdje ne dolazi do ponovnog nalijeganja struje zraka na površinu sekcije mosta nakon što se struja zraka prvotno odvojila od mosta na uzvodnom naletnom bridu sekcije mosta. Ova nestabilnost u smjeru okomitom (vertikalnom) na glavni smjer strujanja vjetra uobičajeno ima nisku frekvenciju i relativno velike amplitude oscilacija. Galopiranje se od vibracija uslijed odvajanja vrtloga (engl. *Vortex-Induced-Vibration, VIV*) razlikuje u

tomu što se potonje javljaju kod točno određene brzine strujanja kada se frekvencija odvajanja vrtloga struje zraka izjednači s vlastitom frekvencijom sekcije mosta., engl. *lock-in*. Lock-in vibracije su prisutne samo u uskom području frekvencija i iščezavaju s daljnim povećanjem brzine strujanja zraka, dok se vibracije kod pojave galopiranja nastavljaju povećavati s povećanjem brzine vjetra. Analiza treperenja sekcije mosta zahtijeva proučavanje dinamičkog odziva mosta, a galopiranje se uobičajeno proučava kao kvazistacionarna pojava.

Matematički model za analizu dinamičkog odziva sekcije mosta obuhvaća jednadžbe gibanja u dva stupnja slobode u kojima se kao sile pobude uvrštavaju aerodinamička sila uzgona i moment prevrtanja sekcije mosta uzrokovani gibanjem sekcije mosta. Aerodinamička sila uzgona i moment prevrtanja se mogu izraziti uz pomoć bezdimenzijskih aeroelastičnih koeficijenata (derivativa treperenja), koji su pokazatelji aeroelastične stabilnosti sekcije mosta. U matrici dinamičkog odziva mosta se mogu razlučiti mehaničke matrice krutosti i prigušenja koje se određuju iz dinamičkog odziva mosta bez strujanja zraka, te aerodinamičke matrice krutosti i prigušenja koje ovise o dinamičkom odzivu sekcije mosta uslijed strujanja zraka. Iz dobivenih matrica krutosti i prigušenja sustava računaju se bezdimenzijski aeroelastični koeficijenti (derivativi treperenja). Za određivanje navedenih matrica potrebno je poznavati vlastite frekvencije vibracija te prigušenja sustava, koje se određuju iz izmjerenog dinamičkog odziva sekcije mosta.

Težište ovog rada je na aerodinamičkim i aeroelastičnim svojstvima visećih i ovješenih mostova s cestovnim vjetrobranima, i to posebice na analizi vibracija uzrokovanih gibanjem sekcije mosta uslijed puhanja vjetra. Analiza aerodinamičkih svojstava sekcija mostova uključuje određivanje aerodinamičkih sila uzgona i otpora i momenta prevrtanja sekcija mostova, te karakteristike strujanja zraka oko sekcija mostova. Analiza aerodinamičke stabilnosti mostova s ugrađenim cestovnim vjetrobranima obuhvaća određivanje aeroelastičnih koeficijenata i analizu vlastitih frekvencija sekcija mostova uz dva stupnja slobode gibanja za izračun kritične brzine strujanja zraka karakteristične za pojavu treperenja.

Hipoteze istraživanja:

1. Dinamička stabilnost sekcija mostova je pogoršana i kritična brzina strujanja vjetra za pojavu treperenja je smanjena kada su cestovni vjetrobrani ugrađeni na sekcije mostova.

2. Smanjenje poroznosti cestovnih vjetrobrana na sekcijama mostova povećava dinamičku nestabilnost mostova.

3. Aerodinamička sila otpora sekcija mostova je veća kada su cestovni vjetrobrani ugrađeni na most.

Istraživanja su provedena eksperimentalno u klimatskom zračnom tunelu Instituta za teorijsku i primijenjenu mehaniku u Pragu, Češka. Ovaj zračni tunel je göttingenskog tipa (zatvoreni tok struje zraka), a sastoji se od aerodinamičke i klimatske sekcije. Aerodinamička sekcija je konstruirana s ciljem provedbe eksperimenata vezanih uz djelovanje vjetra na konstrukcije i vozila, pravokutnog je poprečnog presjeka s visinom od 1,8 m i širinom od 1,9 m. Brzina strujanja u aerodinamičkoj sekciji se može podešavati od 0,5 m/s do 35 m/s, a intenzitet turbulencije na ulazu u praznu ispitnu sekciju je manji od 2%.

U sklopu istraživanja su korištena tri modela sekcije mosta: Kao-Pin Hsi (Tajvan), Great Belt (Danska-Švedska) i Golden Gate (SAD). Sva tri modela sekcije mosta su izrađena u geometrijskom mjerilu 1:100, dok su duljine sekcija modela ovih mostova (poprečno horizontalno na smjer strujanja zraka) kod svih modela 1 m. Modeli cestovnih vjetrobrana različitih visina i poroznosti su također izrađeni u geometrijskom mjerilu 1:100.

U prvom dijelu eksperimentalnog rada istražen je utjecaj poroznosti i visine cestovnog vjetrobrana postavljenog samo na uzvodni rub sekcija mostova na aerodinamička i aeroelastična svojstva sekcija mostova. Pritom su korišteni stupnjevi poroznosti vjetrobrana od 0%, 30% i 50%, te (modelske) visine vjetrobrana od 30 mm, 40 mm i 50 mm.

U drugom dijelu eksperimentalnog rada istražen je utjecaj načina postavljanja vjetrobrana na aerodinamička i aeroelastična svojstva sekcija mostova. Pritom su vjetrobrani različitih visina postavljeni na sljedeće načine: a) vjetrobran postavljen samo na uzvodni rub sekcije mosta, b) vjetrobran postavljen samo na nizvodni rub sekcije mosta, c) vjetrobrani postavljeni na oba ruba sekcije mosta.

S ciljem dobivanja aerodinamičkih koeficijenata sila i momenta prevrtanja, koristio se eksperimentalni mehanizam razvijen u sklopu ovog doktorskog rada. Ovim mehanizmom je moguće zasebno odrediti aerodinamičke sile otpora i uzgona, kao i moment prevrtanja sekcije mosta. Mjerenja su provedena tenzometrima postavljenim na eksperimentalni mehanizam. Tenzometri su povezani s galvanski izoliranim modulima te se signal pojačava i filtrira

tijekom mjerenja. Odziv tenzometara na vanjsko opterećenje je linearan. Konstrukcija mehanizma za određivanje aerodinamičkih sila i momenta prevrtanja je opremljena bočnim ravnim pločama čime se osigurava dvodimenzijsko strujanje zraka, dok je Prandtl-Pitotova cijev korištena za mjerenje brzine strujanja zraka. Aerodinamički koeficijenti sile uzgona, sile otpora, i momenta prevrtanja su bitni za određivanje statičke i dinamičke stabilnosti sekcija mostova s obzirom na pojavu galopiranja sekcija mostova. Procjena dinamičke stabilnosti galopiranja sekcija mostova je provedena uz korištenje Glauert-Den Hartogovog kriterija.

Kod provedbe ispitivanja dinamičke stabilnosti mostova, modeli su postavljeni na mehanizam razvijen za potrebe određivanja aeroelastičnog odziva modela sekcije mosta, koji omogućava pomake u vertikalnom smjeru kao i rotaciju modela sekcije mosta. Ovaj mehanizam omogućava precizno i brzo podešavanje prirodnih frekvencija oscilacija u vertikalnom i rotacijskom gibanju, čime se podešava krutost sustava. Konstrukcija mehanizma za aeroelastična ispitivanja je opremljena ravnim bočnim pločama za izbjegavanje nepoželjnog utjecaja dijelova mehanizma na strujanje zraka oko modela sekcije mosta. Referentna brzina strujanja zraka se mjeri Prandtl Pitotovom cijevi koja je postavljena uzvodno od modela sekcije mosta. Vertikalni pomak i torzijski zakret modela sekcije mosta je izmjerena magnetskih osjetnicima. Kinematika eksperimentalnog mehanizma i ponašanje opruga su linearni. Eksperimenti su provedeni metodom slobodnih vibracija, koja uključuje inicijalni pomak modela sekcije mosta u vertikalnom i rotacijskom smjeru, te mjerenja prigušenja slobodnih oscilacija pri različitim brzinama strujanja zraka.

Polje brzine strujanja zraka oko modela sekcije mosta je određeno uz primjenu PIV (engl. *Particle Image Velocimetry*) metode. Zrak koji struji u zračnom tunelu se ispunjava sitnim česticama koje se osvjetljavaju laserskim snopom svjetla u području oko modela sekcije mosta. Raspodjela sitnih čestica u dva bliska vremenska trenutka se mjeri uz pomoć visokofrekventne kamere te se koristi za izračunavanje polja brzine i vrtložnosti strujanja zraka.

Postignuti eksperimentalni rezultati ukazuju na značajan utjecaj cestovnih vjetrobrana na aerodinamičke i aeroelastične karakteristike sekcija visećih i ovješenih mostova.

U slučaju vjetrobrana postavljenog samo na uzvodni rub sekcije mosta, koeficijent aerodinamičkog otpora se povećava kod smanjenja poroznosti vjetrobrana, te povećavanjem visine vjetrobrana. Ovaj trend je zabilježen kod sekcija svih ispitivanih mostova, te je

izraženiji u rasponu pozitivnih napadnih kutova struje zraka, tj. kad zrak nastrujava na sekciju mosta od gore prema dolje. Utjecaj vjetrobrana na povećanje koeficijenta aerodinamičkog otpora je izraženiji za slučaj mostova koji imaju aerodinamičan oblik, odnosno kod kojih je manje izraženo odvajanje struje zraka (npr. Great Belt). Cestovni vjetrobrani mijenjaju trendove i apsolutne vrijednosti koeficijenta aerodinamičkog uzgona, dok je to izraženije za vjetrobrane s većom visinom i manjom poroznosti. Koeficijent aerodinamičkog momenta prevrtanja sekcija mostova je manji kada su cestovni vjetrobrani postavljeni na sekcije mosta u odnosu na sekcije mosta bez vjetrobrana, dok je utjecaj poroznosti vjetrobrana dominantan u odnosu na utjecaj visine vjetrobrana.

Raspored vjetrobrana također bitno utječe na koeficijente aerodinamičkih sila uzgona i otpora. U uobičajenom rasponu napadnih kutova struje zraka na most (napadni kut je relativno mali ili jednak nuli), svi istraživani rasporedi postavljanja vjetrobrana doprinose negativnoj sili uzgona, tj. vertikalno prema dolje. Za neke ispitivane konfiguracije, vjetrobrani uzrokuju promjenu smjera aerodinamičke sile uzgona. Raspored vjetrobrana ne utječe značajno na koeficijent aerodinamičkog momenta prevrtanja. Stoga, raspored postavljanja vjetrobrana na sekcije mostova ne utječe na torzijsku divergenciju sekcija mosta.

Cestovni vjetrobrani pri svim ispitivanim visinama, poroznosti te rasporedima postavljanja ne utječu na galopiranje mostova, tj. osjetljivost na galopiranje je približno jednaka za sekcije mostova sa i bez cestovnih vjetrobrana; dinamička stabilnost s obzirom na galopiranje sekcija mosta je postignuta kvazistacionarnim pristupom i u dinamičkim testovima. S druge strane, promjena pozitivnog u negativni (i obratno) gradijent sile uzgona s obzirom na kut nastrujavanja zraka, a koja je zabilježena kod nekih ispitivanih konfiguracija, sugerira moguće kritične konfiguracije s obzirom na dinamičku stabilnost uslijed vertikalnog gibanja sekcija mosta.

U slučaju vjetrobrana postavljenog samo na uzvodnu stranu sekcije mosta, osjetljivost na torzijski oblik treperenja je značajno povećana. Ovo je izraženije za manje porozne vjetrobrane, dok su utjecaji visine vjetrobrana istodobno uvjetovani aerodinamičkim oblikom sekcije mosta na koji se vjetrobran postavlja. Sekcije mostova koje imaju aerodinamičan oblik (npr. Great Belt) su općenito osjetljivije na torzijski oblik treperenja ako su na njih postavljeni niži vjetrobrani, dok su sekcije mostova koje imaju manje aerodinamičan oblik

(npr. Golden Gate) osjetljivije na torzijski oblik treperenja ako su na njih postavljeni viši vjetrobrani.

Raspored vjetrobrana također utječe na osjetljivost s obzirom na treperenje sekcija mostova. Vjetrobran postavljen samo na uzvodnu stranu sekcija mosta i vjetrobrani postavljeni na obje strane mosta značajno utječu na torzijski oblik treperenja sekcija mostova, dok postavljanje vjetrobrana samo na nizvodnu stranu sekcija mosta ne utječe značajno na torzijski oblik treperenja sekcija mostova. Vjetrobran postavljen samo na uzvodnu stranu sekcija mosta, te vjetrobrani postavljeni na obje strane sekcija mosta mogu uzrokovati vibracije uslijed periodičnog odvajanja vrtloga. Rezultati analize vlastitih vrijednosti sustava s dva stupnja slobode gibanja za izračun kritične brzine strujanja zraka kod koje se javlja treperenje se općenito podudaraju s trendovima aeroelastičnih koeficijenata treperenja.

Osrednjene brzine strujanja zraka su značajno smanjene iznad sekcija mosta nizvodno od vjetrobrana, što potvrđuje zaštitna svojstva vjetrobrana s obzirom na stabilnost vozila koja prometuju mostovima; ovaj rezultat je u skladu s prethodnim istraživanjima. Vjetrobran postavljen samo na uzvodnu stranu sekcija mostova i vjetrobrani postavljeni na obje strane sekcija mostova ukazuju na slične trendove s obzirom na osrednjene brzine strujanja vjetra na gornjoj strani sekcija mostova. Najveća varijanca brzine strujanja zraka je postignuta u smičnom sloju koji se odvaja od vrha uzvodnog vjetrobrana. Karakteristike tog smičnog sloja uvjetuju karakteristike aerodinamičke sile uzgona i momenta prevrtanja sekcija mostova.

Predloženi ciljevi istraživanja za ovaj doktorski rad su postignuti i postavljene hipoteze istraživanja su ispunjene. Prikazani rezultati potvrđuju da, dok vjetrobrani štite vozila od bočnih vjetrova, oni također uzrokuju negativne promjene aerodinamičkih koeficijenata sila i momenta prevrtanja, te smanjuju aerodinamičku stabilnost mostova.

Moguća tema budućih istraživanja je optimizacija oblika vjetrobrana koji bi pružao zadovoljavajuću zaštitu vozila od bočnog vjetra, te istovremeno ne bi bitno narušavao aerodinamičku stabilnost mostova. Ova svojstva se potencijalno mogu zadovoljiti koristeći vjetrobrane s promjenjivom poroznosti s obzirom na karakteristike nadolazećeg vjetra. Utjecaj mirujućih i prometujućih vozila na aerodinamička i aeroelastična svojstva mostova s vjetrobranima također još nije u potpunosti istražen, kao niti utjecaj tranzijentnih vjetrova (npr. bura, uragan, tornado) na aerodinamičke karakteristike visećih i ovješenih mostova opremljenih cestovnim vjetrobranima.

Ključne riječi

Viseći i ovješeni mostovi; cestovni vjetrobrani; aerodinamičke sile i momenti; treperenje mosta; galopiranje mosta; eksperimenti u zračnom tunelu.

List of Figures

Figure 1: Two main categories of long-span bridges: (a) Cable-stayed bridge, (b) suspension bridge. 2

Figure 2: Akashi Kaikyo Bridge in Japan - the longest central bridge span ever built. Photo courtesy of http://broer.no 3

Figure 3: Flow characteristics around various types of bridge decks; flow is from right to left. 4

Figure 4: Lock-in phenomenon of the vortex-shedding frequency. 7

Figure 5: Tacoma Narrows Bridge flutter oscillations leading to a collapse. Photo from https://www.txstate.edu. 9

Figure 6: Types of bridge models for aeroelastic tests in wind tunnels. 11

Figure 7: Overturned trucks at North Carolina Bridge and Mackinac Bridge, USA. Photos courtesy of http://livetrucking.com and http://wcrz.com. 13

Figure 8: Sign convention for aerodynamic loads and displacements of bridge decks. 18

Figure 9: Aerodynamic lift and drag forces experienced by the bridge-deck section subjected to the flow. 19

Figure 10: Schematic view of the Vincenc Strouhal wind tunnel of the Institute of Theoretical and Applied Mechanics (ITAM) in Prague, Czech Republic 33

Figure 11: Geometrical details of the studied bridge-deck section models: (a) Great Belt Bridge, (b) Kao-Pin Hsi Bridge, (c) Golden Gate Bridge. All dimensions are in mm provided in model scale. 34

Figure 12: Wind-barrier sheltering of trucks for various wind incidence angles. 36

Figure 13: Geometrical details of the studied wind-barrier models: (a) front view, (b) WB 5_50, (c) WB 5_30, (d) WB 5_00, (e) WB 3_30, (f) WB 7_30. All dimensions in mm are provided in model scale, flow direction is from left to right. 38

Figure 14: Experimental setup for flow characterization using the PIV technique. 39

Figure 15: Seeding particles around the bridge-deck section model illuminated by laser. 40

Figure 16: Experimental setup for the flow characterization measurements. 41

Figure 17: Kinematic scheme of the experimental mechanism for measurements of the aerodynamic drag and lift forces and the pitch moment. 42

Figure 18: Calibration results for strain gauges for the drag and lift forces and the pitch moment. 43
Figure 19: Experimental setup for measurements of the aerodynamic force and moment coefficients. 44
Figure 20: Kinematic scheme of the experimental stand for measurements of aeroelastic properties of bridge-deck section models, Král et al. (2016). 45
Figure 21: Experimental setup for the measurement of the dynamic response of bridge-deck section models. 46
Figure 22: Examples of the dynamic response of the bridge-deck section model: (a) relatively small airflow velocity, (b) proximity of torsional flutter. 47
Figure 23: Turbulence grid placed upstream of the bridge-deck section model: (a) low turbulence, (b) high turbulence. 50
Figure 24: Development of the turbulence intensity along the test section (x-direction). 51
Figure 25: Mean flow velocity field around the Great Belt Bridge deck section for various heights and porosities of the windward wind barrier. Flow direction is from left to right. 54
Figure 26: Flow velocity profiles at x/B = 0 for various (a) porosities and (b) heights of the windward wind barrier. 55
Figure 27: Mean flow velocity field around the Great Belt Bridge deck section for various arrangements of wind barriers. Flow direction is from left to right. 57
Figure 28: The flow velocity profiles at x/B = 0 for various arrangements of the 5 m high (full-scale) and 50 % porous wind barrier. 58
Figure 29: Flow velocity variance around the Great Belt Bridge deck section for various heights and porosities of the windward wind barrier. Flow direction is from left to right. 59
Figure 30: The profiles of the flow velocity variance at x/B = 0 for various (a) porosities and (b) heights of the windward wind barrier. 60
Figure 31: Flow velocity variance around the Great Belt Bridge deck section for various arrangements of wind barriers. Flow direction is from left to right. 62
Figure 32: The profiles of the flow velocity variance at x/B = 0 for various arrangements of the 5 m high (full-scale) and 50 % porous wind barrier. 63
Figure 33: Drag force coefficient for bridge-deck sections with: (a) 5 m high (full-scale) wind barriers of various porosities, (b) 30% porous wind barriers of various full-scale heights. 65

Figure 34: Relative increase in the drag force coefficient in comparison with the empty bridge-deck sections: (a) 5 m high (full-scale) wind barriers of various porosities, (b) 30% porous wind barriers of various heights. 67
Figure 35: Lift force coefficient for bridge-deck sections with: (a) 5 m high (full-scale) wind barriers of various porosities, (b) 30% porous wind barriers of various full-scale heights. 68
Figure 36: Pitch moment coefficient for bridge-deck sections with: (a) 5 m high (full-scale) wind barriers of various porosities, (b) 30% porous wind barriers of various full-scale heights. 70
Figure 37: Drag force coefficient for various arrangements of wind barriers at various flow incidence angles. 72
Figure 38: Lift force coefficient for various arrangements of wind barriers at various flow incidence angles. 74
Figure 39: Pitch moment coefficient for various arrangements of wind barriers at various flow incidence angles. 75
Figure 40: Gradient of the lift force coefficient with respect to the flow incidence angle for all studied bridge-deck sections with the windward wind barrier. 77
Figure 41: H_1^* FD for bridge-deck sections with: (a) 5 m high (full-scale) wind barriers of various porosities (0%, 30%, and 50%), (b) 30% porous wind barriers of various full-scale heights (3 m, 5 m, and 7 m). 79
Figure 42: Amplitude spectrum of v(t) for the GBB with WB 5_00; measurement position is 50 mm downstream of the bridge-deck section model in 15 mm height with respect to the top surface of the bridge-deck section model. 81
Figure 43: H_2^* FD for bridge-deck sections with: (a) 5 m high (full-scale) wind barriers of various porosities (0%, 30%, and 50%), (b) 30% porous wind barriers of various full-scale heights (3 m, 5 m, and 7 m). 82
Figure 44: H_3^* FD for bridge-deck sections with: (a) 5 m high (full-scale) wind barriers of various porosities (0%, 30%, and 50%), (b) 30% porous wind barriers of various full-scale heights (3 m, 5 m, and 7 m). 84
Figure 45: A_1^* FD for bridge-deck sections with: (i) 5 m high (full-scale) wind barriers of various porosities (0%, 30%, and 50%), (ii) 30% porous wind barriers of various full-scale heights (3 m, 5 m, and 7 m). 86

Figure 46: A_2^* FD for bridge-deck sections with: (a) 5 m high (full-scale) wind barriers of various porosities (0%, 30%, and 50%), (b) 30% porous wind barriers of various full-scale heights (3 m, 5 m, and 7 m). 87
Figure 47: A_3^* FD for bridge-deck sections with: (a) 5 m high (full-scale) wind barriers of various porosities (0%, 30%, and 50%), (b) 30% porous wind barriers of various full-scale heights (3 m, 5 m, and 7 m). 89
Figure 48: H_1^* FD for bridge-deck sections with various arrangements of wind barriers. 91
Figure 49: Generalized damping in the heave motion for the Great Belt Bridge and various arrangements of WB 5_30. 92
Figure 50: A_2^* FD for bridge-deck sections with various arrangements of wind barriers. 94
Figure 51: A_3^* FD for bridge-deck sections with various arrangements of wind barriers. 95
Figure 52: Critical flow velocity for flutter calculated using the eigenvalue analysis for bridge-deck section models and various arrangements of wind barriers. 98
Figure 53: Frequency at critical flow velocity for flutter calculated using the eigenvalue analysis for bridge-deck section models and various arrangements of wind barriers. 99
Figure 54: Percentagewise decrease of the critical flow velocity for flutter for the Kao-Pin Hsi and Golden Gate Bridge deck sections when the wind-barriers are in place with respect to the empty bridge-deck sections (without wind-barriers). 100
Figure 55: Numerical solutions of the 2DOF flutter equation for the Great Belt Bridge and various configurations of the 5 m high (full-scale) wind barrier. 102
Figure 56: H_1^* and A_2^* FDs for three different turbulence intensities of the freestream flow. 103

List of Tables

Table 1 General characteristics of studied wind barriers 37

Table 2: Mass characteristics and dynamic properties of the studied bridge-deck section models. 49

Table 3: Critical flow velocities for flutter calculated using the eigenvalue analysis for bridge-deck section models with 5 m high (full-scale) wind barriers of various porosities (0%, 30%, and 50%).....96

Table 4: Critical flow velocities for flutter calculated using the eigenvalue analysis for bridge-deck section models with 30% porous wind barriers of various full-scale heights (3 m, 5 m, and 7 m). 97

List of Symbols

Symbol	Unit	Description
A	m^2	Reference area
A_i^*	-	Flutter derivatives
A_α	m	Initial excitation in the pitch direction
A_h	m	Initial excitation in the heave direction
B	m	Width
c	kg/s^2	Stiffness of the system
C	kg/s^2	Stiffness matrix
C_D	-	Aerodynamic drag force coefficient
C_L	-	Aerodynamic lift force coefficient
C_M	-	Aerodynamic pitch moment coefficient
d	kg/s	Dynamic system damping
e_m	-	Error vector in the Unifying Least Square iteration process
$F(t)$	N	External forces vector
F_i	N	Components of the resultant aerodynamic force
F_D	N	Aerodynamic drag force
F_L	N	Aerodynamic lift force
F_{Ls}	N	Aerodynamic self-excited lift force
f_{cr}	Hz	Critical frequency for flutter
f_h	Hz	Natural frequency in the heave direction
f_α	Hz	Natural frequency in the pitch direction
f_{Vs}	Hz	Vortex shedding frequency
H_i^*	-	Flutter derivatives
H	m	Height
h	m	Displacement in the heave (vertical) direction
$\dot{h}$	m/s	Velocity in the heave direction
$\ddot{h}$	m/s^2	Acceleration in the heave direction
$\hat{h}_m$	m	Estimated heave dynamic response
I	kg/m^2	Mass inertia

$I(z)$	-	Turbulence intensity
J	-	Objective function in the Unifying Least Square iteration process
k	kg/s^2	Stiffness of the system
K	-	Reduced frequency
K	kg/s	Damping matrix
L	m	Length
M	Nm	Aerodynamic pitch moment
M	kg	Mass matrix
m	kg	Mass of the body
M_s	Nm	Aerodynamic self-excited pitch moment
n_j	m	Components of the normal vector
p	N/m^2	Air pressure
Re	-	Reynolds number
S_v	m/s	Standard deviation of the flow velocity
St	-	Strouhal number
t	s	Time
Δt	s	Time step
v_∞	m/s	Undisturbed freestream flow velocity
Var	-	Variance of the flow velocity
v_{cr}	m/s	Critical flow velocity for flutter
$Ur,\ Vr$	-	Coefficients in the Unifying Least Square iteration process
x_s	m	Equilibrium position
x	m	Displacement vector
α	m	Angle displacement in the pitch direction
$\dot{\alpha}$	m/s	Angular velocity in the pitch direction
$\ddot{\alpha}$	m/s^2	Angular acceleration in the pitch direction
$\hat{\alpha}_m$	m	Estimated pitch dynamic response
ε	-	Acceptable tolerance in the Unifying Least Square iteration process
ρ	kg/m^3	Air density
ξ_h	-	Mechanical damping in the heave direction
ξ_α	-	Mechanical damping in the pitch direction
λ_r, A_r	-	Complex parameters in the assumed free decay response

Σ_{ji}	$\mathrm{N/m^2}$	Components of the viscous stress tensor
σ_{ji}	$\mathrm{N/m^2}$	Components of the stress tensor
ω_{α}	1/s	Damped natural circular frequency in the pitch direction
ω_{h}	1/s	Damped natural circular frequency in the heave direction
ω_{n}	1/s	Undamped natural frequency

Chapter 1

Introduction

Trends in design of contemporary cable-supported bridges. Wind effects on cable-supported bridges. Aeroelasticity and fundamental aeroelastic phenomena. Current activities about wind effects on cable-supported bridges, flutter dynamic instability and roadway wind barriers. Motivation, research objectives and hypotheses and the expected scientific contribution.

1.1. Design of cable-supported bridges

Recent developments in building technology along with architectural requirements yielded a significant increase in span length of bridges. Span is the distance between two adjacent supports of a structure, i.e. two towers of a bridge supporting the bridge deck.

Bridges are commonly classified with respect to a distribution of the external and internal loads through the structure. Two main categories of contemporary long-span bridges are cable-stayed and suspension bridges, Figure 1.

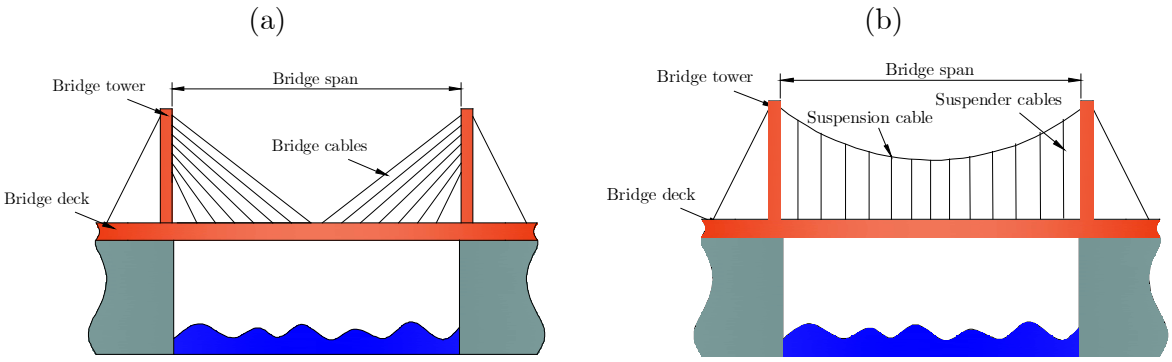

Figure 1: Two main categories of long-span bridges: (a) Cable-stayed bridge, (b) suspension bridge.

Cable-stayed bridges (Figure 1.1a) are supported by the cables which are extended from the tower to the bridge deck in a fan-like pattern or in parallel lines. Suspension bridges (Figure 1.1b) are suspended by the cables as well; however, the cables extend vertically from the bridge deck to the suspension cable that connects the tops of two bridge towers. These two types of bridges are commonly called cable-supported bridges.

While the cable-stayed bridges have been commonly used for bridge spans up to 1 km, suspension bridge design has been used for long-span bridges, e.g. Akashi Kaikyo Bridge in Japan with the span of 1991 m, Figure 2.

Figure 2: Akashi Kaikyo Bridge in Japan - the longest central bridge span ever built. Photo courtesy of http://broer.no.

7 out of 10 bridges with longest spans were built in the 21th century, thus indicating the current trend of building longer and larger bridges. Long-span suspension and cable-stayed bridges are flexible slender structures characterized by relatively low natural frequency and low mechanical damping in the pitch and heave motions. Due to an increase in the span length of contemporary cable-supported bridges, these engineering superstructures are highly susceptible to wind effects.

1.2. Wind effects on cable-supported bridges

1.2.1. Wind characteristics around cable-supported bridges

Bridge design is influenced by many factors, such as span length, terrain properties, climate conditions and owner preferences. As the wind blows around bridge-deck sections, the flow may separate from the bridge. In general, bridge decks may be classified in three categories with respect to the flow separation from bridge decks: (i) streamlined bridge deck with little flow separation, e.g. Humber Bridge, (ii) semi-bluff or semi-streamlined bridge deck with more noticeable flow separation, e.g. Osman Gazi Bridge, (iii) bluff bridge deck with substantial flow separation, e.g. Akashi Kaikyo Bridge. Those differences in the trends of the flow separation are due to the aerodynamic shape of bridge decks and additional bridge elements. Flow characteristics around those three types of bridge-deck sections are schematically presented in Figure 3.

(a) Streamlined bridge deck

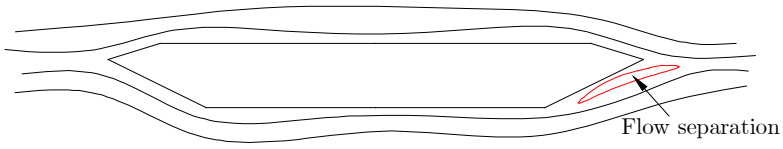

(b) Semi-bluff bridge deck

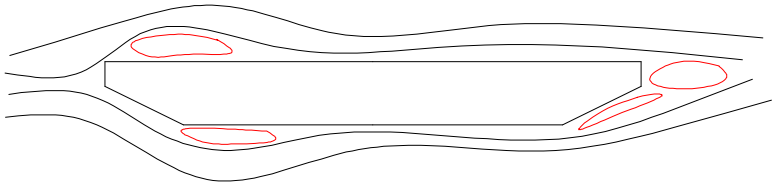

(c) Bluff bridge deck

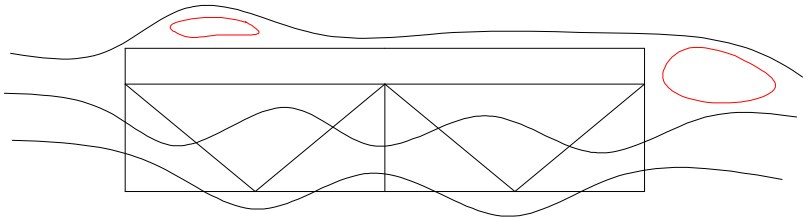

Figure 3: Flow characteristics around various types of bridge decks; flow is from right to left.

For the streamlined bridge decks, the flow separation may occur at the leeward (downstream) edge of the bridge deck, whereas its intensity is rather low. The flow separation for the semi-bluff bridge decks may occur at the windward (upstream) edge of the bridge deck in addition to the flow separation at the leeward edge, while the flow commonly reattaches at the bridge-deck surface. For the bluff bridge decks, the flow on the bottom surface of the bridge deck through the steel-stiffening structure is quite chaotic accompanied by an intense flow separation, while it may occur on both the windward and leeward bridge deck edges.

1.2.2. Aerodynamic loading of cable-supported bridges

The dominant aerodynamic forces acting on bridge decks are the drag force acting in the horizontal (main flow) direction and the lift force acting in the vertical direction. This is

due to design characteristics of long-span bridge decks, i.e. large ratio between the span and other characteristic dimensions. A distribution of these two forces with respect to the bridge deck center of gravity yields the aerodynamic pitch moment. For the long-span bridges, the reference area for both the drag force and the lift force are quite large; hence, the integral aerodynamic forces acting on bridge decks may be significant. These forces yield a substantial load on bridge supporting structures, e.g. the aerodynamic lift force affects the tension of cables on suspension bridges.

The top surface of bridge decks (i.e. road) is flat, hence the streamlined bridge decks may experience smaller air pressure on the bottom side of bridge decks in comparison with the top surface and consequently large integral aerodynamic forces and moments. On the other hand, the semi-bluff and bluff bridge decks may experience stronger fluctuations of the aerodynamic forces and moments due to a more pronounced flow separation.

1.2.3. Aeroelasticity of cable-supported bridges

In addition to the average aerodynamic integral forces and the pitch moment, where bridges are considered as static solid bodies, the aeroelastic behavior of contemporary long-span cable-supported bridges is quite important because their substantial span length makes them flexible and sensitive to wind actions.

Aeroelasticity generally addresses an interaction among elastic, inertial and aerodynamic forces experienced by an elastic body that is subjected to the fluid flow. It was originally believed that the aeroelastic problems occur in aerospace engineering only, e.g. airplane-wing flutter. However, a collapse of the Tacoma Narrows Bridge in 1940 indicated that the bridge aeroelasticity phenomena could cause civil engineering structures (like bridges) to collapse as well, so this unfortunate event motivated the aeroelasticity to be addressed in bridge engineering as well, e.g. Miyata (2003). Nowadays the aeroelastic phenomena are commonly considered when designing tall towers and buildings, long-span suspension and cable-stayed bridges, power lines and similar slender structures, e.g. Hansen et al. (2006), Shyy et al. (2010), Kareem and Wu (2013).

In general, it is an important goal for bridge engineers to design bridges that have critical flow velocities for divergent self-excited oscillations larger than the maximum expected wind velocities in the particular geographic region to avoid occurrence of dynamic instability

during the bridge lifetime. Aeroelasticity can be studied as the static and dynamic aeroelasticity. The static aeroelasticity deals with a steady response of an elastic body in a fluid flow; hence, inertial forces are not accounted for. It can be further divided into control reverse and torsional divergence. Control reverse is aeroelastic phenomena occurring on aircrafts when elastic deformations due to aerodynamic forces influence the controllability of an aircraft, e.g. Yoon et al. (2012). Torsional divergence occurs when a body deflects due to the aerodynamic pitch moment, while this phenomenon may further increase aerodynamic loads and cause the structure to collapse, e.g. Zhang et al. (2013). This phenomenon was common on aircraft wings in the past. As the aircraft wing bends due to the aerodynamic pitch moment, the flow incidence angle of the wing increases, thus further increasing aerodynamic loads and ultimately leading to a failure of the wing.

Dynamic aeroelasticity addresses the dynamic response of a body immersed into the flow for the case when the inertial forces are taken into account as well. Based on a source of structure excitation, there are three different kinds of dynamic aeroelasticity, i.e. (i) self-excited vibrations, (ii) instability-induced vibrations, (iii) extraneously-induced vibrations.

For bridges, the self-excited vibrations (galloping and flutter) are most dangerous. They are caused due to self-excited aerodynamic forces that arise due to the body movement and occur due to a complex interaction between the airflow and the vibrating bridge deck. It is therefore required to carefully analyze aeroelastic behavior of long-span bridges during construction and service prior to building the bridge. Hence, aeroelastic studies are commonly performed experimentally on small-scale bridge-deck section models in wind tunnels, e.g. Larsen (1993).

1.2.4. Vortex-Induced-Vibration

Vortex-Induced-Vibration (VIV) occurs due to the vortex shedding from the leading bridge-deck edge, which phenomenon may be observed intermittently on the top and bottom bridge-deck surfaces. These shed vortices define the oscillatory aerodynamic force in the direction perpendicular (vertical) to the main flow direction. At the vortex-shedding frequency equal to the natural frequency of a body, the body starts to vibrate, e.g. Matsumoto (1999). While vortex-induced vibrations are often not disastrous for contemporary bridges, they may nevertheless yield a considerable fatigue of structural

components, e.g. Diana et al. (2006). It is therefore important that the natural frequencies of all bridge components are not in the range of the vortex-shedding frequency. The vortex-shedding frequency for a given structure is linearly dependent on the flow velocity - the Strouhal number,

$$\mathrm{St} = \frac{f_{vs} L}{v}, \tag{1.1}$$

where St is Strouhal number, f_{vs} is vortex-shedding frequency, L is characteristic length, v is flow velocity. With increasing the flow velocity, the vortex-shedding frequency increases as well to satisfy the characteristic St for a given structure. When the vortex-shedding frequency becomes equal to the natural frequency of the structure, a further increase in the flow velocity does not yield a further increase in the vortex-shedding frequency, but the vortex-shedding frequency remains equal (for a narrow range of flow velocities) to the natural frequency of the structure. This range of flow velocities, where the vortex-shedding frequency does not satisfy the characteristic St but remains constant, is known as the lock-in region with stable-orbit oscillations, Figure 4.

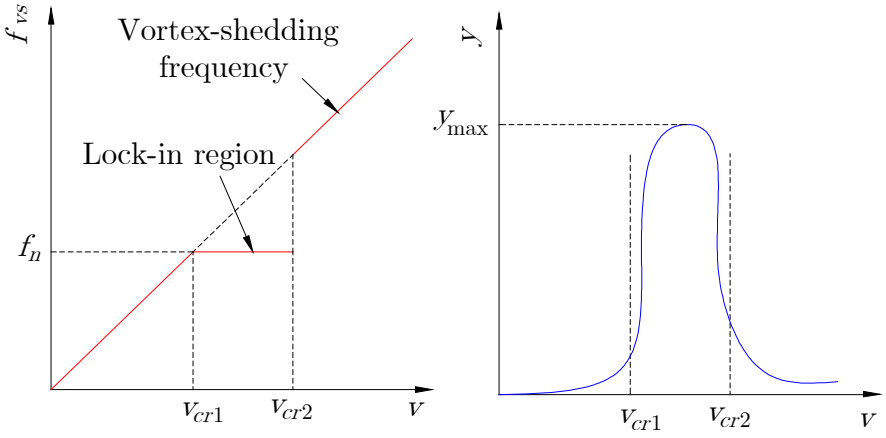

Figure 4: Lock-in phenomenon of the vortex-shedding frequency.

1.2.5. Galloping instability

Galloping is the aerodynamic instability typical for slender structures with particular cross-sectional shapes such as, for example, rectangular or 'D' sections or ice-coated power-line cables, where the flow reattachment on the body surface does not occur after the flow separated at the leading edge of the structure, e.g. Simiu and Scanlan (1996). Galloping is

not considered to be a typical instability mode for long-span cable-supported bridges, but it may nevertheless affect bridge-deck sections with width to height aspect-ratio smaller than three, i.e. bridge-deck sections that are considered to be bluff, e.g. Ruscheweyh et al. (1996), Carassale et al. (2013), Mannini et al. (2014), Nguyen et al. (2015), while the flow at an incidence angle may trigger this instability as well, e.g. Argentini et al. (2018).

Galloping is characterized by large amplitude oscillations perpendicularly and vertically to the main flow direction; therefore, this instability is often called across-wind galloping. Frequency of motion at which this instability occurs is usually rather small, i.e. much smaller than the characteristic vortex-shedding frequency of the same bridge-deck section. Another way to distinguish galloping from vortex-shedding oscillations is that the vortex-shedding oscillations appear at a certain flow velocity and die out when the flow velocity further increases, while the galloping amplitudes start to occur at a certain flow velocity and further increase with an increase in the flow velocity.

1.2.6. Flutter instability

Flutter is a dynamic self-excited instability influenced by the flow and vortex separation from the leading edge of bridge decks and a possible reattachment of the downstream flow. It is characterized by the coupling of the aerodynamic forces and the motion of the bridge deck, as the motion of the bridge deck results in self-excited aerodynamic forces and self-excited oscillations. Wind forces feed the energy into the system during each individual cycle of oscillation, and they are counteracted by the structural damping, as the fed energy is dissipated through the characteristic structural damping of the bridge deck.

When the flow velocity becomes critical , the net damping (a sum of the structural damping of a bridge deck - positive by definition, and the modal damping due to a wind, i.e. aerodynamic damping that may become negative) is zero, and the critical state of the bridge deck is achieved, i.e. the system is dynamically on the stability threshold (bifurcation point). In case the wind velocity further increases, the negative modal damping due to a wind additionally increases; therefore, the net damping becomes negative as well, and any small disturbance to the system, such as buffeting force due to wind turbulence, results in diverging oscillations that ultimately end at a stable cycle limit, e.g. Xu (2013).

This movement-induced vibration often cannot be completely avoided, but critical conditions for flutter appearance can be delayed, i.e. shifted to larger wind velocities, where it is not likely for flutter to occur. Flutter was originally recognized as aeroelastic instability with respect to airfoils, which caused several aircraft accidents. However, subsequent to the collapse of the Tacoma Narrows Bridge (Figure 5) at a wind velocity of only about 19 m/s, wind-tunnel experiments confirmed that it collapsed due to the aeroelastic flutter, e.g. Larsen and Larose (2015). At that point, the flutter instability of bridges became a primary concern for bridge engineers.

Figure 5: Tacoma Narrows Bridge flutter oscillations leading to a collapse. Photo from https://www.txstate.edu.

Classical (coupled) flutter, originally analyzed with respect to thin airfoils on aircrafts, is characterized by two degrees of freedom (vertical and torsional) coupled unstable oscillations that are driven by the wind flow, e.g. Jain et al. (1996).

Stall (torsional) flutter is a single degree of freedom torsional oscillation of airfoils driven by nonlinear characteristics of the lift force in the stall frequency range, or due to a loss of the lift condition, e.g. Dunn and Dugundji (1992). Single-degree-of-freedom (SDOF) torsional flutter commonly appears for bodies characterized by a considerable flow separation, e.g. Matsumoto et al. (1997). A typical example of a body susceptible to this kind of instability is

poorly designed bridge deck, such as the old (collapsed) Tacoma Narrows Bridge. While the SDOF flutter may occur both in the vertical and the torsional mode of vibration, the torsional flutter is more common. From the instability intensity point of view, the flutter can be analyzed as: a) hard flutter and b) soft flutter. Hard flutter characterizes a system where the net damping of the system suddenly decreases and this type of flutter is difficult to predict, i.e. the negative aerodynamic damping increases abruptly with respect to the wind velocity. On the other hand, soft flutter is characterized by a gradual decrease in net damping; hence, the threshold for the aerodynamic stability is gradually approached.

1.3. State-of-the-art of wind effects on cable-supported bridges

Bridge sensitivity to wind effects, particularly to flutter, has been commonly studied using flutter derivatives (FDs). These are the dimensionless coefficients that are used to linearize the self-excited aerodynamic forces and moments around the equilibrium point. They are considered as contributors to the generalized damping and stiffness matrices and indicators of the bridge dynamic stability. The original method for extracting dimensionless FDs was proposed by Scanlan and Tomko (1971). In this method, direct and cross derivatives are extracted separately, whereas it is necessary to maintain the same frequency for the torsional and vertical oscillations. The ARMA (Auto Regressive Moving Average) model for the extraction of FDs was suggested by Shinozuka et al. (1982), while the extended Kalman filtering method for the identification of FDs from coupled-vibration time histories was developed by Yamada et al. (1992). Sarkar (1993) developed a time-domain method to extract FDs from the coupled free-vibration decay response of a bridge deck. A method based on the least square theory was developed by Gu et al. (2000), where FDs were extracted from the free-vibration experiments. This procedure was further developed by Ding et al. (2010) with respect to the stability and precision.

In addition to the free-vibration method, the controlled forced-vibration is another approach for identification of FDs. In this method, the bridge deck is forced to vibrate at a single frequency, while the aeroelastic derivatives are determined from the differences among the inertial and excitation forces. For example, Matsumoto et al. (1996),(1997) investigated torsional flutter of bluff bodies using the forced-vibration method, whereas this approach was used by Falco et al. (1992) as well. FDs obtained using both the free-vibration and controlled

forced-vibration methods were commonly compared to the thin flat plate experiments, as the flat plate proved to be mainly stable with respect to wind-induced vibrations, Theodorsen (1935).

In general, when the wind-tunnel experiments with respect to bridge aeroelasticity are carried out, three different types of small-scale models are commonly used: a) full-bridge model, b) taut-strip bridge model, and c) bridge-deck section model, Figure 6. Full-bridge models are most expensive, because it is necessary to design features such as full geometry of a bridge, mass distribution, stiffness and damping of a structure. In addition, these models require large wind tunnels in order to satisfy blockage requirements, i.e. to keep the blockage of the test section below 5% according to Holmes (2015). Taut-strip models are the models that are in-between the bridge-deck section models and full-bridge models. Taut-strip models are rather rarely used for determination of FDs. Bridge-deck section models represent only a portion of the bridge deck and it is assumed that the flow is two-dimensional, and the bridge-deck section model is characterized by a dynamic response.

(a) Full-bridge model

(b) Taut-strip model

(c) Bridge-deck section model

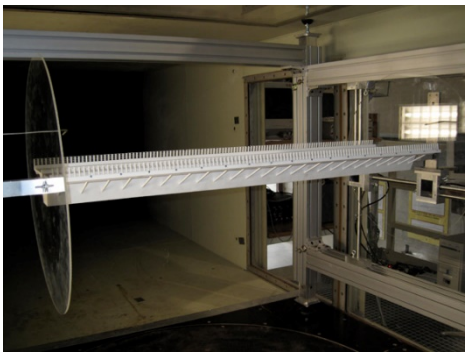

Figure 6: Types of bridge models for aeroelastic tests in wind tunnels.

It is proven that the experiments carried out on short bridge-deck section models are suitable for the analysis of aeroelastic properties of bridge decks due to the fact that the cross-sectional bridge deck is the most important feature for the overall dynamic response of a bridge, Gu et al. (2001). When performing aeroelastic tests using a bridge-deck section model, the rigid model is attached to springs that represent elastic properties of a bridge deck and allow for a motion of a bridge-deck section model in the vertical and torsional directions. The influence of the bridge-deck properties (i.e. mass, mass moment of inertia) on FDs extracted in wind-tunnel tests proved to be negligible, Gu et al. (2001). Scanlan and Lin (1978) noted that the absolute values of FDs in the turbulent flow are slightly larger compared to those identified in the smooth flow. Sarkar et al. (1994) pointed out that the FDs obtained in the smooth flow could be the mean values about which FDs obtained from the turbulent flow fluctuate.

Aerodynamic characteristics of empty cable-supported bridges proved to change in case some additional structures are placed on the bridge deck. Structural elements of bridges and viaducts, e.g. railings, crash barriers, vehicles, central slotting, proved to influence aerodynamic forces and moments of bridges, e.g. Raggett (2007), Diana et al. (2013), Xu et al. (2014a). Design of bridge-deck cross sections may influence their aeroelastic behavior as well, Xu et al. (2014b), while bluff cross sections are in general more susceptible to flutter, e.g. Nikitas et al. (2011).

Vehicles on bridges can significantly alter the dynamic stability of bridge decks, e.g., Han et al. (2014), Han et al. (2015), Pospíšil et al. (2017). As the construction of long-span cable-supported bridges requires a lot of time, the importance of studying aeroelastic stability of bridges during the construction was emphasized in Diana et al. (2013). This is necessary because the bridges prove to have smaller critical flutter velocity in the initial construction stages in comparison with the finalized bridge. Wang et al. (2014) proposed installing rigid central buckle to enhance flutter stability, while external dampers can reduce bridge sensitivity to flutter as well, Jain et al. (1998). Active and passive control methods are commonly used to suppress dynamic instability of bridges, Bakis et al. (2016).

Strong cross-winds on bridges and viaducts may cause dynamic instabilities of vehicles and trains, e.g. Dorigatti et al. (2012). Wind gusts can overturn vehicles and trucks on bridges or

cause them to collide with each other, Figure 7, e.g. Argentini et al. (2011), whereas driving comfort is an important issue as well, Zhou and Chen (2016).

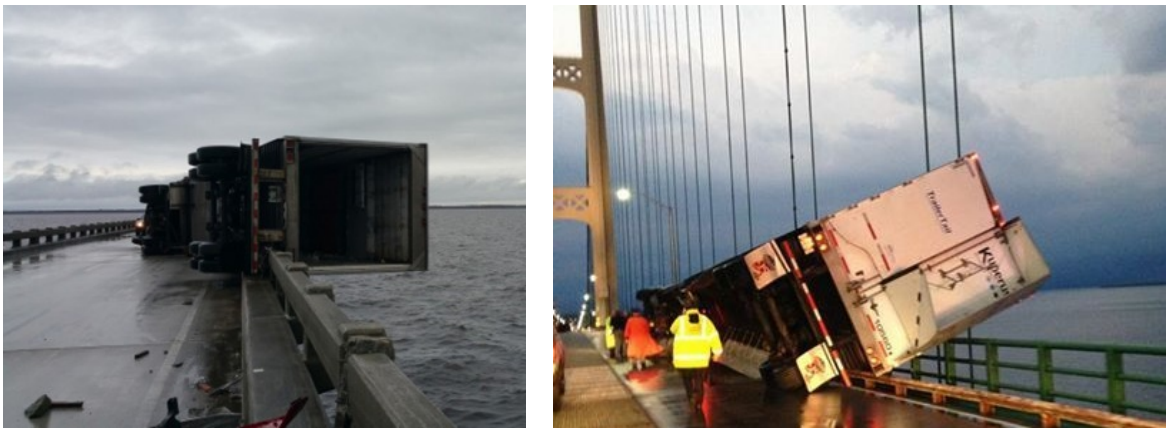

Figure 7: Overturned trucks at North Carolina Bridge and Mackinac Bridge, USA. Photos courtesy of http://livetrucking.com and http://wcrz.com.

Hence, during extreme wind events, unprotected viaducts and bridges are often closed to traffic. To protect vehicles from those adverse cross-wind effects in harsh wind conditions and to keep the roads open even in strong wind conditions, roadway wind barriers are commonly placed on bridges, e.g. Chen et al. (2015). These barriers proved to be successful in sheltering vehicles and trucks from cross-winds on bridges and viaducts, e.g. Kozmar et al. (2012a), Chu et al. (2013).

Three major flow phenomena that are characteristic for wind barriers on bridges are (i) wind flow through wind-barrier gaps, (ii) shear layer separating from the top of the wind barrier placed at the leading edge of the bridge deck, (iii) flow recirculation downstream of the windward wind barrier, Telenta et al. (2014).

Major properties of wind barriers that determine their sheltering efficiency for vehicles are their porosity and height. Chen et al. (2015) indicated that large porosity of wind barriers is unfavorable for dynamic stability of vehicles on bridges, as the obtained velocity reduction may not be sufficient in case the wind-barrier gaps represent more than 50 % of the entire wind-barrier wall. Sheltering efficiency of wind barriers for vehicles is strongly affected by the wind-barrier height, Chu et al. (2013). An optimal wind-barrier design with respect to the vehicle sheltering for the wind perpendicular to bridge decks is considered the one with 30% porosity and 5 m height, e.g. Kozmar et al. (2014).

While the protective effects of wind barriers for vehicles are fairly known, their influence on aerodynamic forces and aerodynamic stability of bridges is rather unknown. Only several studies considered aerodynamic forces for bridges with wind barriers, Guo et al. (2015). The effect of bird-protection barriers on aerodynamic and aeroelastic behavior of high-speed train bridges is reported in Ogueta-Gutiérrez et al. (2014).

As previous studies, e.g. Jones et al. (1995) and Mannini et al. (2016), proved that even a small change in the design of the bridge-deck cross section may trigger unstable oscillations, it is anticipated that placing the barriers on bridges will affect their aeroelastic stability. Wind barriers were in fact observed to cause shedding of vortices on the top surface of the bridge deck, e.g. Avila-Sanchez et al. (2016), which may cause vortex-induced instability of bridge decks in case the frequency of the shed vortices is equal to the heave natural frequency of the bridge deck. Wind barriers cause the vortex-shedding frequency of the twin-box bridge-deck section to decrease and they enhance the flow separation, Laima et al. (2018). An addition of the horizontally placed wind barriers to the vertical wind barriers may suppress the vortex-induced vibrations; however, it may initiate the flutter instability, Yang et al. (2016).

Wind barriers are commonly characterized by their porosity and height, which are optimized for wind and terrain characteristics at a bridge site. At this moment, it is not completely known whether and to what extent the aerodynamic and aeroelastic characteristics of cable-supported bridges alter due to changes in wind-barrier porosity and height.

Wind barriers are commonly placed at the windward (upstream) edge of the bridge decks only, e.g. Kozmar et al. (2014), because in most areas strong cross winds blow on bridges predominantly from one direction and it is necessary to protect vehicles only for the dominant wind direction. However, to further assess other arrangements of wind barriers and their effects on aerodynamic stability of bridges, it is necessary to analyze dynamic behavior of bridges for wind barriers placed at the leeward bridge-deck edge as well as for both windward and leeward bridge-deck edges. This is required because long-span cable-supported bridges are commonly built to stay in service for decades and the predominant wind direction may alter over years, for example due to climate change or urban development. This means that the windward wind barrier may eventually become the leeward wind barrier and vice versa. In some areas, wind commonly blows from various directions, so it is anyway

necessary to place wind barriers at both the windward and leeward bridge-deck edges to protect vehicles for all wind directions, e.g. Chen et al. (2015).

1.4. Research objectives and hypotheses

The present thesis focuses on the effects of wind barriers on aerodynamic characteristics of three typical long-span cable-supported bridge decks and their sensitivity to self-excited vibrations. Wind-barrier models with different porosities and heights were placed at the bridge-deck section models in various arrangements (windward, leeward, both windward and leeward).

Aerodynamic drag and lift force and the pitch moment coefficients were determined for various flow incidence angles. The susceptibility of the studied bridge-deck sections to galloping was analyzed using the quasi-steady approach. The aerodynamic stability of bridges with respect to flutter was analyzed using the free-vibration tests, while the critical flow velocity for flutter was determined using the eigenvalue analysis. The analysis of the results is supported by the flow characterization around the bridge-deck sections.

Research hypotheses are:

(i) The dynamic stability of bridge decks deteriorates and the critical flutter wind velocity decreases in case the bridges are equipped with wind barriers;

(ii) A decrease in the porosity of roadway wind barrier deteriorates the dynamic stability of bridge decks;

(iii) Aerodynamic drag force of bridge decks increases in case the bridges are equipped with wind barriers.

This thesis provides insights into previously unknown aerodynamic and aeroelastic effects of roadway wind barriers on cable-supported bridges. The focus is on height and porosity of wind barriers, their arrangement on bridge-deck sections, the effects of wind turbulence and aerodynamic shape of bridge decks.

Chapter 2

Mathematical models for wind effects on cable-supported bridges

Mathematical models for the analysis of the static and dynamic response of bridge-deck sections to the wind flow. Dimensionless aerodynamic coefficients for the analysis of average aerodynamic loads acting on the static bridge-deck sections. Analytical model based on the quasi-steady approach for the galloping phenomenon. Mathematical model for the two-degree-of-freedom flutter based on the equations of motion with external aerodynamic self-excited forces. Critical flutter velocity based on the eigenvalues analysis for the coupled system in the heave and pitch directions.

2.1. Aerodynamic forces and moments

Aerodynamics is a field of research dealing with the interaction of the moving air and solid objects. The air flow around an object creates a pressure field on the object surface. The resultant force acting on the object due to the air motion,

$$F_i = \int_S \sigma_{ji} \cdot n_j \mathrm{dS} = -\int_S p \cdot n_i \mathrm{dS} + \int_S \Sigma_{ji}\, n_j \mathrm{dS}, \tag{2.1}$$

where $-\int_S p \cdot n_i \mathrm{dS}$ is the pressure force component, and $\int_S \Sigma_{ji}\, n_j \mathrm{dS}$ is the viscous force component. In the two-dimensional flow, the resultant integral forces are commonly decomposed into two components, the drag force F_D acting in the main flow direction, and the lift force F_L acting perpendicularly (vertically) to the main flow direction. They are commonly presented as dimensionless coefficients,

$$C_D = \frac{F_D}{\frac{1}{2}\rho v^2 A}, \tag{2.2}$$

$$C_L = \frac{F_L}{\frac{1}{2}\rho v^2 A}, \tag{2.3}$$

where C_D and C_L are aerodynamic drag and lift force coefficients, respectively; v is average freestream flow velocity, ρ is air density, A is reference area. These two forces yield the aerodynamic pitch moment M, hence the aerodynamic pitch moment coefficient C_M is,

$$C_M = \frac{M}{\frac{1}{2}\rho v^2 A L}, \tag{2.4}$$

where L is the characteristic object length.

The integral average aerodynamic forces are important for the overall static stability of bridges and its structural components, Xu et al. (2010). The aerodynamic coefficients may be used to calculate bridge susceptibility to dynamic instabilities using the quasi-steady approach, i.e. the aerodynamic forces acting on the moving body vary with the incoming flow velocity in the same manner as for the steady flow, e.g. Simiu and Scanlan (1996), Xu (2013).

The static aerodynamic coefficients in the present study are determined at various flow incidence angles α using the following equations,

$$C_D(\alpha) = \frac{F_D(\alpha)}{\frac{1}{2}\rho v^2 HL}, \tag{2.5}$$

$$C_L(\alpha) = \frac{F_L(\alpha)}{\frac{1}{2}\rho v^2 BL}, \tag{2.6}$$

$$C_M(\alpha) = \frac{M(\alpha)}{\frac{1}{2}\rho v^2 B^2 L}, \tag{2.7}$$

where H, B and L are bridge-deck height, width and length, respectively.

The sign convention for aerodynamic forces and moments along with displacements is reported in Figure 8.

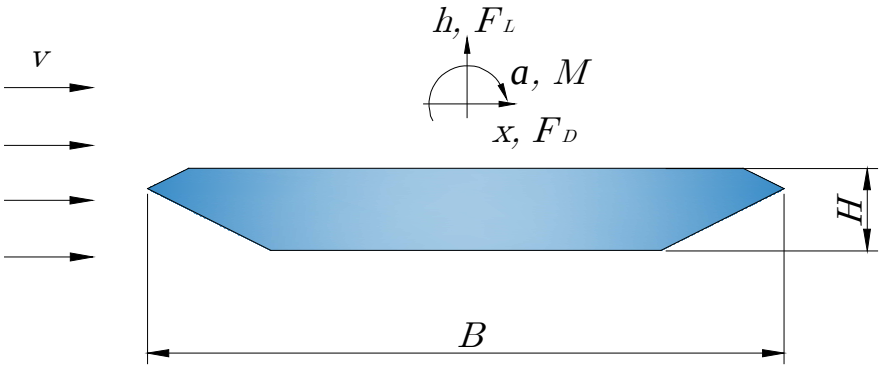

Figure 8: Sign convention for aerodynamic loads and displacements of bridge decks.

2.2. Galloping

The frequency of body motion for the galloping oscillations is rather low, it can be adopted that the aerodynamic forces are acting on a body in the same manner as for a steady flow, e.g. Simiu and Scanlan (1996). Therefore, galloping of bridge-deck sections is commonly analyzed using the quasi-steady approach. In order to outline this approach, a bridge-deck section subjected to the flow is schematically presented in Figure 9. It is assumed to be rigid, i.e. not flexible, while the incidence angle of the flow velocity v_r is α.

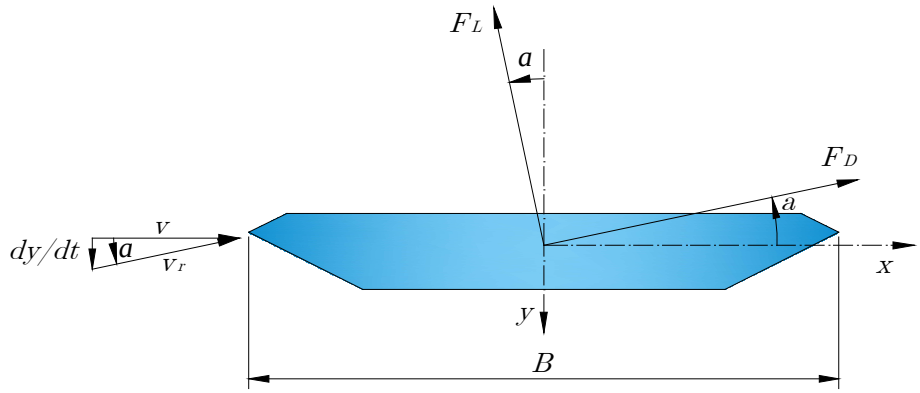

Figure 9: Aerodynamic lift and drag forces experienced by the bridge-deck section subjected to the flow.

The aerodynamic drag and lift forces of bridge-deck sections may be expressed using the force coefficients as,

$$F_D(\alpha) = \frac{1}{2}\rho v_r^2 B C_D(\alpha)\frac{H}{B}, \tag{2.8}$$

$$F_L(\alpha) = \frac{1}{2}\rho v_r^2 B C_L(\alpha). \tag{2.9}$$

where $F_D(\alpha)$ and $F_L(\alpha)$ are drag and lift force, respectively. The vertical force acting in the y-axis direction can be expressed as a function of aerodynamic drag and lift forces,

$$F_y(\alpha) = -F_D(\alpha)\sin\alpha - F_L(\alpha)\cos\alpha, \tag{2.10}$$

$$F_y(\alpha) = -\frac{1}{2}\rho v_r^2 B\left(C_D(\alpha)\frac{H}{B}\sin\alpha + C_L(\alpha)\cos\alpha\right). \tag{2.11}$$

The flow velocity parallel with the x-axis is $v = v_r\cos(\alpha)$, therefore,

$$F_y(\alpha) = -\frac{1}{2}\rho U^2 B\left(C_D(\alpha)\frac{H}{B}\tan\alpha + C_L(\alpha)\sec\alpha\right). \tag{2.12}$$

In case it is assumed that the bridge-deck section oscillates in the across-wind direction (y-direction), under assumption that the oscillation is small, α can be expressed as,

$$\alpha \approx \frac{\frac{dy}{dt}}{v} \to 0. \tag{2.13}$$

The vertical force can be written as Taylor expansion function,

$$F_y(\alpha) = F_y(\alpha = 0) + \left.\frac{dF_y}{d\alpha}\right|_{\alpha=0} \cdot \alpha. \tag{2.14}$$

First term in the Eq. (2.14) is given as,

$$\begin{aligned} F_y(\alpha = 0) &= -\frac{1}{2}\rho v^2 B\left(C_D(\alpha = 0)\frac{H}{B}\tan 0 + C_L(\alpha = 0)\sec 0\right), \\ F_y(\alpha = 0) &= -\frac{1}{2}\rho v^2 B \cdot C_L(\alpha = 0). \end{aligned} \tag{2.15}$$

This component can be neglected as it is the static component. The second term in Eq. (2.14) is given as,

$$\left.\frac{dF_y}{d\alpha}\right|_{\alpha=0} = -\frac{1}{2}\rho U^2 B\left(\left.\frac{dC_D}{d\alpha}\right|_{\alpha=0}\frac{H}{B}\cdot\tan 0 + C_D(\alpha = 0)\frac{H}{B}\cdot\sec^2 0 + ..\right. \tag{2.16}$$

$$\left. .. + \left.\frac{dC_L}{d\alpha}\right|_{\alpha=0}\cdot\sec 0 + C_L(\alpha = 0)\cdot\sec 0\tan 0\right),$$

$$\left.\frac{dF_y}{d\alpha}\right|_{\alpha=0} = -\frac{1}{2}\rho v^2 B\left(C_D(\alpha = 0)\frac{H}{B} + \left.\frac{dC_L}{d\alpha}\right|_{\alpha=0}\right). \tag{2.17}$$

It follows that the force in the *y*-direction is,

$$F_y(\alpha) = -\frac{1}{2}\rho v^2 B\left(C_D(\alpha)\frac{H}{B} + \left.\frac{dC_L}{d\alpha}\right|_{\alpha=0}\right)\cdot\frac{\dot{y}}{v}. \tag{2.18}$$

Eq. 2.18 is a quasi-steady expression of a bridge-deck aerodynamic force acting in the *y*-direction. The equation of motion in the direction normal to the main flow direction (assuming the body is elastically sprung and has linear mechanical damping) is,

$$m\left(\ddot{y} + 2\xi_y\omega_y\dot{y} + \omega_y^2 y\right) = F_y(\alpha), \tag{2.19}$$

where m is mass of system, ξ_y is critical damping ratio in the vertical direction, ω_y is natural frequency of oscillation in the vertical direction. The external force to the system is,

$$m\left(\ddot{y} + 2\xi_y\omega_y\dot{y} + \omega_y^2 y\right) = -\frac{1}{2}\rho v^2 B\left(\left(C_D(\alpha)\frac{H}{B} + \frac{dC_L}{d\alpha}\right)\Big|_{\alpha=0}\right)\cdot\frac{\dot{y}}{v}, \tag{2.20}$$

$$m\left(\ddot{y} + \dot{y}\left(2\xi_y\omega_y + \frac{1}{2}\rho v B\left(\left(C_D(\alpha)\frac{H}{B} + \frac{dC_L}{d\alpha}\right)\Big|_{\alpha=0}\right)\right) + \omega_y^2 y\right) = 0. \tag{2.21}$$

Net damping of the system is,

$$k = 2\xi_y \omega_y + \frac{1}{2}\rho v B\left(\left(C_D(\alpha)\frac{H}{B} + \frac{dC_L}{d\alpha}\right)\bigg|_{\alpha=0}\right). \tag{2.22}$$

Mechanical damping of the system denoted as $2\xi_y\omega_y$ is positive by its definition; therefore, the net damping of the system can be negative only in case,

$$\left(C_D(\alpha)\frac{H}{B} + \frac{dC_L}{d\alpha}\right)\bigg|_{\alpha=0} < 0. \tag{2.23}$$

This condition is known as the Glauert-den Hartog criterion. It is a necessary condition for galloping instability to occur. A sufficient condition for galloping instability is,

$$\left(C_D(\alpha)\frac{H}{B} + \frac{dC_L}{d\alpha}\right)\bigg|_{\alpha=0} < -\frac{\xi_y \omega_y}{\rho v B}. \tag{2.24}$$

The bridge-deck section susceptibility to galloping is therefore analyzed by evaluating its lift and drag force coefficients at various flow incidence angles.

2.3. Flutter

Flutter is generally a nonlinear problem; however, it is possible to analyze it as linear elastic, i.e. the vibrating structure can be assumed to be a linear elastic system for relatively small vibration amplitudes.

Mathematical modeling of the flutter phenomenon is performed through the analysis of the equations of motion. Equation of motion for a SDOF discrete mechanical system can be given with respect to the 2nd Newton's law,

$$m\ddot{x} = f(t,\ x,\ \dot{x}) + F(t), \tag{2.25}$$

where m is mass of a system, x is displacement with its time derivations, t is time, $f(t,\ x,\ \dot{x})$ are forces acting in the system, $F(t)$ are external forces acting on the system. The function f can be expanded into Taylor series around the static equilibrium point x_s,

$$f(t,\ x,\ \dot{x}) = f(t,\ x_s,\ 0) + \frac{\partial f(t,\ x_s,\ 0)}{\partial x}(x - x_s) + \frac{\partial f(t,\ x_s,\ 0)}{\partial \dot{x}}\dot{x} + \ldots \tag{2.26}$$

Neglecting the higher order derivatives, the equation of motion is,

$$m\ddot{x} = f(t,\ x_s,\ 0) + \frac{\partial f(t,\ x_s,\ 0)}{\partial x}(x - x_s) + \frac{\partial f(t,\ x_s,\ 0)}{\partial \dot{x}}\dot{x} + F(t), \tag{2.27}$$

The static equilibrium yields $f(t,\ x_s,\ 0) = 0$,

$$m\ddot{x} - \frac{\partial f\left(t,\ x_s,\ 0\right)}{\partial x}\left(x - x_s\right) - \frac{\partial f\left(t,\ x_s,\ 0\right)}{\partial \dot{x}}\dot{x} = F\left(t\right). \tag{2.28}$$

The time dependent coefficients in the equation of motion for the static equilibrium are,

$$k(t) = -\frac{\partial f}{\partial \dot{x}}\left(t,\ x_s,\ 0\right), \tag{2.29}$$

$$c(t) = -\frac{\partial f}{\partial x}\left(t,\ x_s,\ 0\right). \tag{2.30}$$

It accordingly follows,

$$m\ddot{x} + k\dot{x} + cx = F\left(t\right). \tag{2.31}$$

This is a linear homogenous differential equation of motion for a SDOF discrete mechanical system excited by a general external force $F(t)$. The equation of motion can be alternatively given as,

$$m\ddot{x}\left(t\right) + 2\xi\omega_n m\dot{x}\left(t\right) + \omega_n^2 mx\left(t\right) = F\left(t\right), \tag{2.32}$$

where ξ is dimensionless critical damping ratio,

$$\xi = \frac{k}{2\sqrt{mc}}, \tag{2.33}$$

while ω_n is undamped circular frequency of the system oscillation,

$$\omega_n = \sqrt{\frac{c}{m}}. \tag{2.34}$$

In case a two-degree-of-freedom (2DOF) mechanically independent system with x_1 and x_2 degrees of freedom is considered, the equations of motion are commonly provided as a matrix,

$$\begin{bmatrix} m & 0 \\ 0 & m \end{bmatrix}\begin{bmatrix} \ddot{x}_1 \\ \ddot{x}_2 \end{bmatrix} + \begin{bmatrix} k_1 & 0 \\ 0 & k_2 \end{bmatrix}\begin{bmatrix} \dot{x}_1 \\ \dot{x}_2 \end{bmatrix} + \begin{bmatrix} c_1 & 0 \\ 0 & c_2 \end{bmatrix}\begin{bmatrix} x_1\left(t\right) \\ x_2\left(t\right) \end{bmatrix} = \begin{bmatrix} F_1\left(t\right) \\ F_2\left(t\right) \end{bmatrix}, \tag{2.35}$$

or in a symbolic way,

$$\mathrm{M}\ddot{\mathrm{x}}\left(t\right) + \mathrm{K}\dot{\mathrm{x}}\left(t\right) + \mathrm{C}\mathrm{x}\left(t\right) = \mathrm{F}\left(t\right). \tag{2.36}$$

M is mass matrix, K is damping matrix, C is stiffness matrix, x is displacement vector, F is vector of external forces.

The vertical and torsional vibration modes are commonly analyzed when studying dynamic stability of long-span bridges, whereas the lateral vibration mode is commonly considered to have a minor influence and it is therefore neglected, e.g. Dyrbye and Hansen (1996). Dynamic response of a bridge deck moving in the 2DOF mechanically independent system can be mathematically expressed using the general equations of motion,

$$\begin{aligned} m\left[\ddot{h}(t)+2\xi_{h0}\omega_{h0}\dot{h}(t)+\omega_{h0}^{2}h(t)\right] &= F_{Ls}(t), \\ I\left[\ddot{\alpha}(t)+2\xi_{\alpha 0}\omega_{\alpha 0}\dot{\alpha}(t)+\omega_{\alpha 0}^{2}\alpha(t)\right] &= M_{s}(t), \end{aligned} \tag{2.37}$$

where h and α are heave and pitch displacement, I is mass moment of inertia. ξ_{h0} and $\xi_{\alpha 0}$ are structural critical damping ratios in the heave and pitch motions, ω_{h0} and $\omega_{\alpha 0}$ are structural-damped natural circular frequencies in the heave and pitch motions, respectively. External forces acting on bridge decks are the aerodynamic self-excited lift force and the pitch moment, i.e. $L_s(t)$ and $M_s(t)$, respectively. They can be expanded into Taylor series around the equilibrium point that is considered $h = \alpha = 0$,

$$F_{Ls} = F_{Ls}(h=\alpha=0)+\frac{\partial F_{Ls}}{\partial h}h+\frac{\partial F_{Ls}}{\partial \alpha}\alpha+\frac{\partial F_{Ls}}{\partial \dot{h}}\dot{h}+\frac{\partial F_{Ls}}{\partial \dot{\alpha}}\dot{\alpha}, \tag{2.38}$$

$$M_{s} = M_{s}(h=\alpha=0)+\frac{\partial M_{s}}{\partial h}h+\frac{\partial M_{s}}{\partial \alpha}\alpha+\frac{\partial M_{s}}{\partial \dot{h}}\dot{h}+\frac{\partial M_{s}}{\partial \dot{\alpha}}\dot{\alpha}. \tag{2.39}$$

The static components of the self-excited aerodynamic lift force and the pitch moment are not considered. Excessively large displacements may influence a linear dependence of the self-excited aerodynamic forces on the motion of the bridge-deck section models, e.g. Diana et al. (2008), which is the assumption of the linear flutter model because the self-excited aerodynamic forces are commonly linearized with respect to the static position. The self-excited aerodynamic lift force and the pitch moment are generally non-linear functions of displacements in the vertical and torsional directions and their derivations.

The second and higher-order derivatives are commonly neglected in bridge engineering. Scanlan and Tomko (1971) expressed the derivatives of the self-excited aerodynamic lift force and the pitch moment using the dimensionless coefficients H_i^* and A_i^* (i = 1, 2, 3, 4) as a function of the dimensionless reduced frequency of the system K,

$$K = \frac{\omega B}{v_\infty^2}, \tag{2.40}$$

where ω is natural frequency of oscillation in the heave or pitch motions. The self-excited aerodynamic lift force expanded in Taylor series is,

$$\frac{\partial F_{Ls}}{\partial \dot{h}} = \frac{1}{2}\rho B^2 L \omega_h H_1^*(K) = \frac{1}{2}\rho v_\infty^2 BL \frac{K}{v_\infty} H_1^*(K), \tag{2.41}$$

$$\frac{\partial F_{Ls}}{\partial \dot{\alpha}} = \frac{1}{2}\rho B^3 L \omega_\alpha H_2^*(K) = \frac{1}{2}\rho v_\infty^2 BL \frac{KB}{v_\infty} H_2^*(K), \tag{2.42}$$

$$\frac{\partial F_{Ls}}{\partial \alpha} = \frac{1}{2}\rho B^3 L \omega_\alpha^2 H_3^*(K) = \frac{1}{2}\rho v_\infty^2 BLK^2 H_3^*(K), \tag{2.43}$$

$$\frac{\partial F_{Ls}}{\partial h} = \frac{1}{2}\rho B^2 L \omega_h^2 H_4^*(K) = \frac{1}{2}\rho v_\infty^2 BL \frac{K^2}{B} H_4^*(K). \tag{2.44}$$

The self-excited aerodynamic pitch moment is,

$$\frac{\partial M_s}{\partial \dot{h}} = \frac{1}{2}\rho B^3 L \omega_h A_1^*(K) = \frac{1}{2}\rho v_\infty^2 B^2 L \frac{K}{v_\infty} A_1^*(K), \tag{2.45}$$

$$\frac{\partial M_s}{\partial \dot{\alpha}} = \frac{1}{2}\rho B^4 L \omega_\alpha A_2^*(K) = \frac{1}{2}\rho v_\infty^2 B^2 L \frac{KB}{v_\infty} A_2^*(K), \tag{2.46}$$

$$\frac{\partial M_s}{\partial \alpha} = \frac{1}{2}\rho B^4 L \omega_\alpha^2 A_3^*(K) = \frac{1}{2}\rho v_\infty^2 B^2 LK^2 A_3^*(K), \tag{2.47}$$

$$\frac{\partial M_s}{\partial h} = \frac{1}{2}\rho B^3 L \omega_h^2 A_4^*(K) = \frac{1}{2}\rho v_\infty^2 B^2 L \frac{K^2}{B} A_4^*(K). \tag{2.48}$$

Dimensionless coefficients H_i^* and A_i^* (i = 1, 2, 3, 4) are aeroelastic coefficients of a system, i.e. FDs. They are indicators of the bridge-deck flutter stability. The self-excited aerodynamic lift force and the pitch moment are provided using the FDs as,

$$F_{Ls} = \frac{1}{2}\rho v_\infty^2 BL\left(\frac{K}{v_\infty} H_1^*(K)\dot{h} + \frac{KB}{v_\infty} H_2^*(K)\dot{\alpha} + K^2 H_3^*(K)\alpha + \frac{K^2}{B} H_4^*(K)h\right), \tag{2.49}$$

$$M_s = \frac{1}{2}\rho v_\infty^2 B^2 L\left(\frac{K}{v_\infty} A_1^*(K)\dot{h} + \frac{KB}{v_\infty} A_2^*(K)\dot{\alpha} + K^2 A_3^*(K)\alpha + \frac{K^2}{B} A_4^*(K)h\right). \tag{2.50}$$

The equations of motion of the bridge-deck 2DOF system moving in the vertical and pitch directions with the external flow excitation,

$$
\begin{aligned}
&m\left[\ddot{h}(t)+2\xi_{h0}\omega_{h0}\dot{h}(t)+\omega_{h0}^2 h(t)\right]=\\
&=\frac{1}{2}\rho v_\infty^2 BL\left(\frac{K}{v_\infty}H_1^*(K)\dot{h}+\frac{KB}{v_\infty}H_2^*(K)\dot{\alpha}+K^2H_3^*(K)\alpha+\frac{K^2}{B}H_4^*(K)h\right),\\
&I\left[\ddot{\alpha}(t)+2\xi_{\alpha0}\omega_{\alpha0}\dot{\alpha}(t)+\omega_{\alpha0}^2\alpha(t)\right]=\\
&=\frac{1}{2}\rho v_\infty^2 B^2 L\left(\frac{K}{v_\infty}A_1^*(K)\dot{h}+\frac{KB}{v_\infty}A_2^*(K)\dot{\alpha}+K^2A_3^*(K)\alpha+\frac{K^2}{B}A_4^*(K)h\right).
\end{aligned}
\tag{2.51}
$$

These are the general equations of motion for bridge decks moving in the 2DOF system in which the self-excited aerodynamic lift force and the pitch moment are expressed using the dimensionless FDs and a reduced frequency of the system. The self-excited aerodynamic lift force and the pitch moment are coupled in the vertical and torsional directions. Due to this coupling, flutter instability may occur for bridges that proved to be dynamically stable in separate SDOF system tests.

The governing equation of motion for the bridge-deck 2DOF dynamic system in matrix form,

$$
\begin{aligned}
&\begin{bmatrix} m & 0\\ 0 & I\end{bmatrix}\begin{bmatrix}\ddot{h}\\ \ddot{\alpha}\end{bmatrix}+\begin{bmatrix} 2m\xi_{h0}\omega_{h0} & 0\\ 0 & 2m\xi_{\alpha0}\omega_{\alpha0}\end{bmatrix}\begin{bmatrix}\dot{h}\\ \dot{\alpha}\end{bmatrix}+\begin{bmatrix} m\omega_{h0}^2 & 0\\ 0 & m\omega_{\alpha0}^2\end{bmatrix}\begin{bmatrix}h\\ \alpha\end{bmatrix}=\\
&=\begin{bmatrix}\frac{1}{2}\rho v_\infty^2 BL\frac{K}{v_\infty}H_1^*(K) & \frac{1}{2}\rho v_\infty^2 BL\frac{KB}{v_\infty}H_2^*(K)\\ \frac{1}{2}\rho v_\infty^2 B^2 L\frac{K}{v_\infty}A_1^*(K) & \frac{1}{2}\rho v_\infty^2 B^2 L\frac{KB}{v_\infty}A_2^*(K)\end{bmatrix}\begin{bmatrix}\dot{h}\\ \dot{\alpha}\end{bmatrix}+\\
&+\begin{bmatrix}\frac{1}{2}\rho v_\infty^2 BL\frac{K^2}{B}H_4^*(K) & \frac{1}{2}\rho v_\infty^2 BLK^2H_3^*(K)\\ \frac{1}{2}\rho v_\infty^2 B^2 L\frac{K^2}{B}A_4^*(K) & \frac{1}{2}\rho v_\infty^2 B^2 LK^2A_3^*(K)\end{bmatrix}\begin{bmatrix}h\\ \alpha\end{bmatrix},
\end{aligned}
\tag{2.52}
$$

or in a symbolic form,

$$
\mathrm{M}\ddot{\mathrm{x}}+\mathrm{K}^{\mathrm{m}}\dot{\mathrm{x}}+\mathrm{C}^{\mathrm{m}}\mathrm{x}=\mathrm{K}^{\mathrm{a}}\dot{\mathrm{x}}+\mathrm{C}^{\mathrm{a}}\mathrm{x}. \tag{2.53}
$$

where M is mass matrix,

$$
\mathrm{M}=\begin{bmatrix} m & 0\\ 0 & I\end{bmatrix}. \tag{2.54}
$$

K^{m} is mechanical (structural) damping matrix,

$$
\mathrm{K}^{\mathrm{m}}=\begin{bmatrix} 2m\xi_{h0}\omega_{h0} & 0\\ 0 & 2m\xi_{\alpha0}\omega_{\alpha0}\end{bmatrix}. \tag{2.55}
$$

C^m is mechanical (structural) stiffness matrix,

$$C^m = \begin{bmatrix} m\omega_{h0}^2 & 0 \\ 0 & m\omega_{\alpha 0}^2 \end{bmatrix}. \tag{2.56}$$

x is displacement matrix,

$$x = \begin{bmatrix} h \\ \alpha \end{bmatrix}. \tag{2.57}$$

K^a is aerodynamic damping matrix,

$$K^a = \begin{bmatrix} \frac{1}{2}\rho v_\infty^2 BL\frac{K}{v_\infty}H_1^*(K) & \frac{1}{2}\rho v_\infty^2 BL\frac{KB}{v_\infty}H_2^*(K) \\ \frac{1}{2}\rho v_\infty^2 B^2 L\frac{K}{v_\infty}A_1^*(K) & \frac{1}{2}\rho v_\infty^2 B^2 L\frac{KB}{v_\infty}A_2^*(K) \end{bmatrix}. \tag{2.58}$$

C^a is aerodynamic stiffness matrix,

$$C^a = \begin{bmatrix} \frac{1}{2}\rho v_\infty^2 BL\frac{K^2}{B}H_4^*(K) & \frac{1}{2}\rho v_\infty^2 BLK^2 H_3^*(K) \\ \frac{1}{2}\rho v_\infty^2 B^2 L\frac{K^2}{B}A_4^*(K) & \frac{1}{2}\rho v_\infty^2 B^2 LK^2 A_3^*(K) \end{bmatrix}. \tag{2.59}$$

The aerodynamic stiffness and damping matrices can be combined with the structural matrices,

$$\begin{bmatrix} m & 0 \\ 0 & I \end{bmatrix}\begin{bmatrix} \ddot{h} \\ \ddot{\alpha} \end{bmatrix} + \begin{bmatrix} 2m\xi_{h0}\omega_{h0} - \frac{1}{2}\rho B^2 L\omega_h H_1^*(K) & -\frac{1}{2}\rho B^3 L\omega_\alpha H_2^*(K) \\ -\frac{1}{2}\rho B^3 L\omega_h A_1^*(K) & 2I\xi_{\alpha 0}\omega_{\alpha 0} - \frac{1}{2}\rho B^4 L\omega_\alpha A_2^*(K) \end{bmatrix}\begin{bmatrix} \dot{h} \\ \dot{\alpha} \end{bmatrix} + \\ + \begin{bmatrix} m\omega_{h0}^2 - \frac{1}{2}\rho B^2 L\omega_h^2 H_4^*(K) & -\frac{1}{2}\rho B^3 L\omega_\alpha^2 H_3^*(K) \\ -\frac{1}{2}\rho B^3 L\omega_h^2 A_4^*(K) & I\omega_{\alpha 0}^2 - \frac{1}{2}\rho B^4 L\omega_\alpha^2 A_3^*(K) \end{bmatrix}\begin{bmatrix} h \\ \alpha \end{bmatrix} = 0. \tag{2.60}$$

This equation is commonly given as,

$$\begin{bmatrix} 1 & 0 \\ 0 & 1 \end{bmatrix}\begin{bmatrix} \ddot{h} \\ \ddot{\alpha} \end{bmatrix} + \begin{bmatrix} 2\xi_{h0}\omega_{h0} - \frac{\rho B^2 L}{2m}\omega_h H_1^*(K) & -\frac{\rho B^3 L}{2m}\omega_\alpha H_2^*(K) \\ -\frac{\rho B^3 L}{2I}\omega_h A_1^*(K) & 2\xi_{\alpha 0}\omega_{\alpha 0} - \frac{\rho B^4 L}{2I}\omega_\alpha A_2^*(K) \end{bmatrix}\begin{bmatrix} \dot{h} \\ \dot{\alpha} \end{bmatrix} + \\ + \begin{bmatrix} \omega_{h0}^2 - \frac{\rho B^2 L}{2m}\omega_h^2 H_4^*(K) & -\frac{\rho B^3 L}{2m}\omega_\alpha^2 H_3^*(K) \\ -\frac{\rho B^3 L}{2I}\omega_h^2 A_4^*(K) & \omega_{\alpha 0}^2 - \frac{\rho B^4 L}{2I}\omega_\alpha^2 A_3^*(K) \end{bmatrix}\begin{bmatrix} h \\ \alpha \end{bmatrix} = 0. \tag{2.61}$$

or in a symbolic form,

$$\ddot{\mathrm{x}} + \mathrm{K}^{\mathrm{e}}\dot{\mathrm{x}} + \mathrm{C}^{\mathrm{e}}\mathrm{x} = 0, \tag{2.62}$$

where K^{e} and C^{e} represent effective damping and stiffness matrices, respectively. These matrices are composed of the structural and aerodynamic terms,

$$\mathrm{K}^{\mathrm{e}} = \begin{bmatrix} 2\xi_{h0}\omega_{h0} - \dfrac{\rho B^2 L}{2m}\omega_h H_1^*(K) & -\dfrac{\rho B^3 L}{2m}\omega_\alpha H_2^*(K) \\ -\dfrac{\rho B^3 L}{2I}\omega_h A_1^*(K) & 2\xi_{\alpha 0}\omega_{\alpha 0} - \dfrac{\rho B^4 L}{2I}\omega_\alpha A_2^*(K) \end{bmatrix}, \tag{2.63}$$

$$\mathrm{C}^{\mathrm{e}} = \begin{bmatrix} \omega_{h0}^2 - \dfrac{\rho B^2 L}{2m}\omega_h^2 H_4^*(K) & -\dfrac{\rho B^3 L}{2m}\omega_\alpha^2 H_3^*(K) \\ -\dfrac{\rho B^3 L}{2I}\omega_h^2 A_4^*(K) & \omega_{\alpha 0}^2 - \dfrac{\rho B^4 L}{2I}\omega_\alpha^2 A_3^*(K) \end{bmatrix}. \tag{2.64}$$

FDs obtained from the diagonal terms of the stiffness and damping matrices are direct FDs. The remaining FDs extracted from non-diagonal terms of the matrices are non-direct FDs; they are obtained from the 2DOF system only, as they represent the influence of the heave on the pitch motion and vice versa,

$$\begin{aligned} H_1^*(K) &= -\frac{2m}{\rho B^2 L\omega_h}\left(\mathrm{K}_{11}^{\mathrm{e}} - \mathrm{K}_{11}^{\mathrm{m}}\right), & H_2^*(K) &= -\frac{2m}{\rho B^3 L\omega_\alpha}\left(\mathrm{K}_{12}^{\mathrm{e}} - \mathrm{K}_{12}^{\mathrm{m}}\right), \\ H_3^*(K) &= -\frac{2m}{\rho B^3 L\omega_\alpha^2}\left(\mathrm{C}_{12}^{\mathrm{e}} - \mathrm{C}_{12}^{\mathrm{m}}\right), & H_4^*(K) &= -\frac{2m}{\rho B^2 L\omega_h^2}\left(\mathrm{C}_{11}^{\mathrm{e}} - \mathrm{C}_{11}^{\mathrm{m}}\right), \\ A_1^*(K) &= -\frac{2I}{\rho B^3 L\omega_h}\left(\mathrm{K}_{21}^{\mathrm{e}} - \mathrm{K}_{21}^{\mathrm{m}}\right), & A_2^*(K) &= -\frac{2I}{\rho B^4 L\omega_\alpha}\left(\mathrm{K}_{22}^{\mathrm{e}} - \mathrm{K}_{22}^{\mathrm{m}}\right), \\ A_3^*(K) &= -\frac{2I}{\rho B^4 L\omega_\alpha^2}\left(\mathrm{C}_{22}^{\mathrm{e}} - \mathrm{C}_{22}^{\mathrm{m}}\right), & A_4^*(K) &= -\frac{2I}{\rho B^3 L\omega_h^2}\left(\mathrm{C}_{21}^{\mathrm{e}} - \mathrm{C}_{21}^{\mathrm{m}}\right). \end{aligned} \tag{2.65}$$

FDs are obtained from the generalized system stiffness and damping matrices with the flow present as well as from the structural stiffness and damping matrices. The emphasis is commonly on direct FDs, as they are considered to provide a better insight into flutter sensitivity of bridge decks, e.g. Xu et al. (2014).

While eight FDs extracted from the 2DOF tests are commonly analyzed for bridges, e.g. Wu et al. (2012), some studies emphasize a role of the lateral motion (horizontal to the main flow) on the overall flutter characteristics of bridge decks, e.g. Singh et al. (1996), Xu et al. (2014c), Xu et al. (2016). The drag self-excited force related derivatives (P-derivatives) are reported to have stabilizing effect on flutter, Zhang and Brownjohn (2005), while their influence on the critical flutter velocity of bluff bridges is relatively minor, Xu (2015).

For the streamlined bodies such as airfoils, the self-excited loads, i.e. FDs, can be determined using the analytical expressions under several assumptions, Theodorsen (1935). For bluff bodies such as bridges, the self-excited aerodynamic forces must be derived from dynamic tests using several techniques of excitation, e.g. Dyrbye and Hansen (1996).

2.4. Dynamic response identification

To evaluate C^e and K^e matrices from the dynamic response of bridge decks and consequently the FDs, the Modified Unifying Least Squares (ULS) identification method was used. This procedure is based on the least squares method - it was originally developed by Gu et al. (2000) and Chen et al. (2002) and further modified by Bartoli et al. (2009), Král (2011).

The initial values of parameters used to start the iteration loop were determined by the procedure following from the main principle of the ULS method itself, but operating with two parameters for each DOF separately. Using a free-decay time history signal in quiescent air, the first set of the initial parameter values related to the SDOF system was specified. The identical procedure was performed for the heave SDOF system.

This approach yields four parameters (frequency of oscillation in the heave and pitch motions as well as damping ratios in the heave and pitch motions) necessary to use the ULS method. This method is rather robust at small flow velocities, while at large flow velocities the heave and pitch responses interact considerably, and it is often not possible to obtain a complete convergence of the results.

The estimated dynamic response of bridge-deck free decayed oscillations is,

$$\hat{h}_m = \sum_{r=1}^{2} \left(A_{hr} \mathrm{e}^{\lambda_r m \Delta t} + A_{hr}^* \mathrm{e}^{\lambda_r^* m \Delta t} \right), \tag{2.66}$$

$$\hat{\alpha}_m = \sum_{r=1}^{2} \left(A_{\alpha r} \mathrm{e}^{\lambda_r m \Delta t} + A_{\alpha r}^* \mathrm{e}^{\lambda_r^* m \Delta t} \right), \tag{2.67}$$

where m is the m^{th} sample in the time history, Δt is time step, λ_r and A_r are,

$$\lambda_r = \alpha_r + j\beta_r, \ \lambda_r^* = \alpha_r - j\beta_r, \tag{2.68}$$

$$A_r = U_r + jV_r, \ A_r^* = U_r - jV_r. \tag{2.69}$$

The estimated responses are,

$$\hat{h}_m = 2\sum_{r=1}^{2} e^{\alpha_r m\Delta t}\left[U_{hr}\cos\left(\beta_r m\Delta t\right) - V_{hr}\sin\left(\beta_r m\Delta t\right)\right], \tag{2.70}$$

$$\hat{\alpha}_m = 2\sum_{r=1}^{2} e^{\alpha_r m\Delta t}\left[U_{\alpha r}\cos\left(\beta_r m\Delta t\right) - V_{\alpha r}\sin\left(\beta_r m\Delta t\right)\right]. \tag{2.71}$$

The least squares method is used to get an approximation of the measured dynamic responses,

$$e_{hm} = h_m - \hat{h}_m, \tag{2.72}$$

$$e_{\alpha m} = \alpha_m - \hat{\alpha}_m, \tag{2.73}$$

where e_{hm} and $e_{\alpha m}$ are error vectors between the estimated and measured values. Initial values $\alpha^{(1)}$ and $\beta^{(1)}$ were determined from the mechanical properties of the system. New coefficients were introduced to linearize the equations,

$$C_{rm}^{(i)} = 2e^{\alpha_r^{(i)} m\Delta t}\cos\left(\beta_r^{(i)} m\Delta t\right), \tag{2.74}$$

$$S_{rm}^{(i)} = 2e^{\alpha_r^{(i)} m\Delta t}\sin\left(\beta_r^{(i)} m\Delta t\right), \tag{2.75}$$

hence Eqs. (2.70) and (2.71) become,

$$\hat{h}_m = \sum_{r=1}^{2}\left(U_{hr}C_{rm} - V_{hr}S_{rm}\right), \tag{2.76}$$

$$\hat{\alpha}_m = \sum_{r=1}^{2}\left(U_{\alpha r}C_{rm} - V_{\alpha r}S_{rm}\right). \tag{2.77}$$

The objective function is,

$$\begin{aligned} J = &\left[\{h\} - \left([C]\{U_h\} - [S]\{V_h\}\right) + \{\alpha\} - \left([C]\{U_\alpha\} - [S]\{V_\alpha\}\right)\right]^{\mathrm{T}} \times \\ &\left[\{h\} - \left([C]\{U_h\} - [S]\{V_h\}\right) + \{\alpha\} - \left([C]\{U_\alpha\} - [S]\{V_\alpha\}\right)\right], \end{aligned} \tag{2.78}$$

that yields

$$\frac{\partial J}{\partial\{U_h\}} = 0,\ \ \frac{\partial J}{\partial\{V_h\}} = 0,\ \ \frac{\partial J}{\partial\{U_\alpha\}} = 0,\ \ \frac{\partial J}{\partial\{V_\alpha\}} = 0. \tag{2.79}$$

The system of equations as a matrix,

$$\begin{bmatrix} A & D \\ D & B \end{bmatrix}\begin{Bmatrix} U_h \\ V_h \end{Bmatrix} = \begin{Bmatrix} X_h \\ Y_h \end{Bmatrix}, \tag{2.80}$$

$$\begin{bmatrix} A & D \\ D & B \end{bmatrix}\begin{Bmatrix} U_\alpha \\ V_\alpha \end{Bmatrix} = \begin{Bmatrix} X_\alpha \\ Y_\alpha \end{Bmatrix}, \tag{2.81}$$

where,

$$A = [C]^{\mathrm{T}}[C], \quad B = [S]^{\mathrm{T}}[S], \quad D = -[C]^{\mathrm{T}}[S],$$
$$X_h = [C]^{\mathrm{T}}\{h\}, \quad X_\alpha = [C]^{\mathrm{T}}\{\alpha\}, \quad \mathrm{Y}_h = -[S]^{\mathrm{T}}\{h\}, \quad \mathrm{Y}_\alpha = -[S]^{\mathrm{T}}\{\alpha\}. \tag{2.82}$$

New values of α and β were calculated as,

$$\alpha_i^m = \alpha_i^{m-1} + \Delta_i, \ i = 1,2, \tag{2.83}$$

$$\beta_i^m = \beta_i^{m-1} + \Delta_i, \ i = 3,4. \tag{2.84}$$

The increments Δ_i (i=1, 2, 3, 4) were determined from the Taylor expansion of Eqs. (2.66) and (2.67) around α_i^{m-1} and β_i^{m-1} and neglecting the higher-order terms and implying $\partial J/\partial\Delta_i = 0$. The numerical method was considered to be completed when the absolute values of the Δ_i increment was smaller than the allowable error, which was adopted as 10^{-4} in this thesis.

2.5. Eigenvalue analysis of the bridge-wind system

For the equations of motion of the 2DOF system in the state-space using the state variables,

$$\mathbf{Y} = \begin{bmatrix} \mathbf{x} \\ \dot{\mathbf{x}} \end{bmatrix}, \tag{2.85}$$

it follows from Eq. (1.76),

$$\begin{bmatrix} \dot{\mathbf{x}} \\ \ddot{\mathbf{x}} \end{bmatrix} = \begin{bmatrix} 0 & \mathbf{I} \\ -\mathbf{K}^{\mathrm{e}} & -\mathbf{C}^{\mathrm{e}} \end{bmatrix} \begin{bmatrix} \mathbf{x} \\ \dot{\mathbf{x}} \end{bmatrix}. \tag{2.86}$$

State matrix A is by definition of the state-space matrix equal to,

$$\mathbf{A} = \begin{bmatrix} 0 & \mathbf{I} \\ -\mathbf{K}^{\mathrm{e}} & -\mathbf{C}^{\mathrm{e}} \end{bmatrix}. \tag{2.87}$$

The eigenvalues of the A matrix are complex numbers. The real part of the eigenvalues is the net damping of the coupled system in the heave and pitch motions $-\xi_h\omega_h$ and $-\xi_\alpha\omega_\alpha$, while the imaginary parts of the eigenvalues are net frequencies of the coupled system $\sqrt{1-\xi_h}\omega_h$ and $\sqrt{1-\xi_\alpha}\omega_\alpha$, respectively.

Through the iterative eigenvalue analysis of the state matrix A, the critical flow velocity for a coupled 2DOF system was determined. In case the frequencies from eigen solution of A

were equal to the input frequencies, and the damping from the eigen solution of A was zero, the critical flutter state was achieved.

Chapter 3

Experimental setup

Experimental setup for wind-tunnel measurements. Climatic boundary-layer wind tunnel of the Institute of Theoretical and Applied Mechanics in Prague, Czech Republic. Studied bridge-deck sections: (a) Great Belt Bridge, (b) Kao-Pin Hsi Bridge, (c) Golden Gate Bridge. Experimental stand that can separately measure the aerodynamic lift and drag forces and the pitch moment. Dynamic experimental stand that allows for a motion of the bridge-deck section model in the vertical and torsional directions and determination of flutter derivatives. Application of the Prandtl-Pitot tube for the measurement of the undisturbed, freestream airflow velocity. 2D Particle Image Velocimetry (PIV) technique to determine flow and vorticity fields around bridge-deck section models.

3.1. Wind tunnel

Experiments were carried out in the climatic boundary-layer wind-tunnel of the Institute of Theoretical and Applied Mechanics (ITAM) in Prague, Czech Republic. Wind tunnel is designed as a Göttingen closed-circuit type with controlled flow and temperature conditions. It consists of an inlet section, aerodynamic section, climatic section, and a fan section, Figure 10.

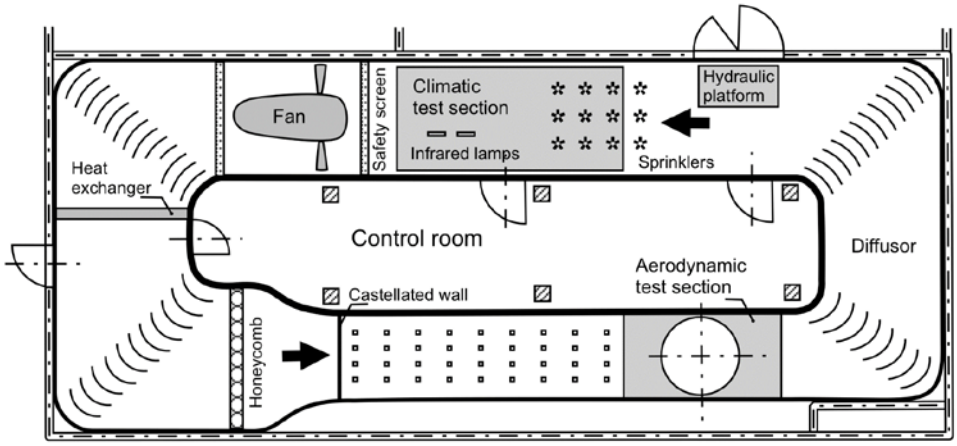

Figure 10: Schematic view of the Vincenc Strouhal wind tunnel of the Institute of Theoretical and Applied Mechanics (ITAM) in Prague, Czech Republic

This wind-tunnel is designed for experiments with respect to wind effects on structures, aeroelastic structural response, atmospheric boundary layer modeling, and general civil, environmental and mechanical engineering applications. The aerodynamic section of this wind tunnel is 1.9 m wide and 1.8 m high rectangular cross-section with a possibility to regulate flow velocity from 0.5 m/s to 35 m/s. Airflow in the test section is generated by the axial fan with 2 m in diameter that is powered by 200 kW electric motor. The flow is uniform along the wind-tunnel aerodynamic cross section and the turbulence intensity is less than 2%, Plut (2013). In this wind tunnel, it is possible to model the atmospheric boundary layer (ABL); however, this feature was not employed for the present thesis because the vertical dimension of the bridge-deck sections is negligible in comparison with the ABL height, i.e. it can be assumed that the freestream flow conditions are nearly the same upstream of the top and bottom surfaces of the bridge-deck sections. Bridge-deck section models were placed above the boundary layer at the wind-tunnel floor. The majority of experiments was carried out in the smooth flow, while additional experiments were

conducted using the grid to enhance the turbulence upstream of the bridge-deck section models.

3.2. Bridge-deck section and wind-barrier models

Studied bridge-deck sections are: (a) Great Belt Bridge (GBB) with a streamlined cross section, e.g. Bruno and Mancini (2002), (b) Kao-Pin Hsi Bridge (KPHB) with a semi-bluff cross section, e.g. Pospíšil et al. (2017), (c) Golden Gate Bridge (GGB) with a bluff cross section, e.g. Scanlan (1997). Geometrical details of the studied bridge cross-sections along with photos of the bridge-deck section models with windward wind barriers in place are presented in Figure 11.

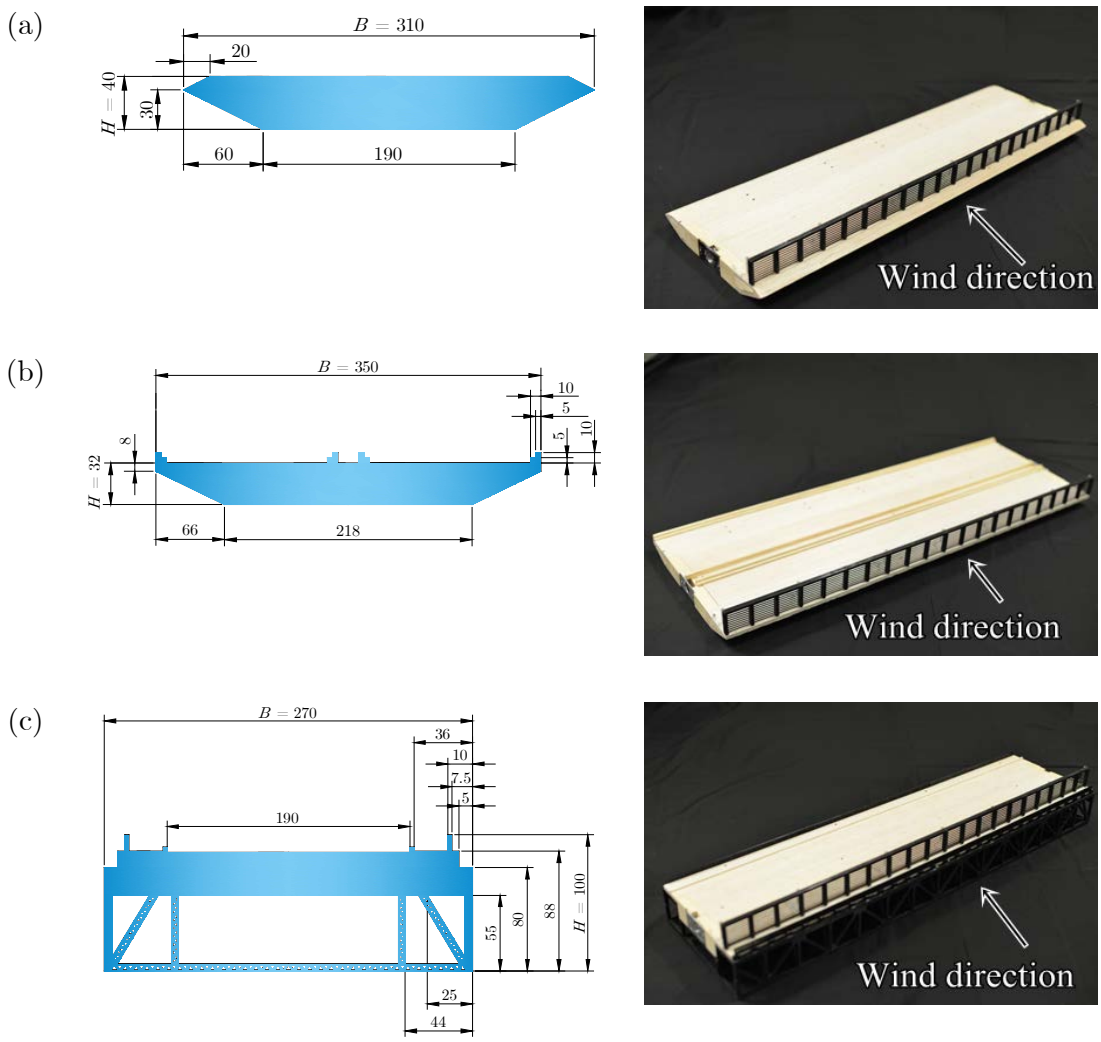

Figure 11: Geometrical details of the studied bridge-deck section models: (a) Great Belt Bridge, (b) Kao-Pin Hsi Bridge, (c) Golden Gate Bridge. All dimensions are in mm provided in model scale.

Wind-tunnel structural models were manufactured at the 1:100 length scale. The length of the models is $L = 1000$ mm laterally to the main flow direction (across the wind-tunnel test section). The ratio between the width of the bridge-deck section models (measured in the main flow direction) and span (laterally to the main flow direction) is smaller than 1:3. The bridge-deck section models were manufactured from balsa wood, while additional plastic parts were implemented on the GGB model, such as pedestrian railings and stiffness structure under the bridge-deck section.

The porous wind-barrier models were designed in the same 1:100 geometrical scale as for the bridge-deck section models. The wind-barrier design is similar to the one used in Kozmar et al. (2012a). The wind-barrier models consist of triangular profiles horizontally placed between vertical pillars that support the wind-barrier model. The distance between two neighboring pillar models is 45 mm. The wind-barrier porosity is calculated as a ratio between the area corresponding to the wind-barrier gaps and the entire frontal area of the wind barrier. There are some studies on the downscaling procedure when testing porous structural elements in the wind tunnel, e.g. Allori et al. (2013), which emphasize the importance of maintaining the same porosity for the scaled model, as it is for the prototype, while the shape and arrangement of the gaps are not that important. Nevertheless, in the present thesis, the focus is on dynamic stability of cable-supported bridges with porous wind barriers, which is believed not to be that influenced by the switching of the flow between various local flow regimes when the air passes through the gaps.

The wind-barrier porosity is generally a compromise between two contradictory demands: (i) wind conditions at bridge decks should be acceptable from the safety of vehicles point of view, (ii) wind barriers must not dramatically alter dynamic stability and aerodynamic loading of bridges. In practice, wind barriers are manufactured with various porosities. To investigate the effects of a wide range of those porous wind barriers on bridges, in the present study the 5 m high very-porous (50%), average-porous (30%) and solid (0%) wind barriers were considered. Furthermore, wind characteristics at bridge decks are influenced by the wind-barrier height. The 5 m high wind barrier effectively shelters vehicles and trucks on viaducts and bridges for the wind perpendicular to the wind barrier, Kozmar et al. (2012a). In case the wind incidence angle α is different from zero (upslope or downslope wind), e.g. downslope bora wind, Kozmar et al. (2012b), Kozmar et al. (2015), the wind-barrier height needs to be accordingly adapted, Figure 12.

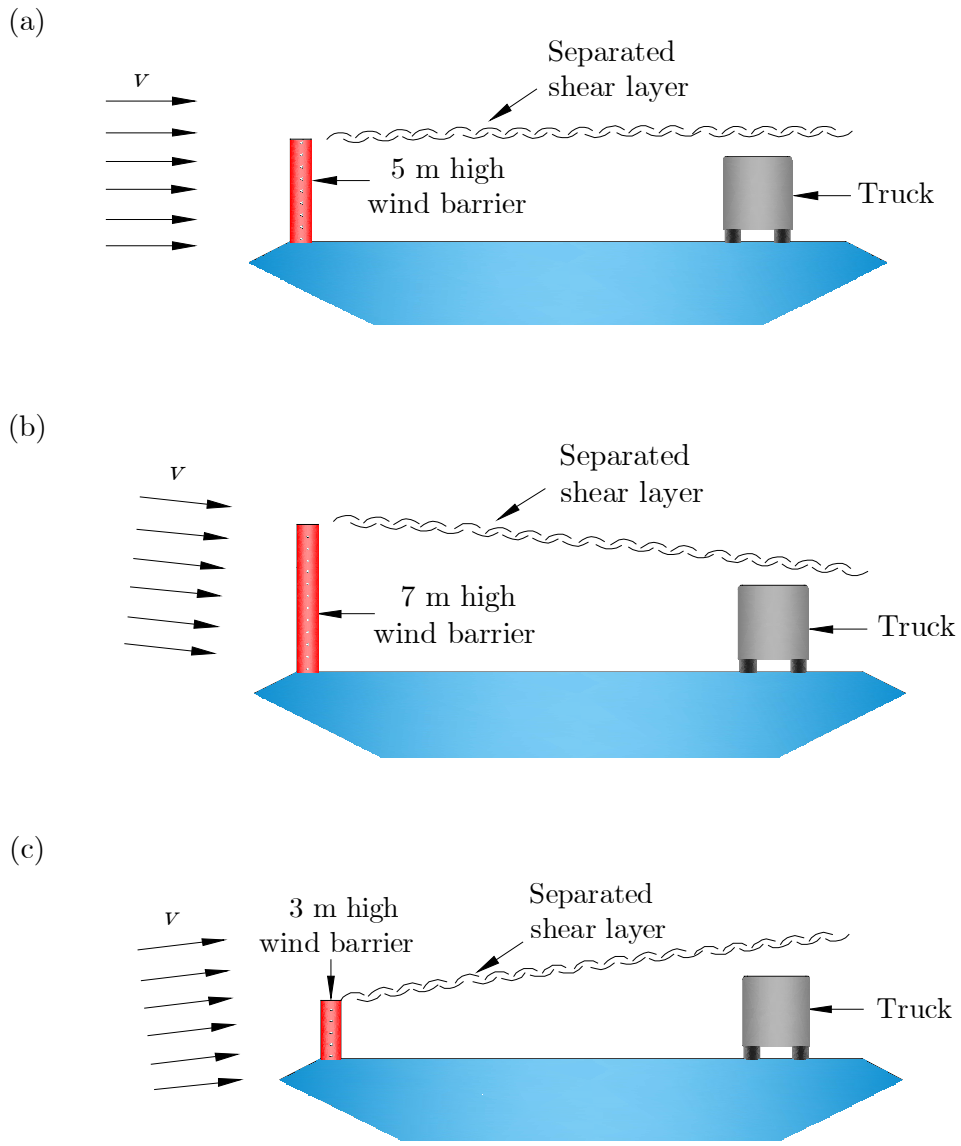

Figure 12: Wind-barrier sheltering of trucks for various wind incidence angles.

For the upslope wind, the wind barrier may be smaller than the standard height, while it needs to be larger than standard height for downslope wind conditions in order to provide the same sheltering efficiency for vehicles in all traffic lanes.

In the present study, the average-porous (30%) wind barrier of 3 m, 5 m, and 7 m full-scale height was considered. The notation of all investigated wind barriers is provided in Table 1.

Table 1 General characteristics of studied wind barriers

Notation	Height (model-scale)	Porosity
WB 5_30	50 mm	30%
WB 5_50	50 mm	50%
WB 5_0	50 mm	0%
WB 3_30	30 mm	30%
WB 7_30	70 mm	30%

Geometrical details and dimensions of the studied wind-barrier models are presented in Figure 13. The mass and mass moment of inertia of the investigated bridge-deck section models were not scaled in accordance with their prototypes. This discrepancy in scaling previously proved not to affect the results when using the spring-supported experimental model, Gu et al. (2001), which experimental approach was used in the present thesis as well.

The blockage of the bridge-deck section models placed on the experimental stands in the wind-tunnel test section was less than 7%. This was calculated as a ratio between the frontal area of the model together with the experimental stand, and the wind-tunnel cross section normally to the main flow direction. Hence, no correction factors were applied on the obtained results in agreement with West and Apelt (1982), Simiu and Scanlan (1996).

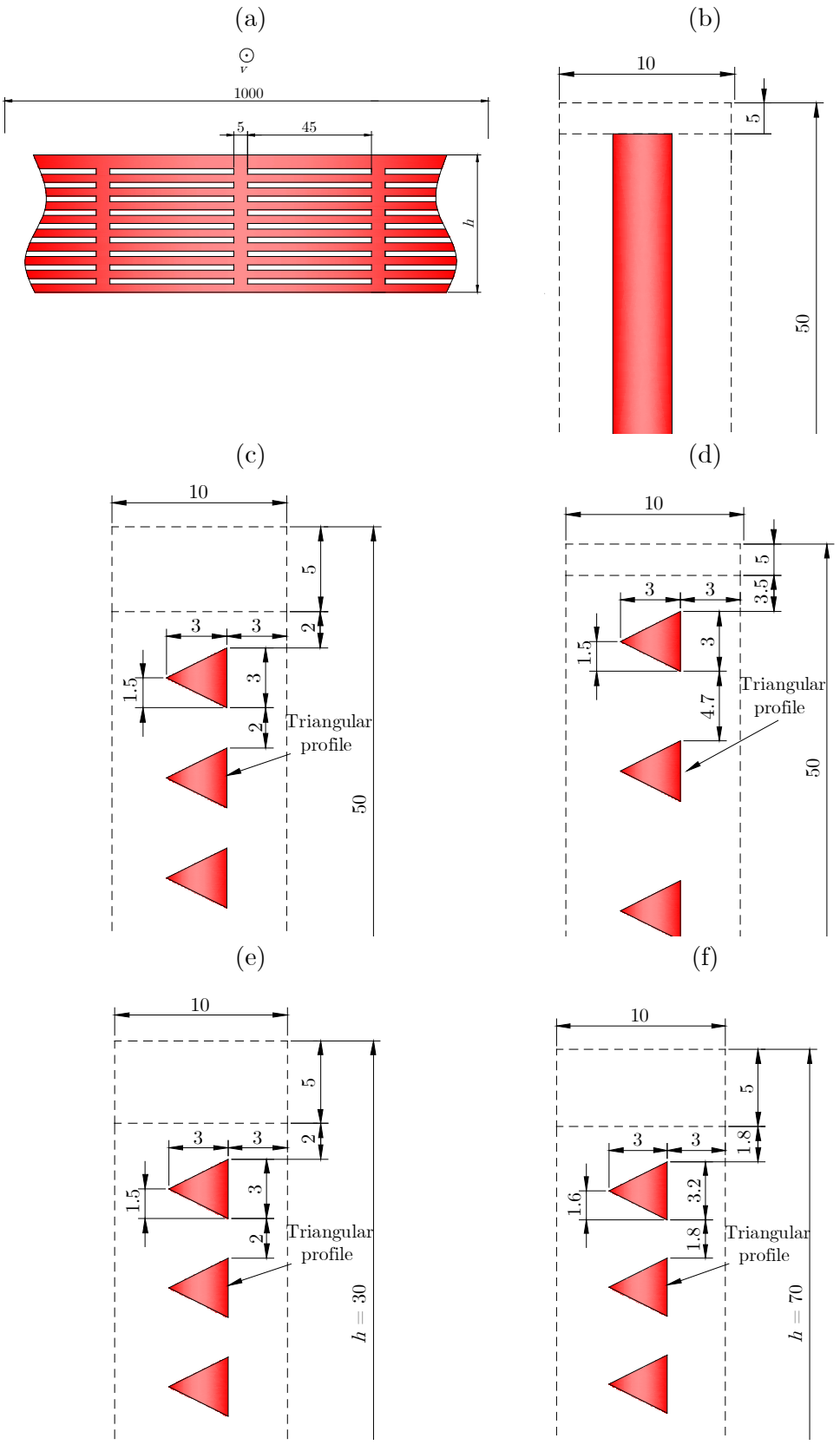

Figure 13: Geometrical details of the studied wind-barrier models: (a) front view, (b) WB 5_50, (c) WB 5_30, (d) WB 5_00, (e) WB 3_30, (f) WB 7_30. All dimensions in mm are provided in model scale, flow direction is from left to right.

3.3. Flow measurements

Flow characterization was performed using the 2D Particle Image Velocimetry (PIV) technique. This technique is an optical method used to determine flow characteristics around an investigated model, e.g. Adrian (1991), Willert and Gharib (1991). In the experiments, the air in the wind tunnel is seeded with tracing particles with similar buoyancy as the air; hence, the particles are transported together with the flow. The laser illuminates the sheet of airflow around the studied model. The high-speed camera captures the series of dual picture shots, while an appropriate software is used to calculate the movement of illuminated particles, i.e. fluid movement. The schematic view of the PIV experimental setup is shown in Figure 14.

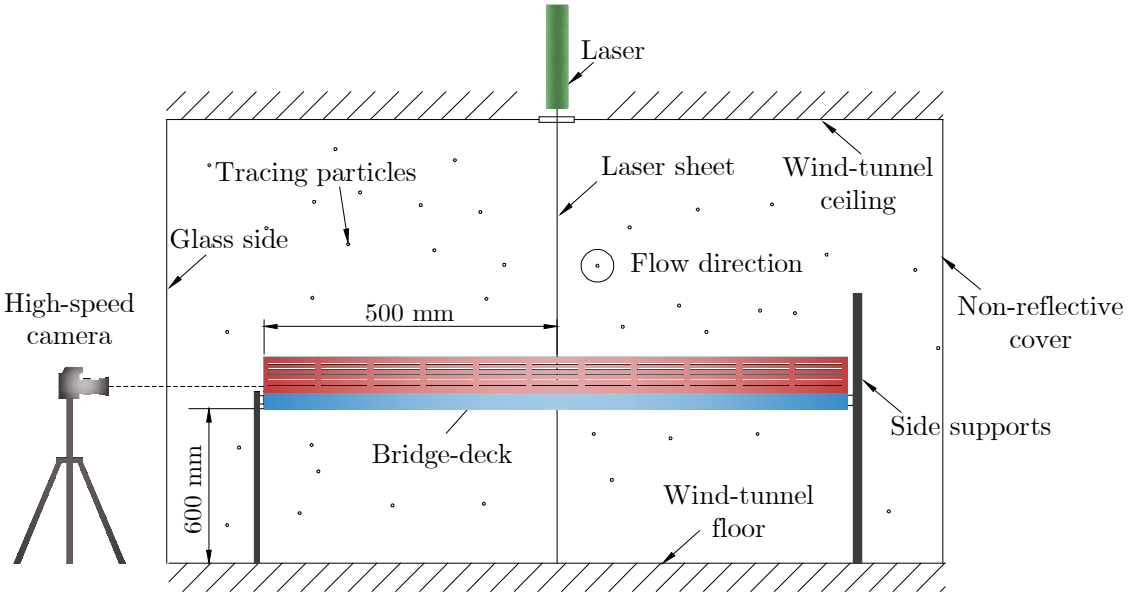

Figure 14: Experimental setup for flow characterization using the PIV technique.

In the present study, PIV equipment from Dantec and Litron Lasers was used. Dantec HiSence 4M camera was used to capture snapshots of the flow field. Its resolution was 2048 x 2048 pixels. The flow was illuminated using pulsed Nd: YAG laser. The seeding particle generator was placed in the climatic test section upstream of the fan and the honeycombs. The seeding particle generator was activated for a few seconds and then turned off.

The fog particles have diameter ≈1μm with high seeding density. After some time, the fog dispersed, thus resulting in a homogeneously seeded flow field, Figure 15. A series of 50 dual

picture shots was taken at a rate of 10 Hz. The time period between each pair of images was 400 μs. Fog generator vaporized special fog agent.

The adaptive correlation technique was selected to obtain the local flow velocity in the interrogation area with a size of 64 pixels. The resulting vector field was smoothed using a moving average filter. Smaller interrogation areas were tested as well but discarded due to high signal noise.

Figure 15: Seeding particles around the bridge-deck section model illuminated by laser.

The presented results represent average values of all the obtained frames. Measurements were conducted for the undisturbed freestream flow velocity approximately equal to 5 m/s, turbulence intensity less than 2% and the uniform flow velocity profile. The Reynolds number of the flow was approximately 10^5.

Separate shots were obtained with camera placed in line with the windward and leeward wind barrier models, respectively, to allow for a detailed analysis of flow characteristics immediately upstream and downstream of both wind barrier models. The same camera positioning was applied for measurements bellow the bottom surface of the bridge-deck section models. In those measurements, the bridge-deck section models were rotated around the horizontal axis parallel to the main flow direction.

In this way, four different images were captured for each configuration of the bridge-deck section and wind-barrier models, while those four images were subsequently merged into one

figure during post-processing. The experimental setup for the PIV measurements is presented in Figure 16.

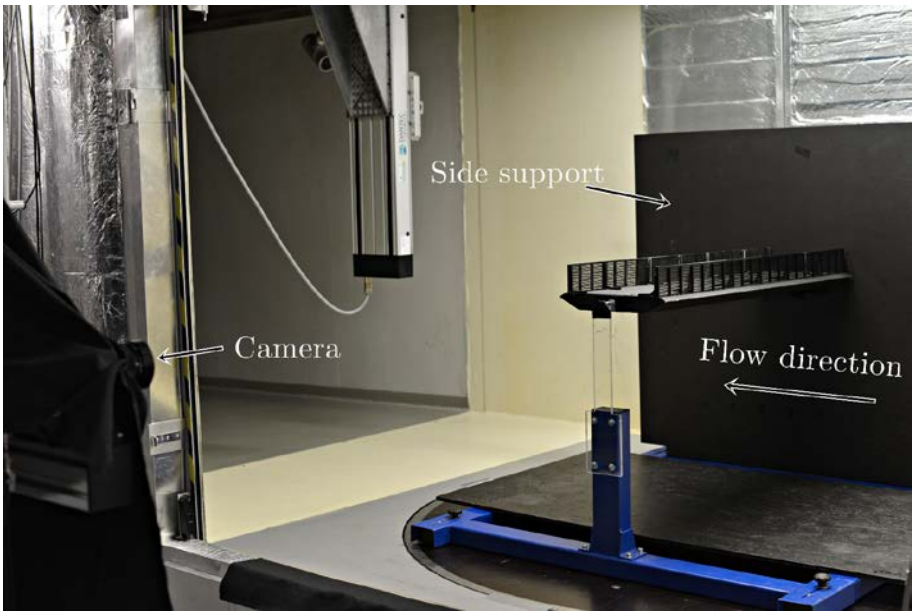

Figure 16: Experimental setup for the flow characterization measurements.

3.4. Aerodynamic force and moment measurements

Aerodynamic lift and drag forces as well as the pitch moment were measured for the steady bridge-deck section models, i.e. without their movement. The aerodynamic forces and the pitch moment are important for the structural stability of bridge decks; they can be used to predict across-wind galloping dynamic instability, e.g. Xu (2013). The mean aerodynamic lift and drag force coefficients of bridge-deck section models were used to calculate susceptibility to across-wind galloping instability using the Glauert-Den Hartog criterion based on a quasi-steady approach, Hartog (1932).

To measure the aerodynamic force and moment coefficients on bridge-deck section models, an experimental stand able to separately measure aerodynamic lift and drag forces and the pitch moment, experienced by the body immersed in the flow, was developed in this thesis. A kinematic scheme of this mechanism with a bridge-deck section model in place is presented in Figure 17.

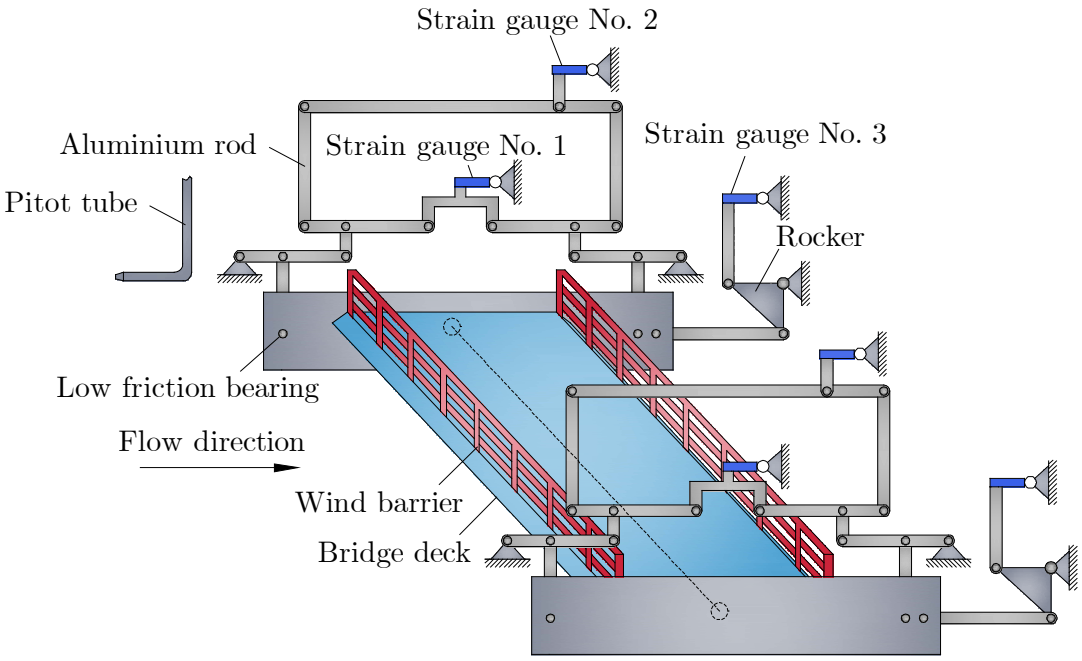

Figure 17: Kinematic scheme of the experimental mechanism for measurements of the aerodynamic drag and lift forces and the pitch moment.

Bridge-deck section models were attached to an aluminum plate and connected to an assembly of aluminum rods using low-friction bearings. Aerodynamic forces and moments were measured using strain gauges. Operative range of strain gauges is from 3 N to 100 N (Megatron KM102 model), while they are mechanically pre-stressed in order to be inside the operative range.

Strain gauge No. 1 measures the aerodynamic drag force, No. 2 measures the aerodynamic lift force, No. 3 measures the pitch moment of bridge-deck section models. The kinematics of the aluminum rods was designed in such a way that if e.g. only the lift force is applied on the model, strain gauges No. 2 are excited only. This is the case for the drag force and the pitch moment as well. The system proved to be linear, i.e. voltage measured on strain gauges is a linear function of force acting on the system. Strain gauges were connected through six galvanically isolated modules to the acquisition system via the AD board.

Calibration procedure included separately employing the lift force, drag force and pitch moment (one force, i.e. moment, is applied in one experiment) on the system using various dummies with known weight. The pulley-wire system with the measured friction coefficient of the pulley was used when applying the drag force only. Calibration results for strain gauges for the drag and lift forces and the pitch moment are shown in Figure 18.

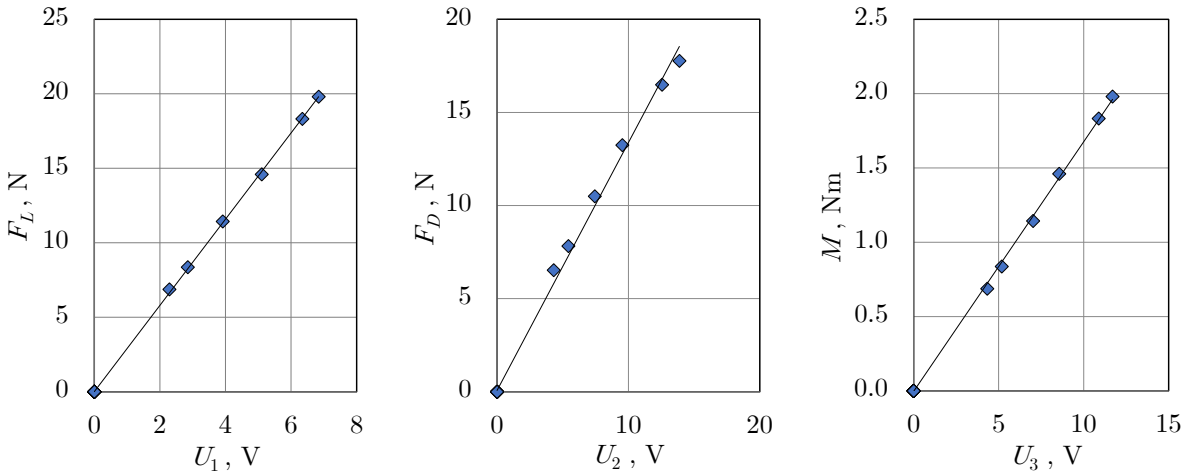

Figure 18: Calibration results for strain gauges for the drag and lift forces and the pitch moment.

The system proved to be linear in the range of obtained loads in the subsequent experiments (voltage on strain gauges is linear with respect to the acting force or moment).

The measurements of aerodynamic forces and the moment were carried out at the sampling rate of 1 kHz and the time acquisition length of 30 s. The aerodynamic force and moment coefficients in the preliminary experiments proved to be nearly constant for Reynolds numbers ($\mathrm{Re} = \rho v B/\mu$) larger than $2{\cdot}10^5$. Hence, freestream flow velocity in all experiments was selected to be approximately 12.5 m/s, thus resulting in Re approximately $3{\cdot}10^5$, which is larger than the critical value.

Plastic flat end-plates were placed between the mechanism and the bridge-deck section models to avoid flow disturbance at the lateral sides of the model (end effects), the influence of structural parts of the mechanism, and to provide two-dimensional flow around bridge-deck section models.

Prandtl-Pitot tube was used to measure undisturbed, freestream flow velocity. It was placed between the plastic plates and 0.5 m upstream of the leading edge of the bridge-deck section models. This device is used to determine the mean flow velocity via the difference between the total and the static pressure in the flow. While the Prandtl-Pitot tube is not suitable for measuring the velocity time history at high sampling rate, it has been commonly used to measure reference mean flow velocity, as it was the case in this thesis as well.

Experimental setup for measurements of the aerodynamic force and moment coefficients is shown in Figure 19. Dewetron data acquisition system was used for recording the

aerodynamic forces and the moment of the bridge-deck section models placed on the experimental stand. Dewetron system allows for recording of the signal by using the 24-bit A/D conversion with anti-aliasing filtering, post-processing and signal conditioning tools.

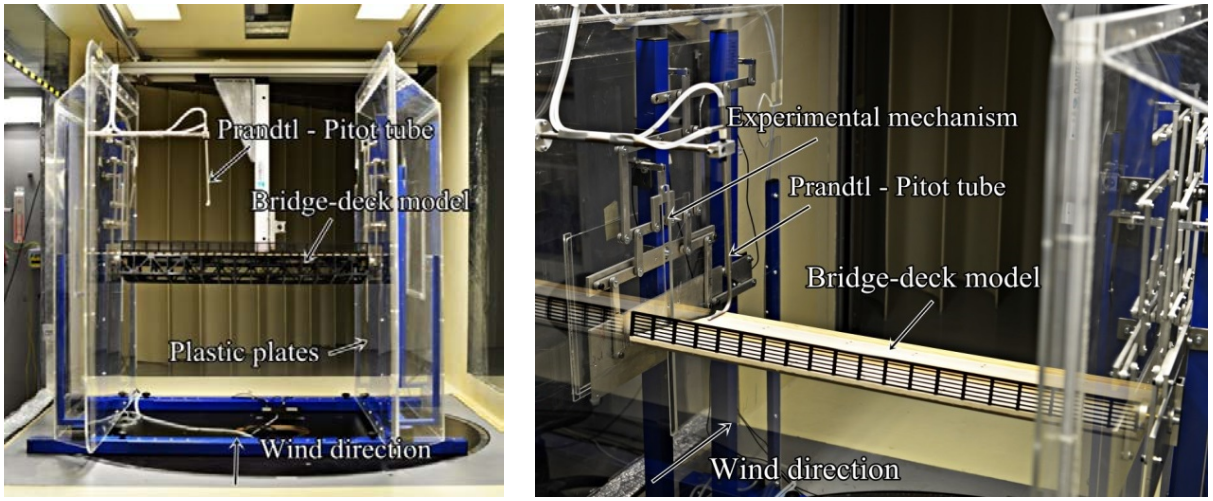

Figure 19: Experimental setup for measurements of the aerodynamic force and moment coefficients.

3.5. Aeroelastic dynamic measurements

For the aerodynamic stability analysis, the bridge-deck section models were attached to an original and multipurpose experimental stand. This stand was designed and constructed at ITAM for the measurements of linear and nonlinear aeroelastic phenomena, Král et al. (2016).

Unlike the traditional concept of mounting the bridge-deck section model using spring-supported body, this setup enables a quick and precise frequency tuning in the range of ω_h from 1 to 10 for vertical oscillations and the same range for torsional oscillations. This is due to a specific design based on torsional bar that provides stiffness in the vertical motion, and m-spring in the torsional degree of freedom. A schematic view of this mechanism along with its kinematical arrangement is presented in Figure 20.

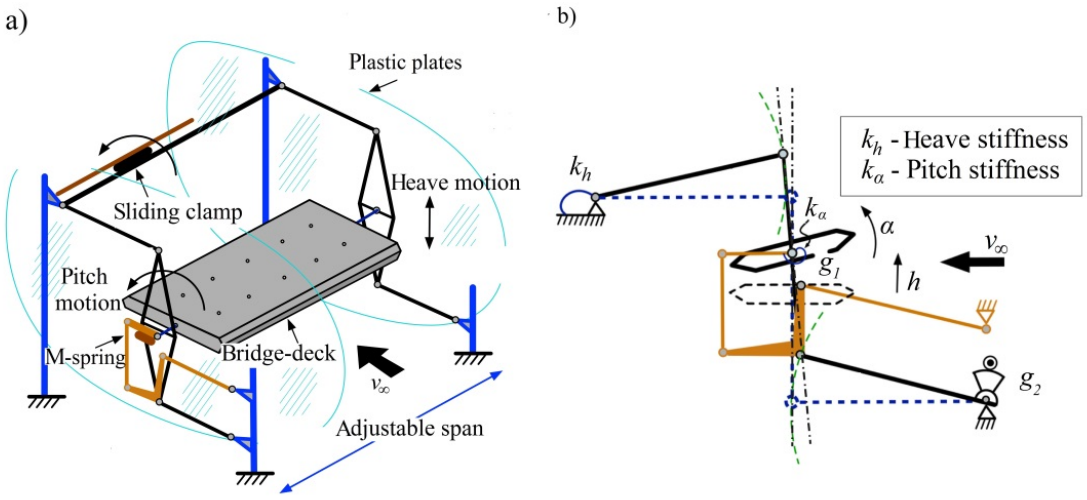

Figure 20: Kinematic scheme of the experimental stand for measurements of aeroelastic properties of bridge-deck section models, Král et al. (2016).

The motion of this mechanism is based on the Watt linkage principle. The heave motion of the model is mechanically independent of the pitch motion. A movement of a model centroid is rectilinear for large amplitudes of oscillations. A behavior of structural springs is linear until very large amplitudes of oscillation (larger than observed in the experiments) are achieved, both in the heave and pitch directions.

The framework of a movable part was designed to be as light as possible; therefore, the bars were made of carbon fiber composite and joined together using the aluminum elements. Experimental frame allows for mounting of bridge-deck section models with span ranging from 0.2 m to 1 m. The motions of a bridge-deck section model in the heave and pitch directions were measured using rotary magnetic transducers. The pitch displacement was measured directly in the g_1 position (Figure 20), while the heave displacement was acquired by the rotary transducer using a mechanical speed-increasing gear, i.e. g_2 position in Figure 20.

Plastic plates were installed on the experimental stand to allow for achieving the two-dimensional flow around the bridge-deck section models, while the flow velocity was measured using the Prandtl-Pitot tube placed between the plastic plates and 0.5 m upstream of the model. The experiments on the dynamic response of bridge-deck section models were carried out at the sampling rate of 1 kHz and the time acquisition length of 30 s.

Experimental setup for the bridge-deck section models including the wind-barrier model in the aerodynamic wind-tunnel test section is presented in Figure 21. Dewetron data

acquisition system was used for recording a dynamic response of the bridge-deck section models placed on the experimental stand.

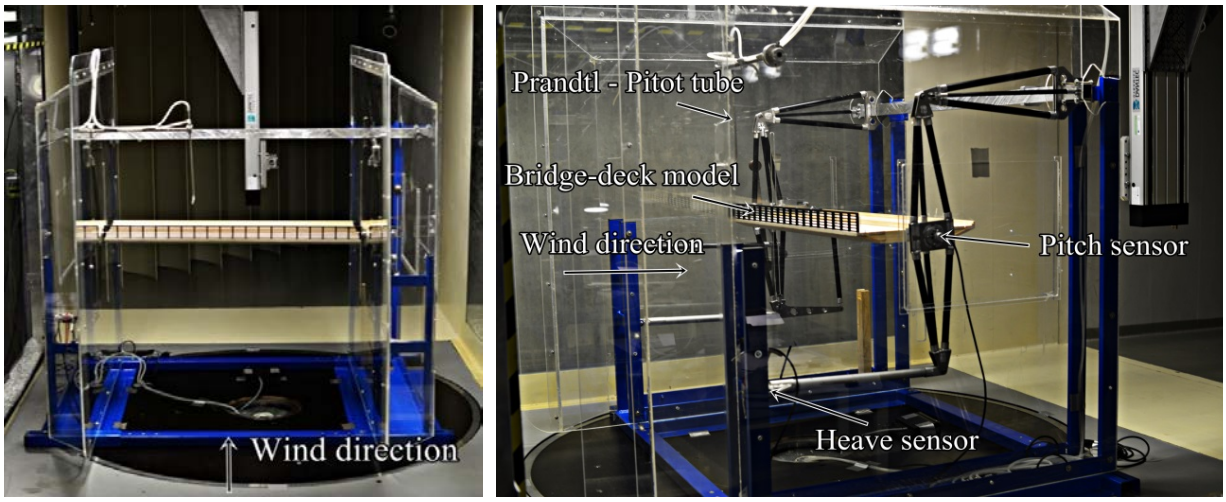

Figure 21: Experimental setup for the measurement of the dynamic response of bridge-deck section models.

The measurements were conducted using the free-vibration method, which includes an initial displacement of a bridge-deck section model in the vertical and torsional directions, and measurement of free-decayed oscillations due to the freestream flow velocities.

The adopted initial vertical and torsional displacements of the bridge-deck section models were constant during the experiments, as suggested in Mannini and Bartoli (2015), at $h_0 \approx 10$ mm and $\alpha_0 \approx 8°$, respectively. Excessively large initial displacements may influence the linear dependence of the self-excited forces on the motion of the bridge-deck section models, e.g. Diana et al. (2008), which is more pronounced for bluff bridge-deck section models, Mannini et al. (2016), as this may affect the reattachment point of the separated flow. Initial torsional displacement proved to be more important than the heave displacement for FDs, Noda et al. (2003).

In the present thesis, the values for the initial vertical and torsional displacements were set based on the preliminary tests because for most configurations the initial amplitudes decayed relatively quickly at small reduced flow velocities, and hence it was difficult to identify them in case the initial amplitudes were smaller, e.g. Poulsen et al. (1992).

The largest mean rotation of the model of 0.9° was recorded for the Golden Gate Bridge with the 5 m high (full-scale) wind barrier and 0% porosity. The nonlinear effect of the flow

incidence angle may accordingly be neglected, e.g. Diana et al. (2010). Free-decay oscillations were measured for various freestream flow velocities as well as for the system without the flow. The damping and stiffness matrix were accordingly obtained.

An example of the dynamic response of the bridge-deck section model is reported for two characteristic cases, (i) relatively small airflow velocity at which there is no significant coupling, while the oscillations gradually decay, (ii) in the proximity of the torsional flutter, where coupling of the heave and pitch motions may be observed, and the damping in the pitch motion is decreased, Figure 22.

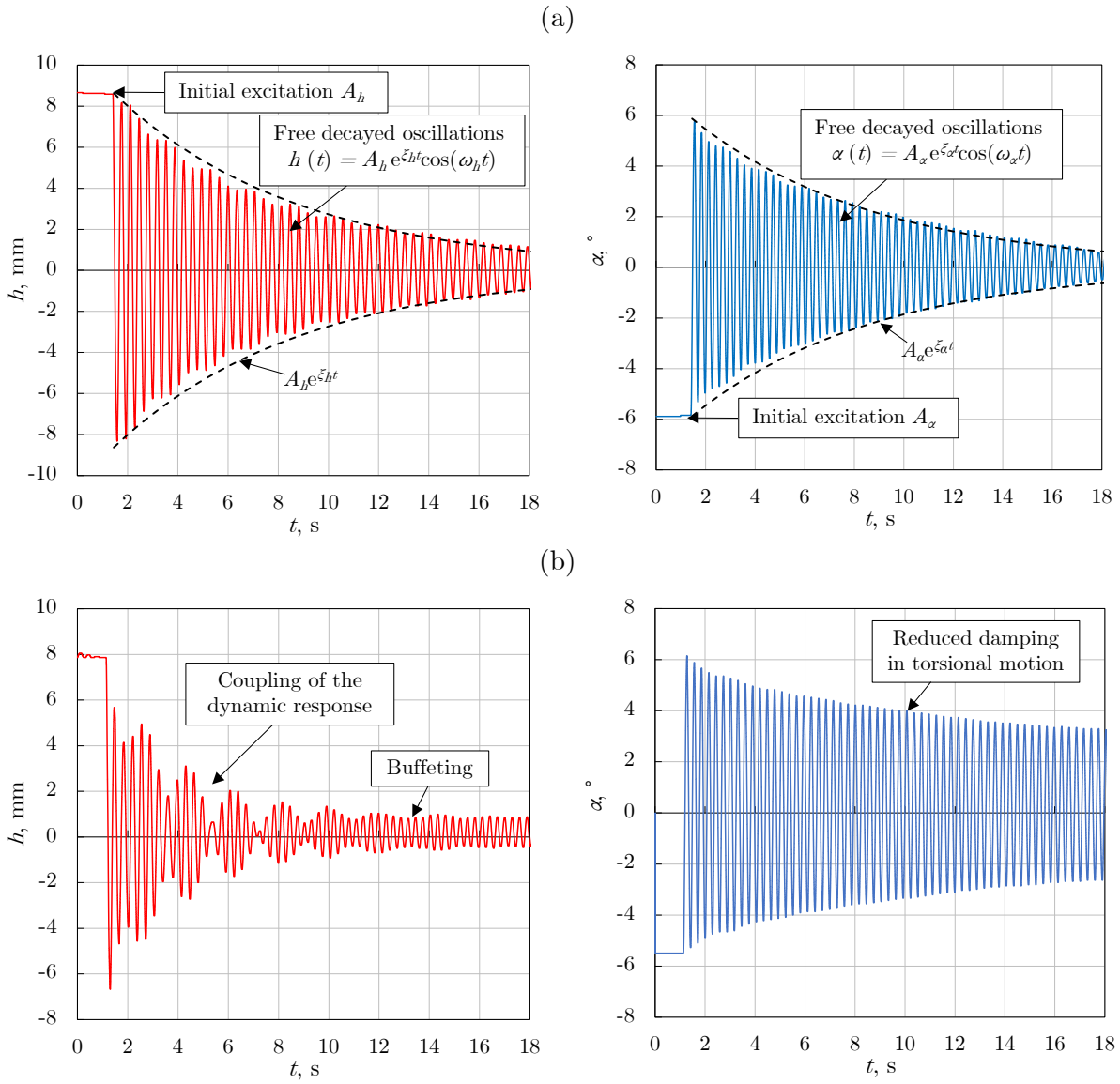

Figure 22: Examples of the dynamic response of the bridge-deck section model: (a) relatively small airflow velocity, (b) proximity of torsional flutter.

The free-vibration technique is less time consuming in comparison with the forced-vibration technique. In addition, the free-vibration technique implies a structural model characterized by a more natural interaction of the bridge-deck section model with the flow.

However, there are some drawbacks of the free-vibration technique as compared to the forced-vibration method. Buffeting forces due to turbulence enhance a stochastic component of the bridge-deck section model movement with increasing freestream flow velocity. This is particularly exhibited in case of dynamically stable bridge decks, while it can decrease the accuracy of the results in the range of larger freestream flow velocities.

Furthermore, large flow velocities may lead to the amplification of the net damping due to an increase of the aerodynamic damping if the studied bridge-deck section model is dynamically stable. Therefore, a short period of time was available to identify a dynamic response of bridge-deck section models.

The free-vibration method has limited applicability for velocities smaller than the critical flow velocity at which the bridge-deck section model starts to flutter, and this method is no longer accurate due to linear assumptions of the model. However, the analysis of the dynamic behavior is commonly focused on the pre-critical state.

Due to a complex geometry of the bridge-deck section models and the moving parts of the experimental stand, the mass parameters of the bodies engaged in the motion cannot be determined analytically and an experimental approach is required. The identification of the mass parameters was carried out through three steps. Experiments encompassed measurements of the free-decay oscillation (in the still air) of the stand itself, a dummy of known mass characteristics mounted on the stand, and finally of the bridge-deck section models mounted on the stand. Mass characteristics of the studied bridge-deck section models necessary for further analysis of the aeroelastic behavior were determined by using the equations,

$$m_{st} = m_{du}\left(\frac{\omega_{h,st}^{2}}{\omega_{h,du}^{2}} - 1\right);\ m_{dk} = m_{st}\left(\frac{\omega_{h,st}^{2}}{\omega_{h,dk}^{2}} - 1\right). \tag{3.1}$$

$$I_{st} = I_{du}\left(\frac{\omega_{\alpha,st}^{2}}{\omega_{\alpha,du}^{2}} - 1\right); \qquad I_{dk} = I_{st}\left(\frac{\omega_{\alpha,st}^{2}}{\omega_{\alpha,dk}^{2}} - 1\right). \tag{3.2}$$

The subscript *st* is for the experimental stand without the bridge-deck section model, *du* is for the experimental stand with the dummy body mounted, and *dk* for the experimental stand with the bridge-deck section model.

From the recorded dynamic response of the bridge-deck section models at various flow velocities (and still air), the free-decay damping and natural frequencies of oscillations in both degrees of freedom can be determined. This was obtained using the numerical method based on the least squares method. The mass characteristics and dynamic properties of the bridge-deck section models obtained in the quiescent air are provided in Table 2.

Table 2: Mass characteristics and dynamic properties of the studied bridge-deck section models.

Bridge	m, kg	I, kg m2	f_h, Hz	f_α, Hz	ξ_h, -	ξ_α, -
GBB	3.99 – 4.17	0.0206 – 0.0235	2.8-2.9	3.2-3.3	0.007-0.009	0.008-0.01
KPHB	4.11 – 4.29	0.0248-0.0287	2.8-2.9	3.3-3.4	0.007-0.008	0.008-0.009
GGB	5.23-5.41	0.0305-0.0334	2.8	3.3-3.5	0.005-0.007	0.009-0.017

The mass and inertia of the bridge-deck section models depend on the arrangement, height and porosity of wind-barrier models, system stiffness depends on the frequency tuning, while the mechanical damping depends on the mechanical friction of the system.

The results include the generalized damping and stiffness matrices obtained at various freestream flow velocities. These matrices together with the structural damping and stiffness matrices obtained in the still air can be used for determination of FDs at various freestream flow velocities. FDs obtained from the 2DOF dynamic response of bridge-deck section models are commonly reported as a function of the reduced flow velocity $v_\infty/(f_{\alpha/h} \cdot B)$, where v_∞ is undisturbed freestream wind velocity, f is frequency of oscillation in the heave or pitch directions, B is width of the bridge-deck section models. FDs associated with the heave motion were normalized with respect to the heave natural frequency of oscillation (H_1^*, H_4^*, A_1^*, A_4^*), while the FDs associated with the pitch motion were normalized with respect to the pitch natural frequency of oscillation, (H_2^*, H_3^*, A_2^*, A_3^*).

In addition to the experiments carried out in the smooth flow with the turbulence intensity less than 2%, the influence of turbulence on the dynamic stability of bridge-deck section models including the wind-barrier models was assessed. The turbulence grid that enhances turbulence was placed upstream of the bridge-deck section models at two different positions, Figure 23: (a) 6.8 m upstream of the model, i.e. low-turbulence case (LT), (b) 1.5 m upstream of the model, i.e. high-turbulence case (HT).

(a) Grid setup for low turbulence

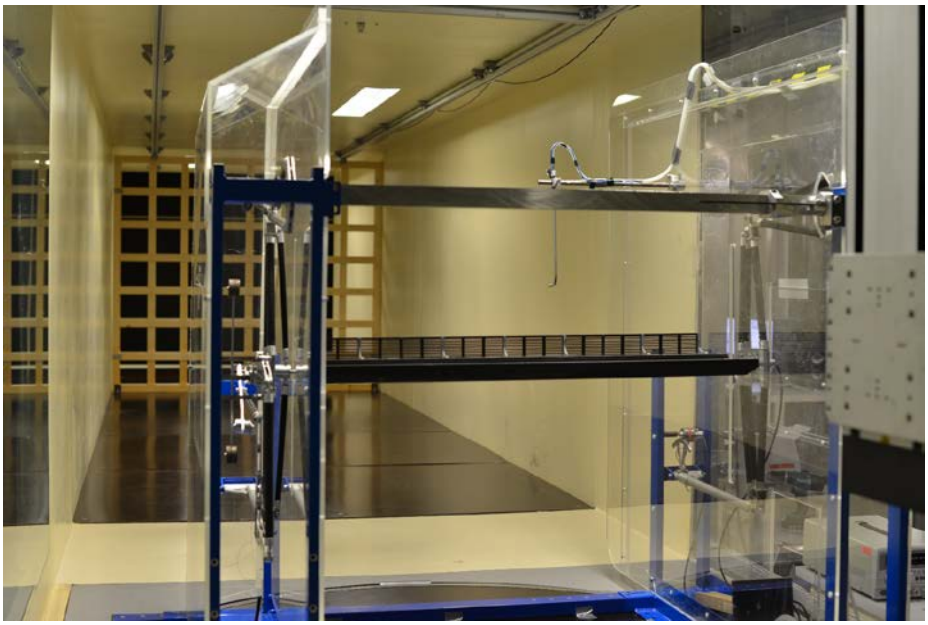

(b) Grid setup for high turbulence

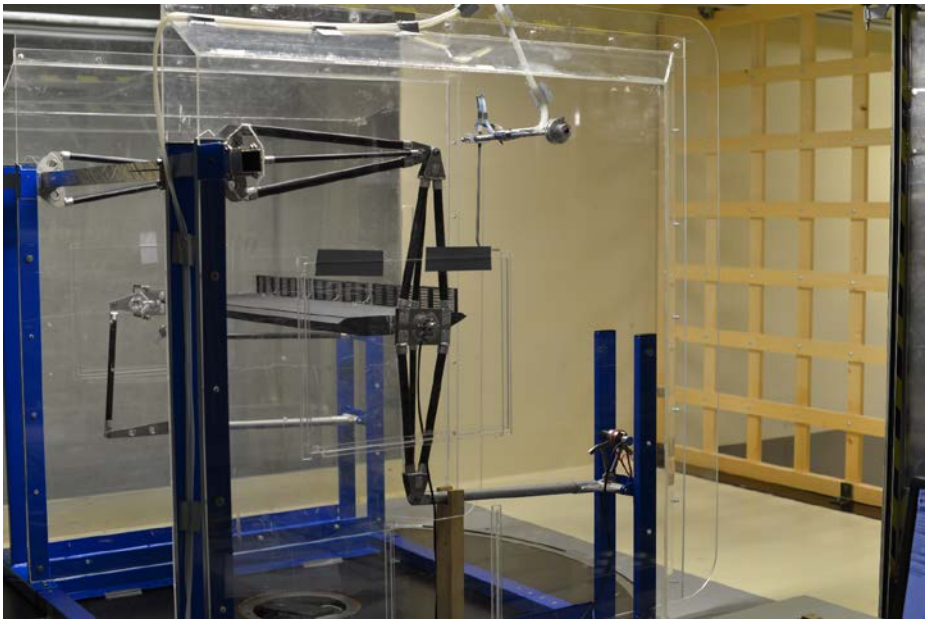

Figure 23: Turbulence grid placed upstream of the bridge-deck section model: (a) low turbulence, (b) high turbulence.

The turbulence intensity is defined as,

$$I = \frac{\sqrt{v'^2}}{\overline{V}}, \tag{3.3}$$

where I is turbulence intensity, v' is airflow velocity fluctuation, $\overline{V}$ is mean flow velocity. The turbulence intensity was determined based of hot-wire measurements in the mid height of the wind-tunnel aerodynamic section. A development of the turbulence intensity I_{vx} along the test section (x-direction) is reported in Figure 24, whereas x_g is the distance between the grid and the measuring position.

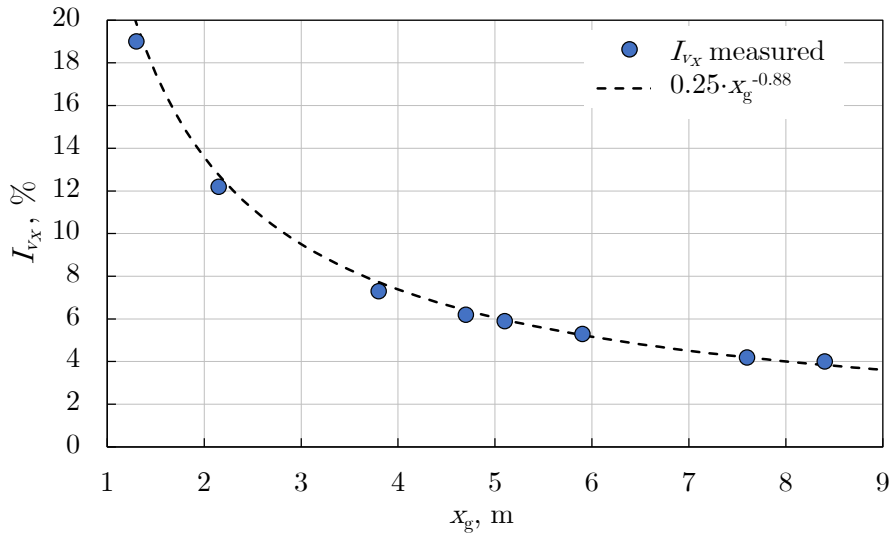

Figure 24: Development of the turbulence intensity along the test section (x-direction).

The obtained turbulence intensity for the subsequent measurements of the bridge-deck dynamic stability are 17.5% for HT and 4.5% for LT at the position of the bridge-deck section model.

Chapter 4

Experimental results and discussion

2D mean flow velocity fields and the variance of the flow velocity fields. Aerodynamic drag force, lift force and the pitch moment acting on the bridge-deck section models for various flow incidence angles. Galloping dynamic instability of the bridge-deck section models equipped with wind-barrier models. Aeroelastic flutter derivatives. Eigenvalue analysis of the bridge-wind dynamic system to determine the critical flow velocity for flutter instability.

4.1. Flow characteristics around bridge-deck section models

The results include the 2D mean flow velocity fields normalized using the undisturbed, freestream flow velocity and the variance (standard deviation squared) of the flow velocity. Standard deviation of the airflow velocity s_v is defined as,

$$s_v = \sqrt{\frac{\sum_{i=1}^{N}(v_i - v)^2}{N-1}}, \tag{4.1}$$

where v_i is sample of the flow velocity data, v is mean airflow velocity, N is number of data points. The freestream flow velocity was constant in all experiments at approximately 5 m/s; hence, the variance of the flow velocity can actually serve as a measure for turbulence intensity of the flow. The results are reported here for the Great Belt Bridge because the influence of wind barriers on flow characteristics are most pronounced for this particular bridge-deck section.

4.1.1. Mean velocity field around bridge-deck sections

2D mean flow velocity fields are presented in Figure 25 for the Great Belt Bridge with windward wind barriers of various heights and porosities, while the mean flow velocity fields for various arrangements of wind barriers are reported in Figure 27.

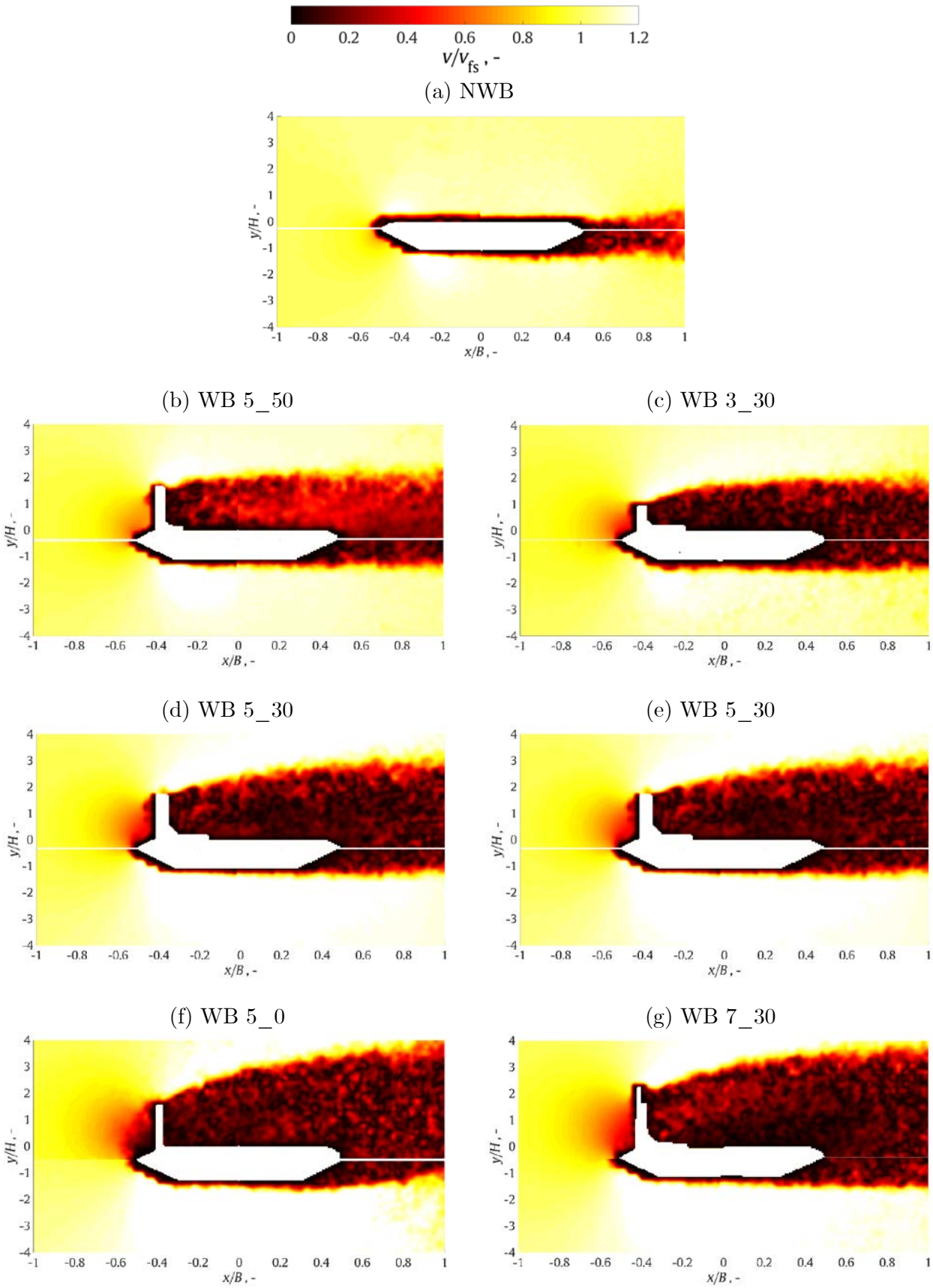

(a) NWB

(b) WB 5_50

(c) WB 3_30

(d) WB 5_30

(e) WB 5_30

(f) WB 5_0

(g) WB 7_30

Figure 25: Mean flow velocity field around the Great Belt Bridge deck section for various heights and porosities of the windward wind barrier. Flow direction is from left to right.

Mean flow velocities are significantly reduced downstream of wind barriers thus indicating its sheltering effect in agreement with Coleman and Baker (1994), Kozmar et al. (2012a), Avila-Sanchez et al. (2016). The mean flow velocities are more reduced for the less porous, i.e. more solid, windward wind barrier because the largest flow velocities immediately above the bridge-deck section are observed for the largest porosity of the windward wind barrier.

The shear layer that separates from the top of the windward wind barrier divides the area of the reduced flow velocity under the separated shear layer from the area of the undisturbed freestream flow velocity above the shear layer. The slope of the shear layer is larger for more solid wind barriers, thus providing a more effective sheltering for vehicles. The height of the windward wind barrier determines the height of the sheltered area above the bridge-deck section, i.e. higher wind barriers yield an increased height of the reduced flow velocity area above the bridge-deck section, thus providing more favorable conditions for vehicles passing the bridge. The flow velocity profiles at $x/B = 0$ for various porosities and heights of the windward wind barrier are reported in Figure 26.

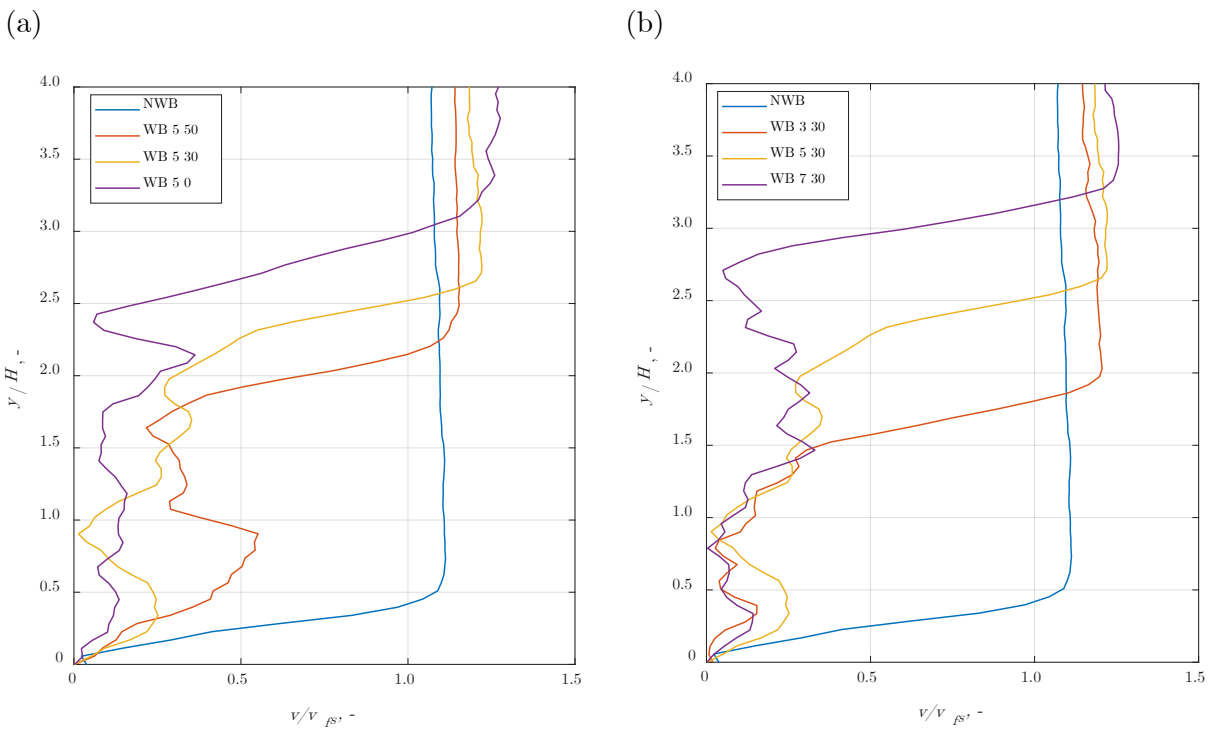

Figure 26: Flow velocity profiles at $x/B = 0$ for various (a) porosities and (b) heights of the windward wind barrier.

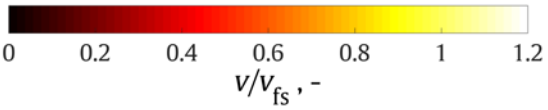

(a) WB 3_30 WW

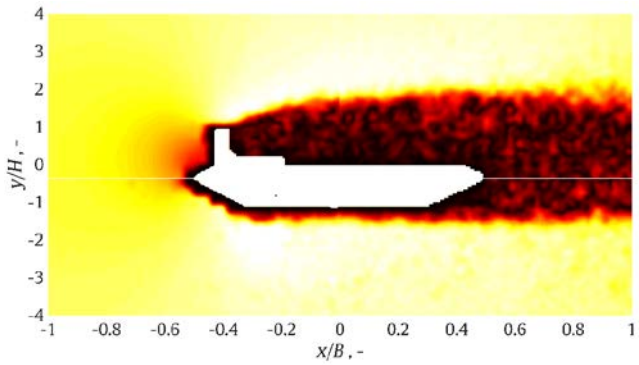

(b) WB 3_30 LW

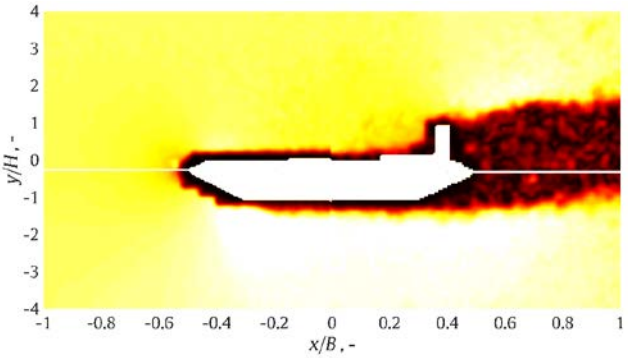

(c) WB 3_30 WW+LW

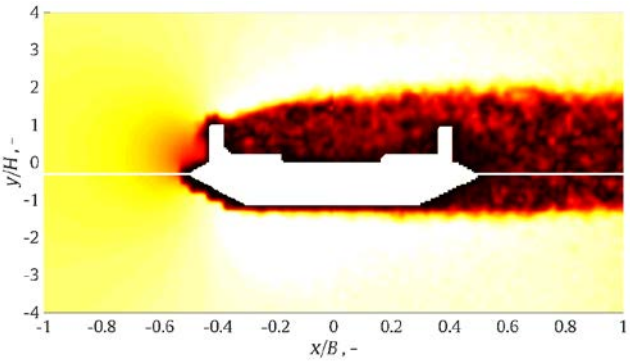

(d) WB 5_30 WW

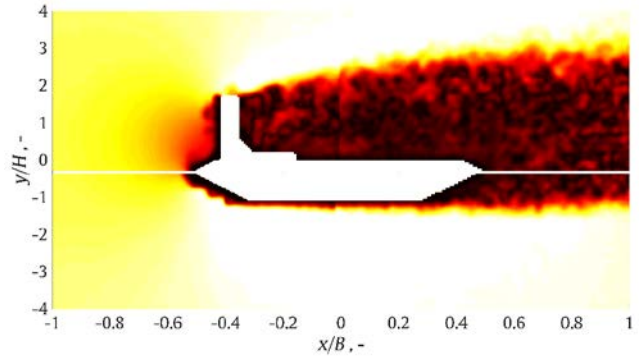

(e) WB 5_30 LW

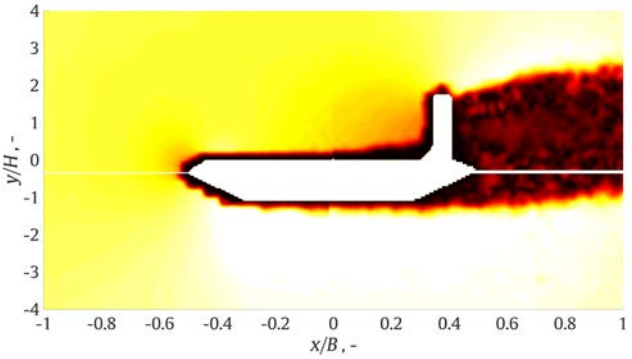

(f) WB 5_30 WW+LW

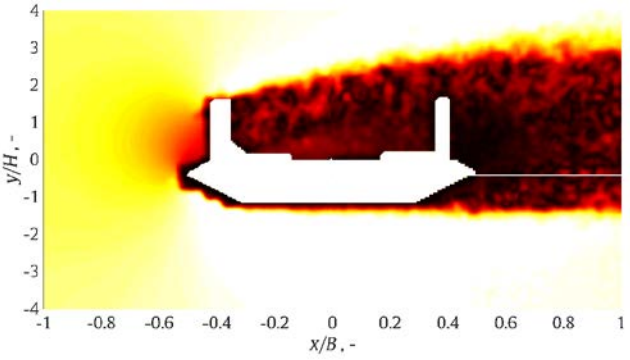

(g) WB 7_30 WW (h) WB 7_30 LW

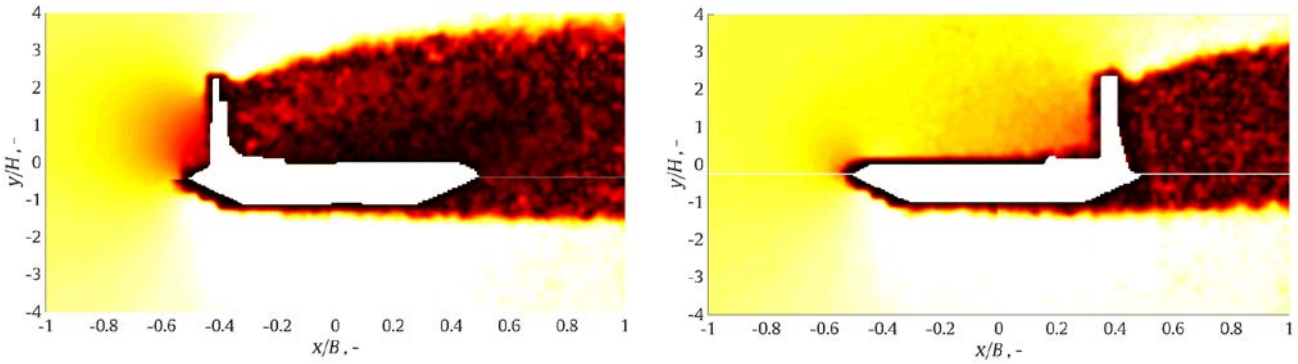

(i) WB 7_30 WW+LW

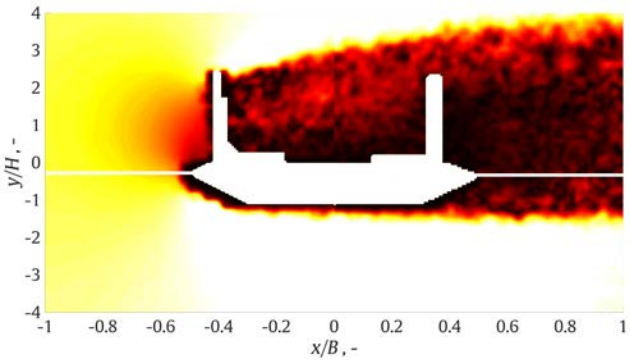

Figure 27: Mean flow velocity field around the Great Belt Bridge deck section for various arrangements of wind barriers. Flow direction is from left to right.

The windward and both windward and leeward wind barriers yield relatively similar mean flow velocity fields, whereas the leeward wind barrier provides practically no sheltering for vehicles, as the mean flow velocities above the bridge-deck section are relatively large and very close above the bridge-deck section they reach the freestream undisturbed velocities. The shear layer separating from the top of the wind barriers is observed for all wind barriers. There is a trend of larger mean flow velocities above the bridge-deck section when both wind barriers are in place in comparison with the windward wind barrier only, which is due to the vortex that is captured between the two wind barriers, in agreement with Avila-Sanchez et al. (2016). The flow velocity profiles at $x/B = 0$ for various arrangements of the 5 m high (full-scale) and 50 % porous wind barrier are reported in Figure 28.

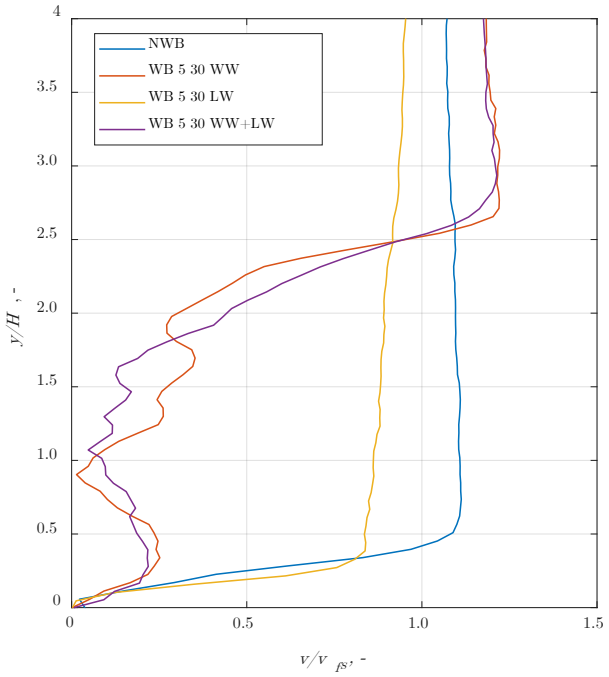

Figure 28: The flow velocity profiles at x/B = 0 for various arrangements of the 5 m high (full-scale) and 50 % porous wind barrier.

4.1.2. Vorticity field around bridge-deck sections

The fields of the flow velocity variance are presented in Figure 29 for the Great Belt Bridge with the windward wind-barrier of various heights and porosities, while the variance of the flow velocity fields for various arrangements of the wind barrier is reported in Figure 31.

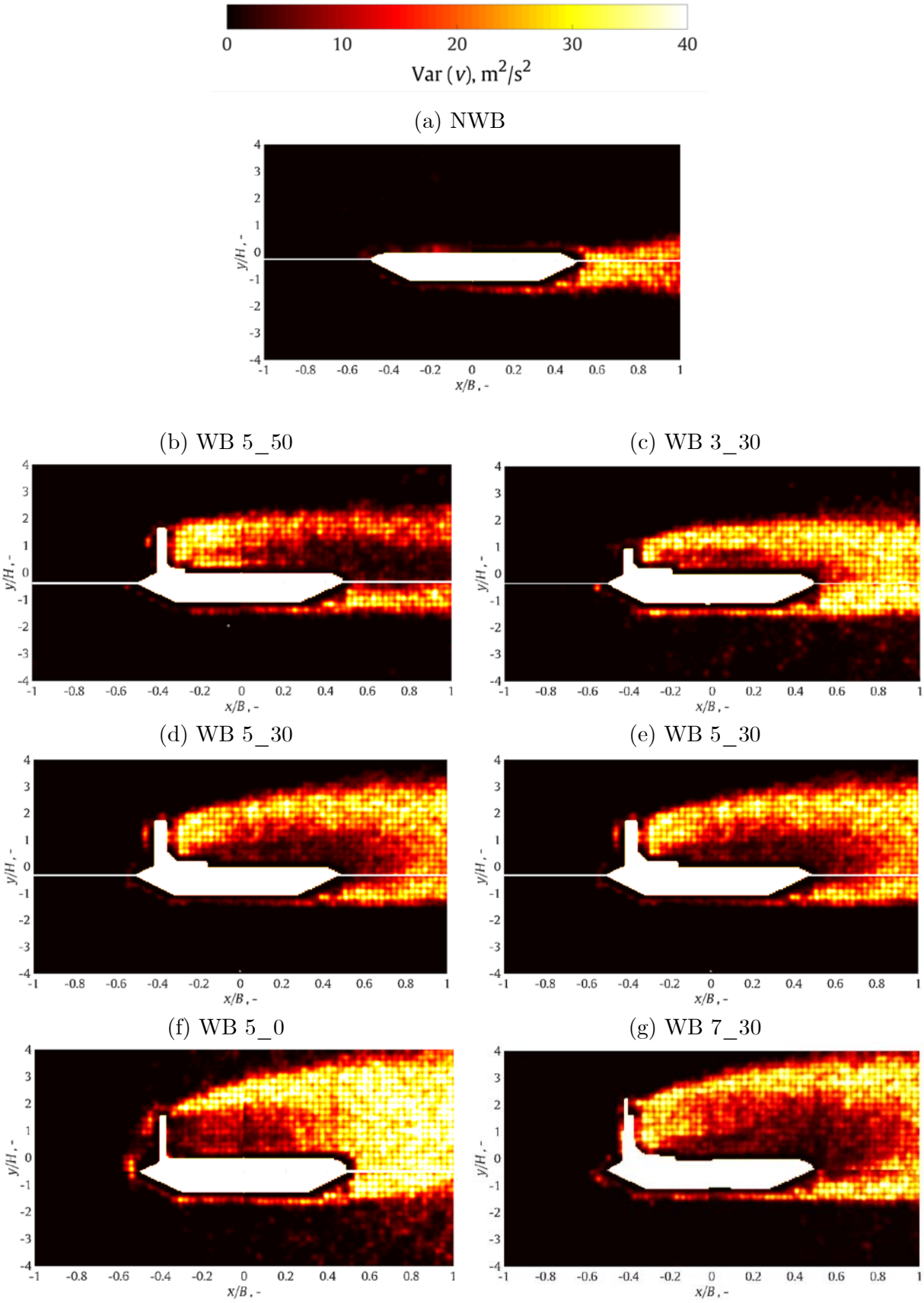

Figure 29: Flow velocity variance around the Great Belt Bridge deck section for various heights and porosities of the windward wind barrier. Flow direction is from left to right.

The flow velocity variance indicates large perturbations in the flow velocity due to wind barriers. Very large flow velocity variance (vorticity) is observed in the shear layer that separates from the tops of wind barriers and the top and bottom surfaces of the bridge-deck section. Similarly as for the mean velocity flow fields, the shear layer that separates from the top of the windward wind barrier divides the area of the relatively small flow velocity variance in the undisturbed freestream flow from the area of the large flow velocity variance close to the top bridge-deck section surface. As the wind-barrier porosity decreases, the flow velocity variance immediately downstream of the wind barrier decreases, while it substantially increases in the wake of the bridge-deck section. Increasing the windward wind-barrier height shifts an adverse area of strong velocity fluctuations upwards, i.e. away from the top surface of the bridge-deck section, thus providing more effective sheltering for vehicles passing the bridge. The profiles of the flow velocity variance at $x/B = 0$ for various porosities and heights of the windward wind barrier are reported in Figure 30.

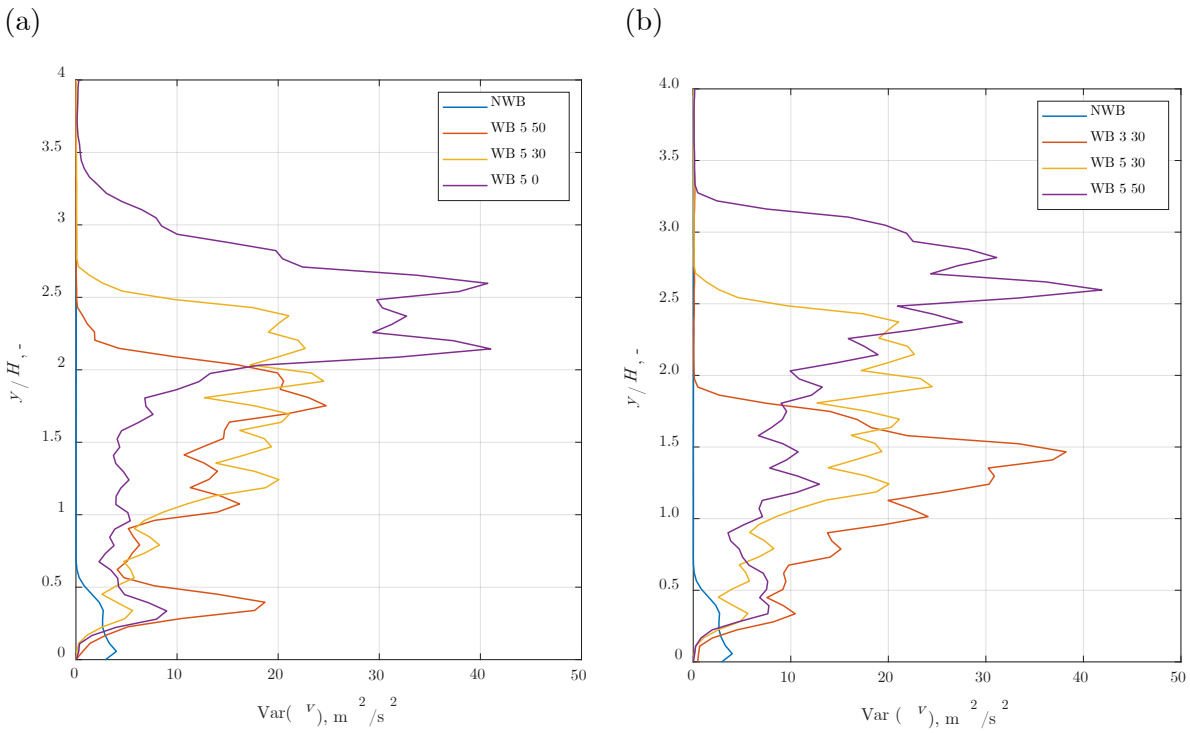

Figure 30: The profiles of the flow velocity variance at $x/B = 0$ for various (a) porosities and (b) heights of the windward wind barrier.

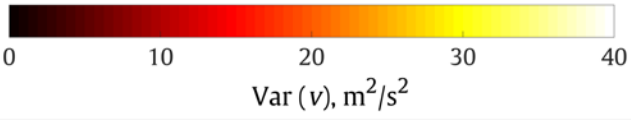

(a) WB 3_30 WW

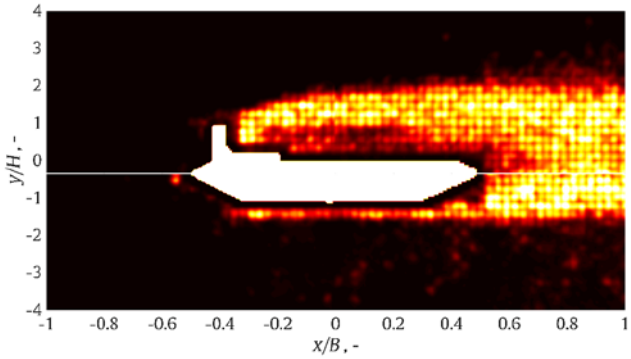

(b) WB 3_30 LW

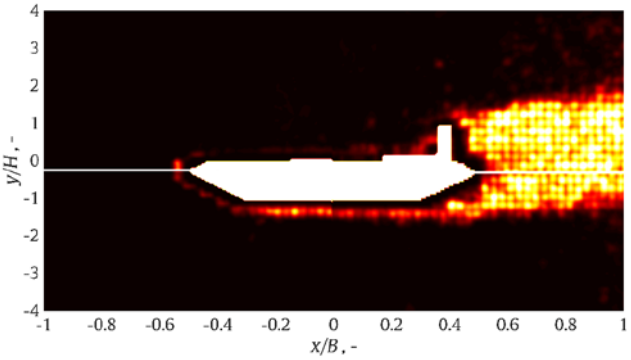

(c) WB 3_30 WW+LW

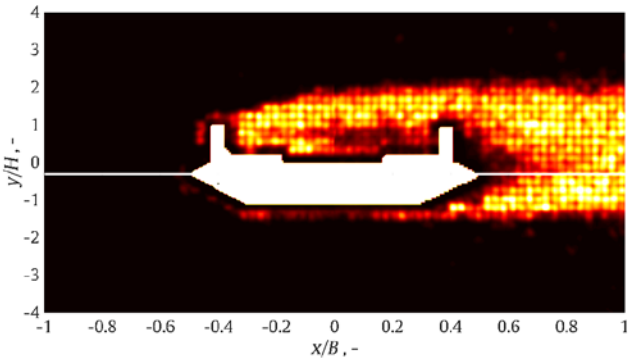

(d) WB 5_30 WW

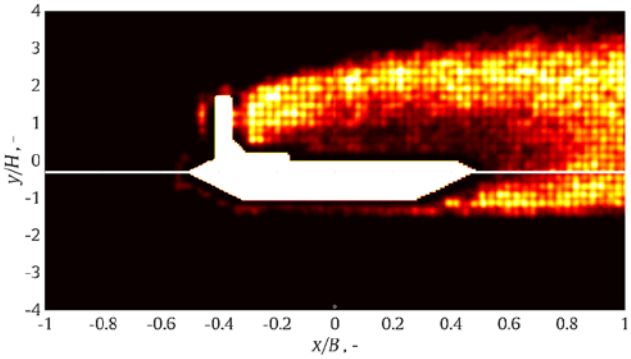

(e) WB 5_30 LW

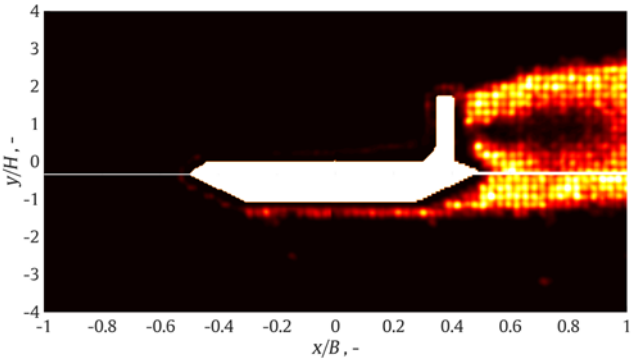

(f) WB 5_30 WW+LW

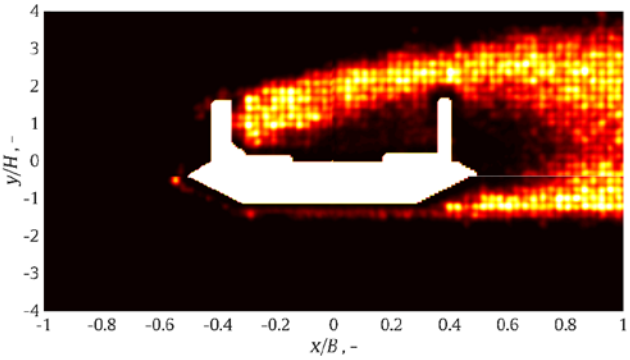

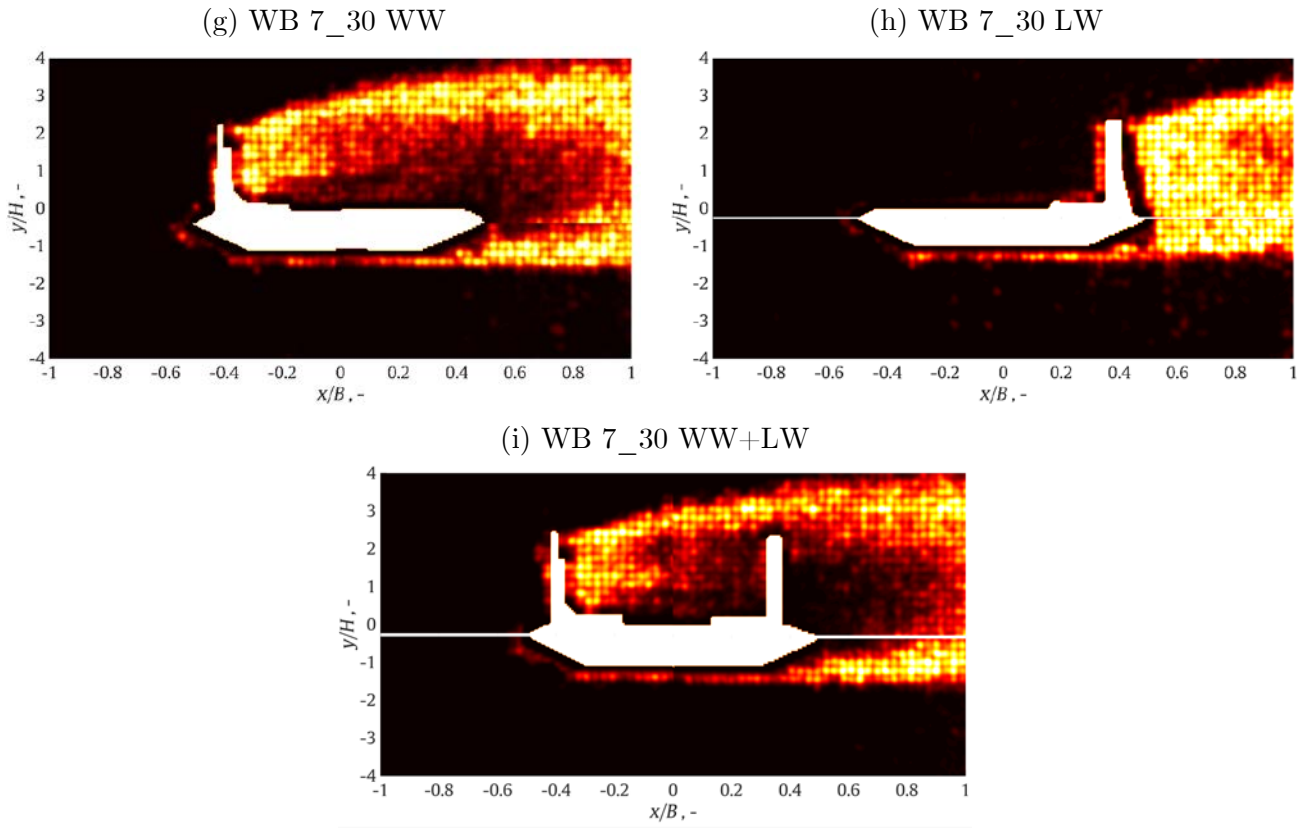

Figure 31: Flow velocity variance around the Great Belt Bridge deck section for various arrangements of wind barriers. Flow direction is from left to right.

Large flow velocity variance above the top bridge-deck section surface is observed for the windward and both windward and leeward wind barriers. This indicates that large pressure fluctuations on the top bridge-deck section surface may be expected in those configurations thus yielding large fluctuations of the aerodynamic forces and moments. The largest flow velocity variance is again in the separated shear layer. When comparing the results for the windward and both windward and leeward wind barriers, discrepancies may be observed above the bridge-deck section due to a recirculating flow between the wind barriers in case both wind barriers are in place. The profiles of the flow velocity variance at $x/B = 0$ for various arrangements of the 5 m high (full-scale) and 50 % porous wind barrier are reported in Figure 32.

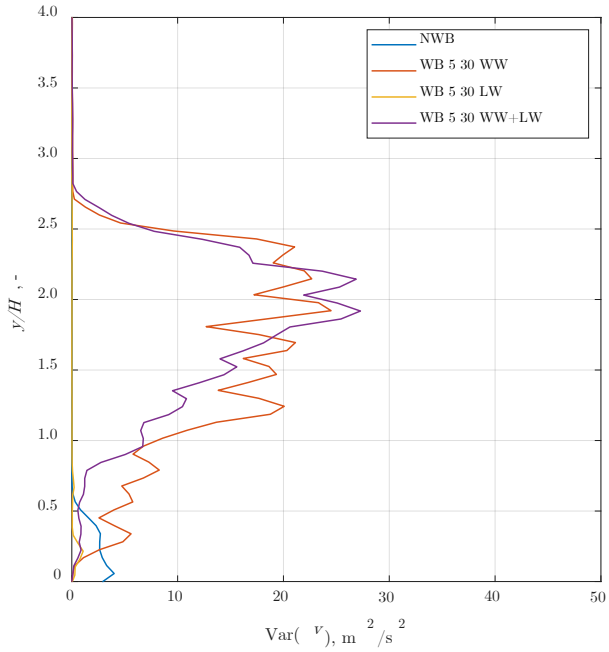

Figure 32: The profiles of the flow velocity variance at x/B = 0 for various arrangements of the 5 m high (full-scale) and 50 % porous wind barrier.

The behavior of the shear layer is well correlated with the flow incidence angle; hence, a small change in the flow incidence angle, e.g. in case of downslope windstorms, may substantially modify the characteristics of the separated shear layer. This suggests that the shear layer that separates from the wind-barrier top may have an important role in the self-excited lift force and the pitch moment that both substantially influence the dynamic behavior of bridge-deck sections.

4.2. Aerodynamic forces and the pitch moment acting on bridge-deck sections

4.2.1. Effects of wind-barrier height and porosity on aerodynamic forces and the pitch moment of bridge-deck sections

Wind barriers of various porosity and height were studied on the windward edge of the bridge-deck sections first. The drag force coefficient is reported in Figure 33 for the flow incidence angles between -10° (upslope flow) and +10° (downslope flow) with an increment of 1°.

The trends in the drag force coefficient obtained for the empty Great Belt Bridge without the wind barrier correspond relatively well to previous studies on similar bridge-deck sections, e.g. Reinhold et al. (1992). Some differences in the results are likely due to minor discrepancies in the Reinhold et al. (1992) H4.1 bridge-deck section used for a validation, and the section tested in the present study. In particular, the H4.1 section in Reinhold et al. (1992) is equipped with guard rails, the top of the bridge-deck surface is not flat (unlike the bridge-deck section tested in the present study), and there are some minor differences in dimensions as well.

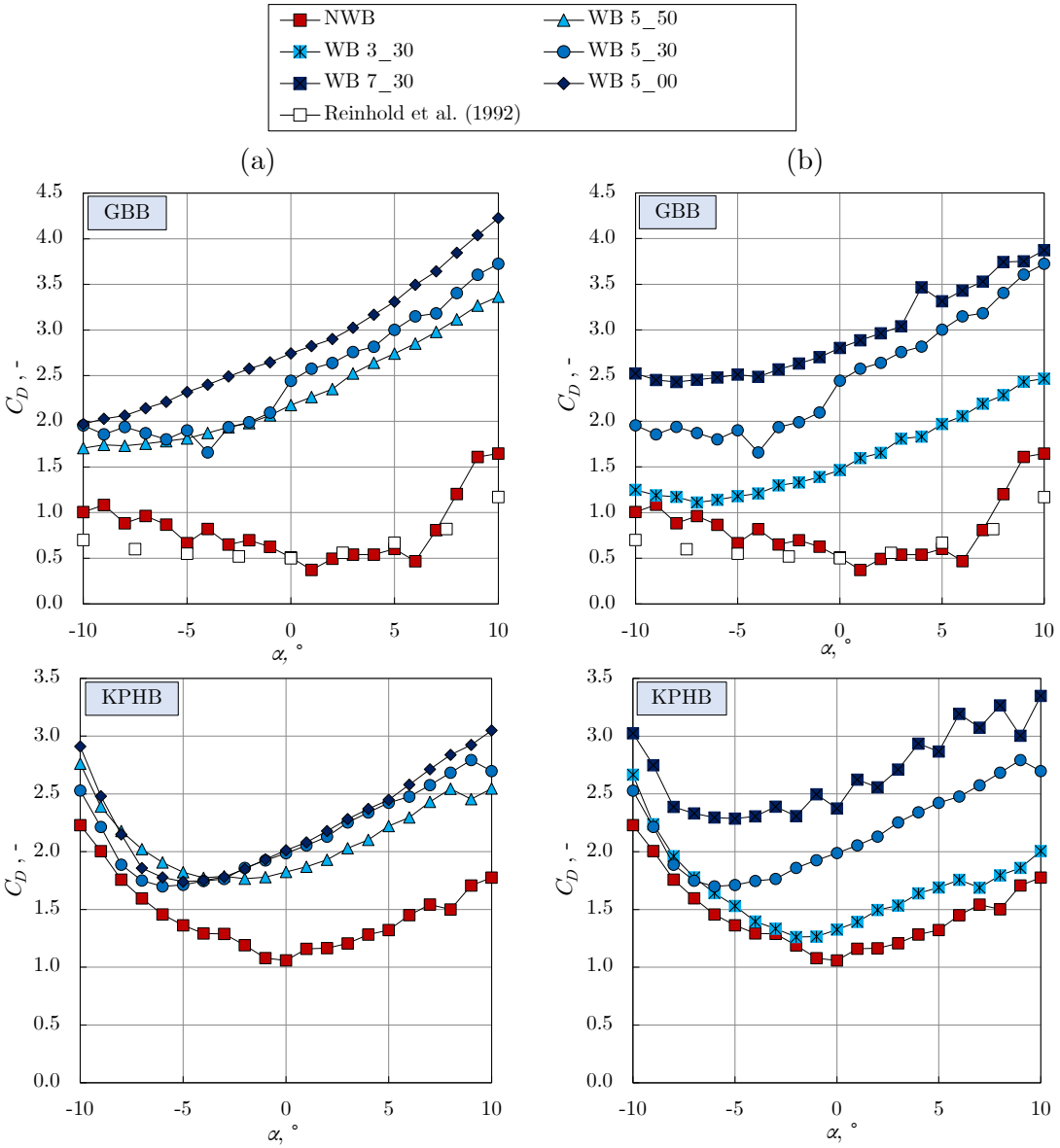

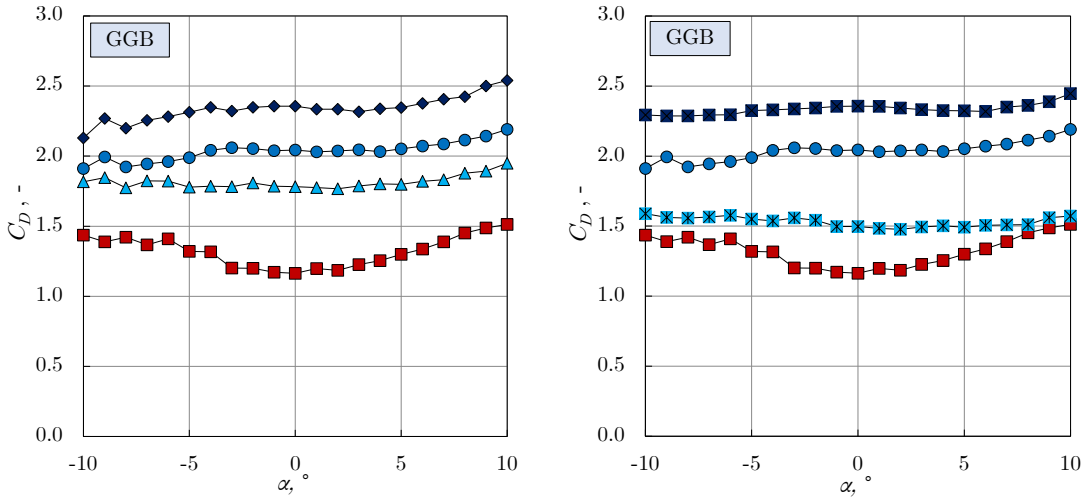

Figure 33: Drag force coefficient for bridge-deck sections with:
(a) 5 m high (full-scale) wind barriers of various porosities,
(b) 30% porous wind barriers of various full-scale heights.

The influence of guard rails on the aerodynamic force and moment coefficients is reported in Simiu and Scanlan (1996) and it corresponds well with the differences in results observed between the bridge deck used in the present study and the H4.1 section used in Reinhold et al. (1992).

Wind barriers generally cause the drag force coefficient to increase in the entire range of investigated flow incidence angles, as the wind barriers present an additional obstacle to the flow. While this trend is observed for all studied bridge-deck sections, for all of them it is more exhibited at positive flow incidence angles. In this range of flow incidence angles, the wind barrier additionally increases the bridge-deck section surface subjected to the flow, while in the range of negative flow incidence angles this surface is partly shadowed by the slope of the bridge-deck section.

A decrease in the wind-barrier porosity increases the bluffness of the bridge-deck sections. The drag force coefficient generally increases as the porosity of the wind barriers decreases. This is observed in the entire range of investigated flow incidence angles for all studied bridge-deck sections, except for the Kao-Pin Hsi Bridge at large negative flow incidence angles.

The drag force coefficient increases as the height of the wind barriers increases. This is observed for all studied bridge-deck sections in the entire range of investigated flow incidence angles. This is due to an increased model area perpendicular to the flow for higher wind

barriers. The influence of the wind-barrier height is more pronounced for positive flow incidence angles.

A relative increase in the drag force coefficient with respect to the empty bridge-deck sections (without the wind barrier) is reported for various wind barriers in Figure 34.

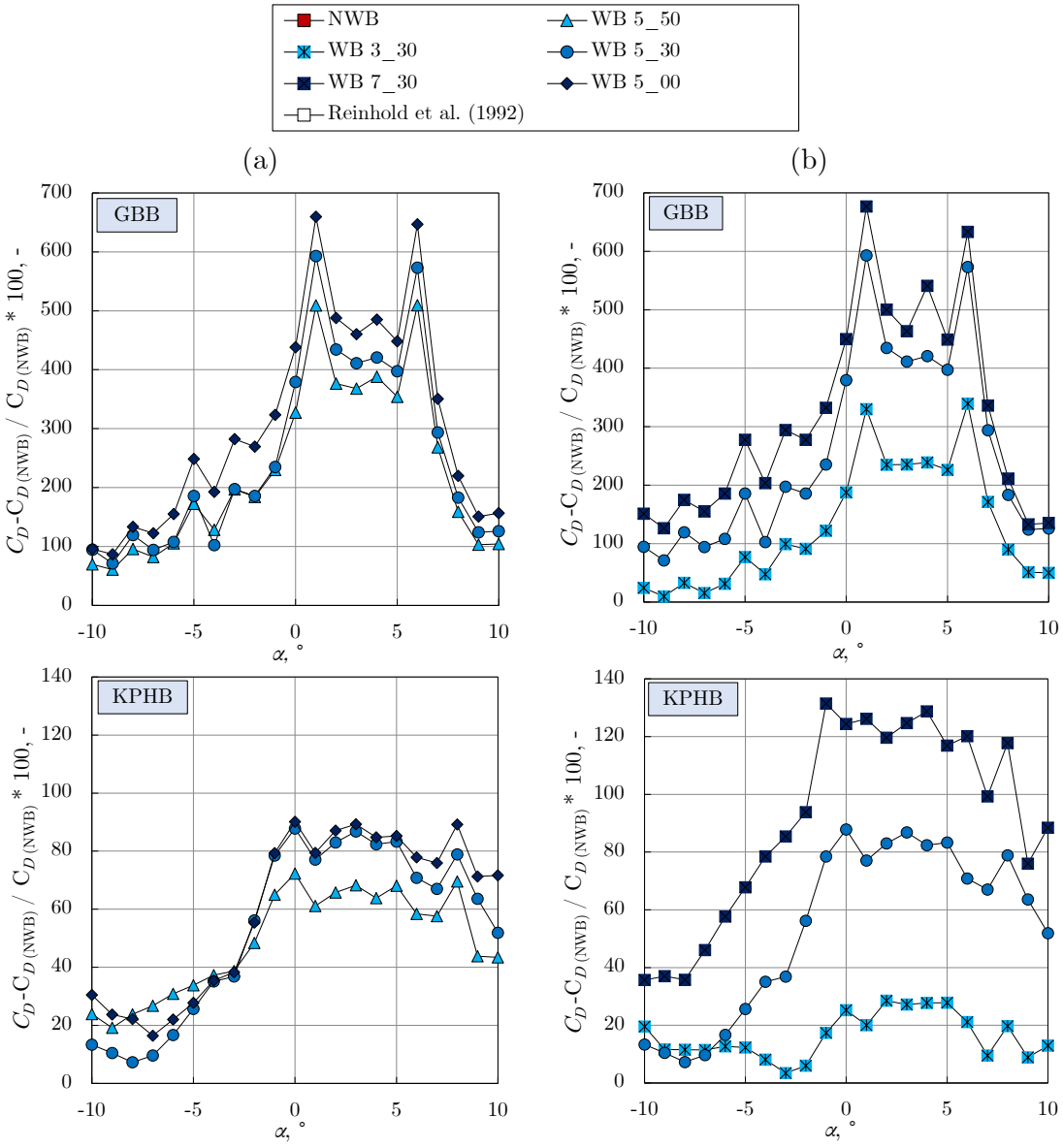

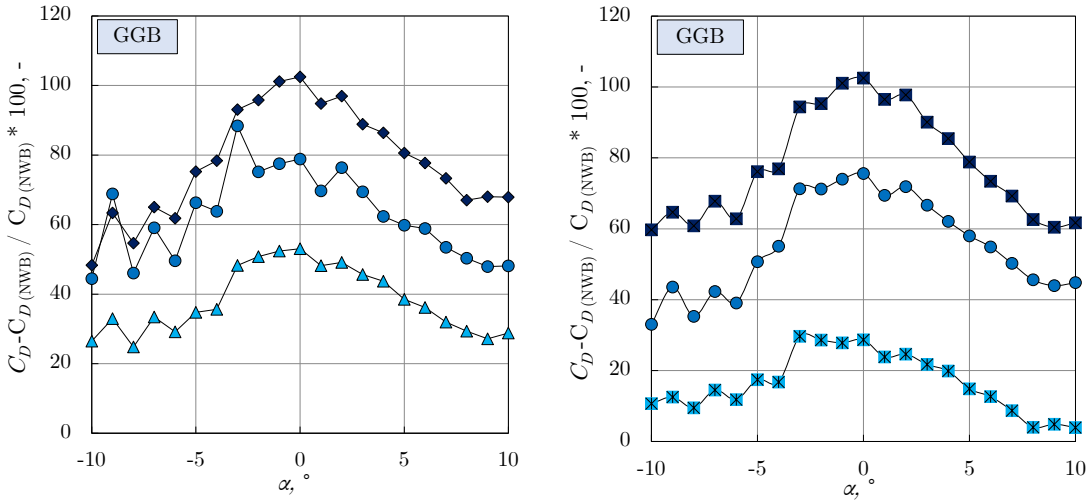

Figure 34: Relative increase in the drag force coefficient in comparison with the empty bridge-deck sections: (a) 5 m high (full-scale) wind barriers of various porosities, (b) 30% porous wind barriers of various heights.

The influence of wind barriers on the increase of the drag force coefficient is more exhibited for the Great Belt Bridge, which is the most streamlined of the three investigated bridge-deck sections. For the Great Belt Bridge, largest relative increases are observed at the 1° and 6° flow incidence angles. An increase in the drag force coefficient due to wind barriers is less exhibited for the Kao-Pin Hsi Bridge and the Golden Gate Bridge. The largest increase of the drag force coefficient for these sections is observed at the 0° flow incidence angle.

The lift force coefficient is reported in Figure 35 for the flow incidence angles between -10° and +10° with an increment of 1°.

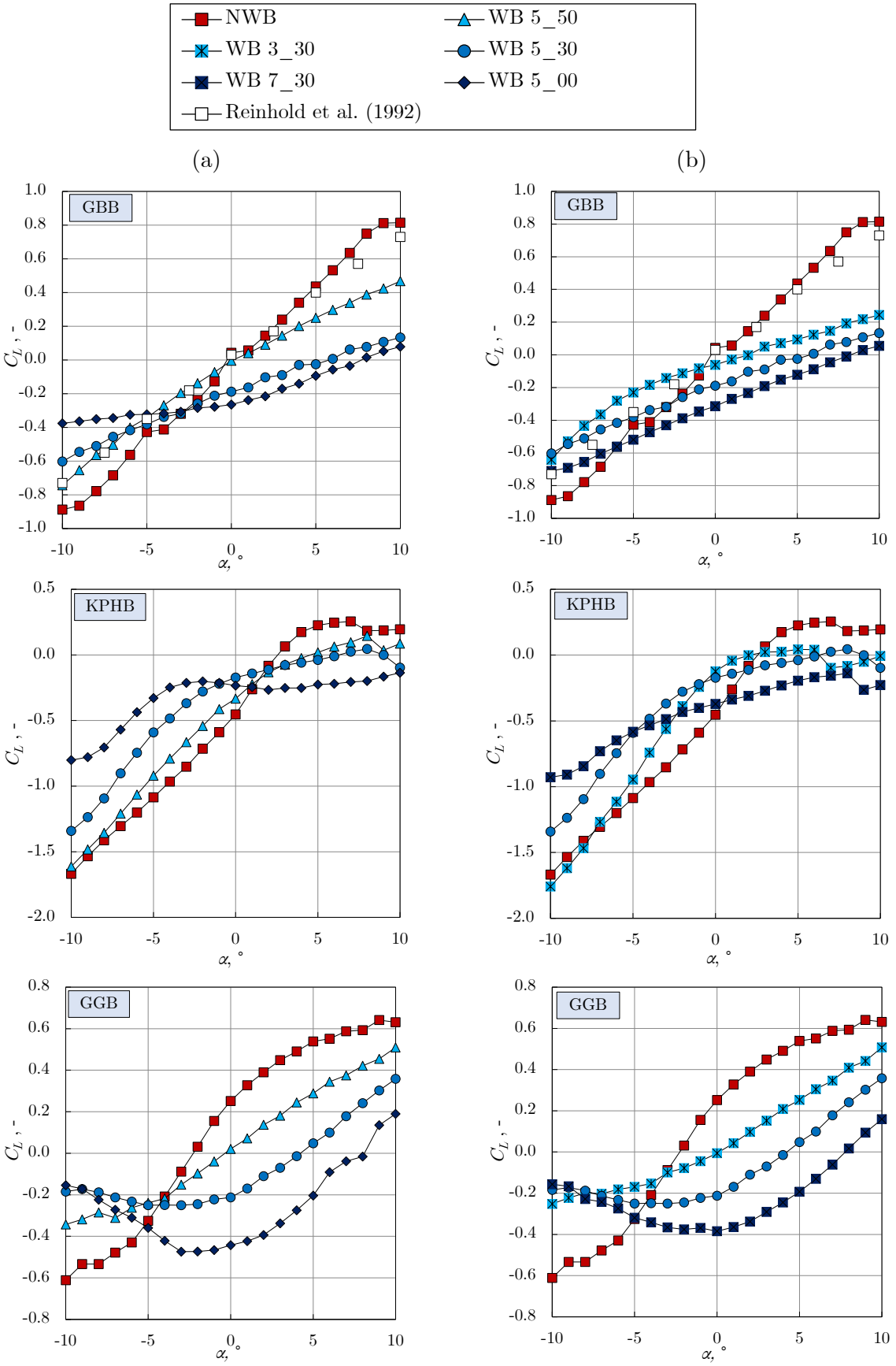

Figure 35: Lift force coefficient for bridge-deck sections with: (a) 5 m high (full-scale) wind barriers of various porosities, (b) 30% porous wind barriers of various full-scale heights.

General trends in the lift force coefficient for all studied bridge-deck sections without the wind barrier are similar, as the lift force coefficient increases with increasing the flow incidence angle from -10° to +10°.

Wind barriers modify the trends and absolute values of the lift force coefficient, i.e. wind barriers generally cause a decrease in the absolute values of the lift force coefficient at large positive and large negative flow incidence angles. The influence of wind barriers on the lift force coefficient increases as the porosity of the wind barriers decreases. This may cause the lift force to change the direction from positive to negative, e.g. the Golden Gate Bridge with the WB 5_30 for $0° < \alpha < 4°$ and the WB 5_00 for $0° < \alpha < 8°$.

The effects of wind barriers on the lift force coefficient increase with increasing the height of wind barriers, i.e. the differences in the results with respect to the empty bridge-deck sections are larger for higher wind barriers. This is more clearly exhibited for the more bluff Golden Gate Bridge section.

Coefficients of the aerodynamic pitch moment are reported in Figure 36 for the flow incidence angles between -10° and +10° with an increment of 1°.

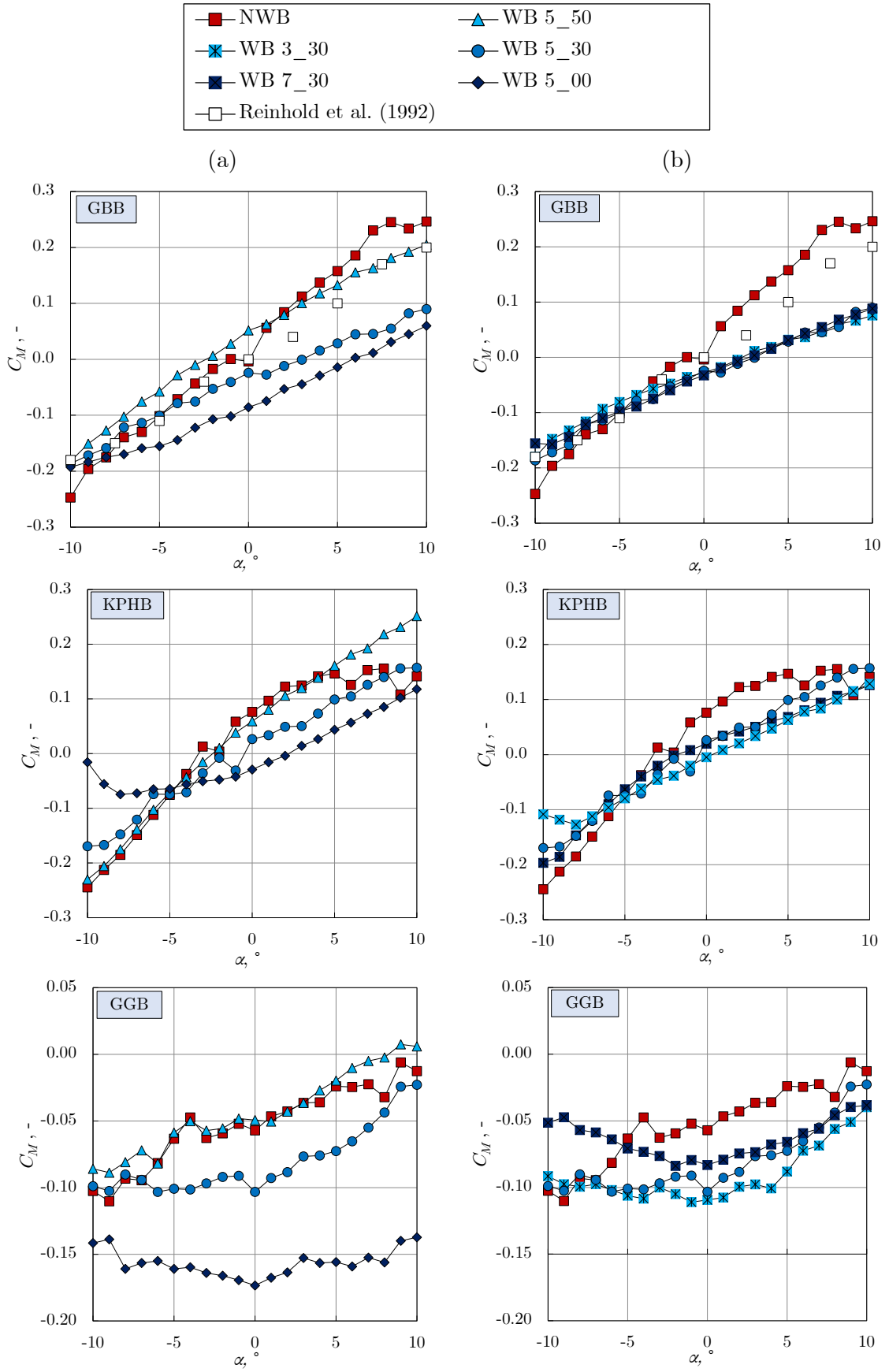

Figure 36: Pitch moment coefficient for bridge-deck sections with: (a) 5 m high (full-scale) wind barriers of various porosities, (b) 30% porous wind barriers of various full-scale heights.

The influence of wind barriers on the pitch moment is present in all studied configurations, both when changing the wind-barrier porosity and its height. The pitch moment generally decreases when the wind barriers are in place, likely due to the flow separation and reattachment phenomena that influence the surface pressure distribution on the bridge-deck sections. Wind barriers contribute to the negative pitch moment, which is more pronounced as the wind-barrier porosity decreases. While there is a change in the pitch moment coefficient for studied wind barriers with respect to the empty bridge-deck sections, a discrepancy in the results for wind barriers of various heights are relatively minor for the Great Belt Bridge and the Kao-Pin Hsi Bridge, and somewhat larger for the Golden Gate Bridge, particularly for smaller wind barriers.

4.2.2. Effects of wind-barrier arrangement on aerodynamic forces and the pitch moment of bridge-deck sections

The drag force coefficient is presented in Figure 37 for the flow incidence angles from -10° to 10°.

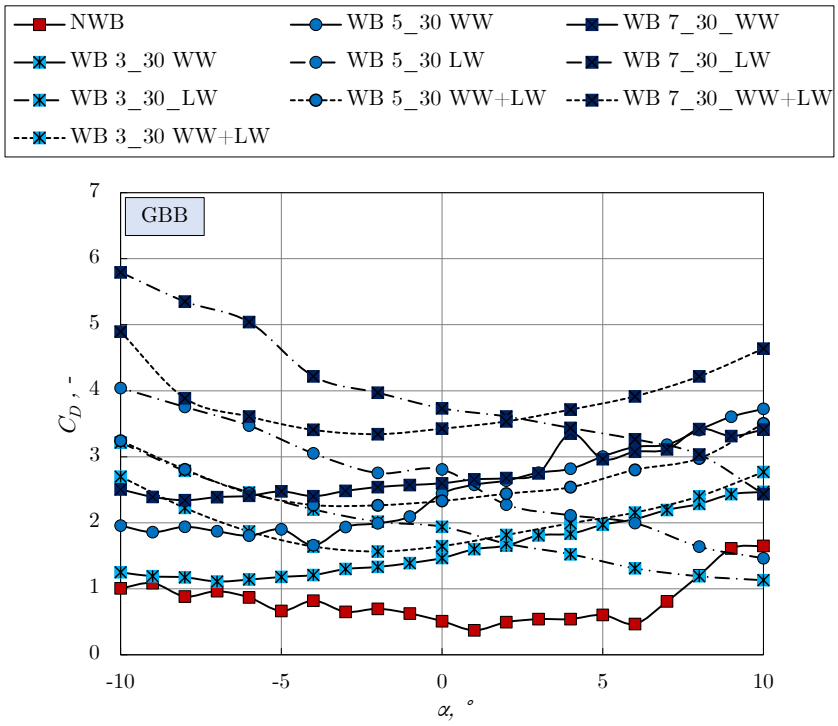

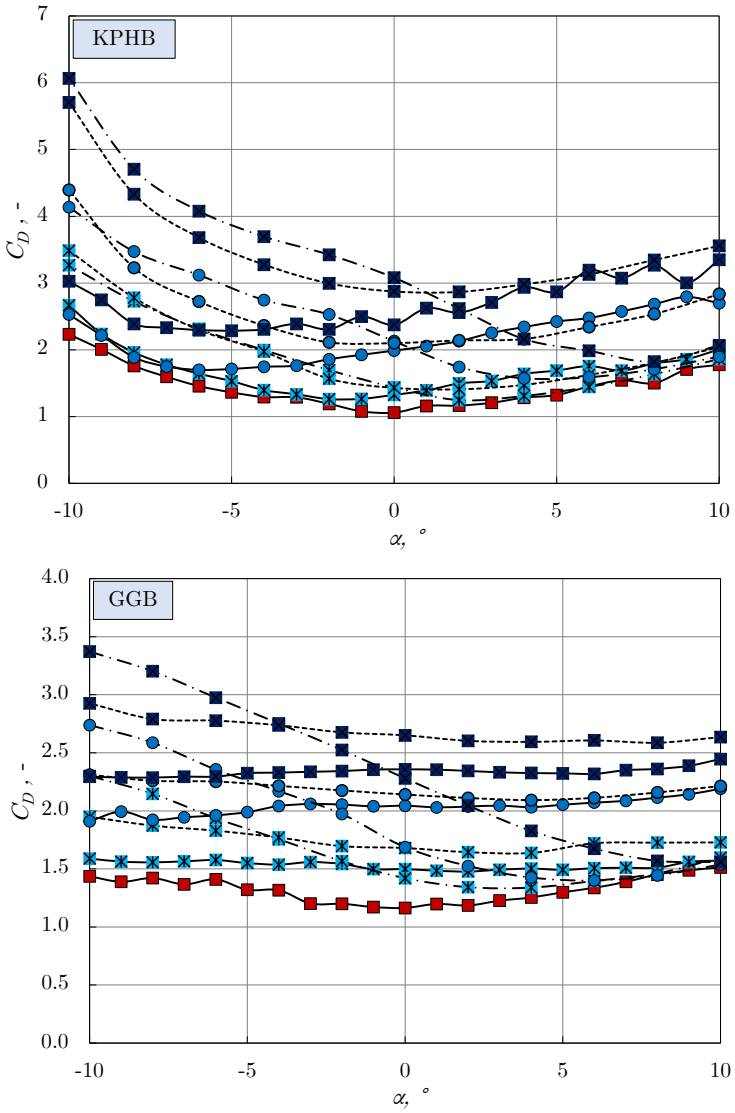

Figure 37: Drag force coefficient for various arrangements of wind barriers at various flow incidence angles.

The drag force coefficient proved to be very dependent on the arrangement of wind barriers. For the large negative flow incidence angles, the leeward wind barrier increases the most the drag force coefficient. In this range of the flow incidence angles, the windward wind barrier is partly shadowed by the bridge-deck section and its influence on the obtained drag force coefficient is smaller. The smallest relative increase in the drag force coefficient is obtained for the windward wind barrier.

As the flow incidence angle approaches zero and has small positive values, the influence of the leeward wind barrier decreases, while the largest relative increase in the drag force coefficient is observed for both windward and leeward wind barriers.

This is due to the characteristic flow recirculation zone in between the windward and leeward wind barriers in agreement with Avila-Sanchez et al. (2016). As the flow incidence angle further increases, the influence of the leeward wind barrier becomes smaller, while both wind barriers still have the largest influence on the drag force coefficient.

The wind-barrier layout strongly influences the lift force coefficient, Figure 38.

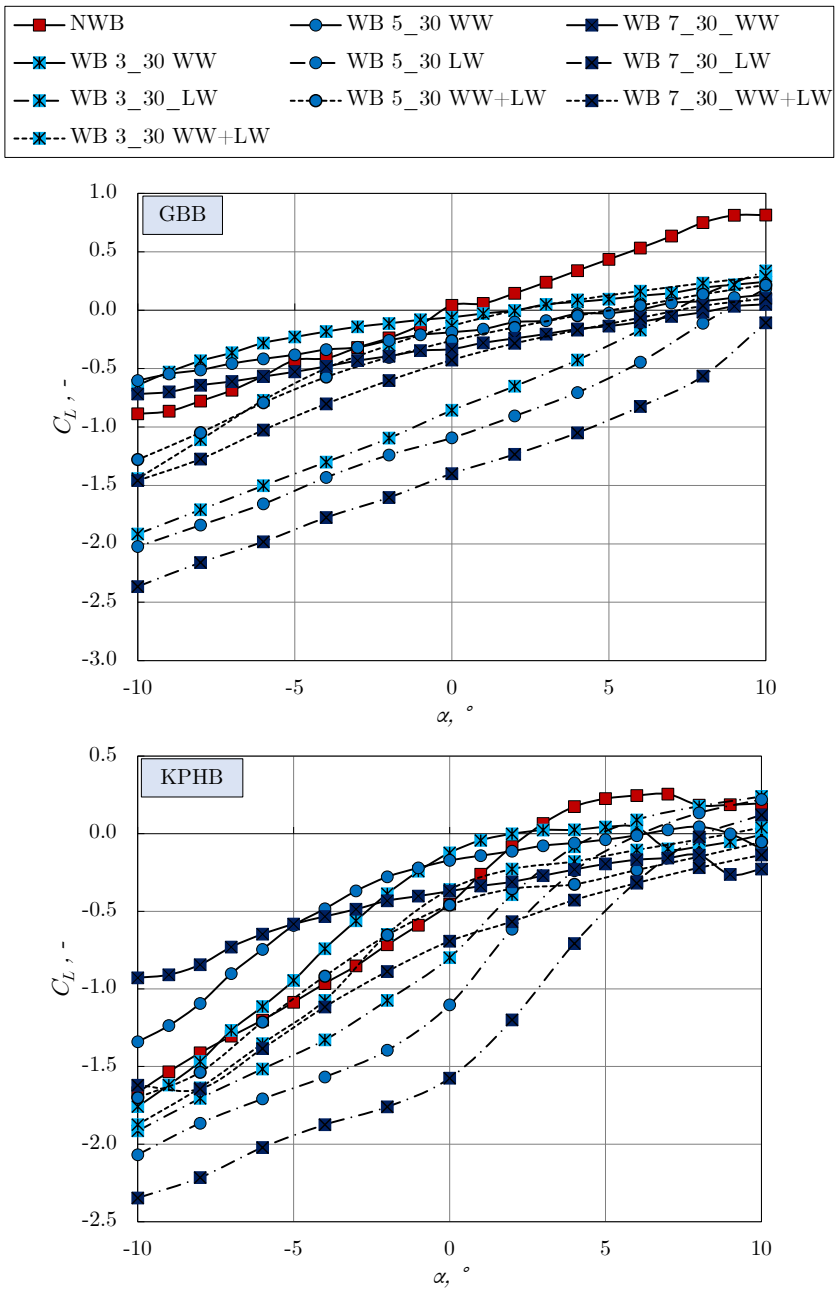

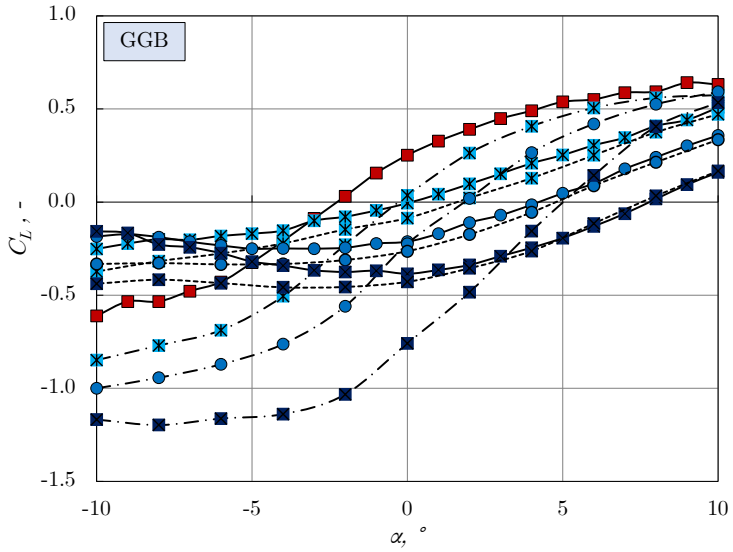

Figure 38: Lift force coefficient for various arrangements of wind barriers at various flow incidence angles.

The direction of the lift force is particularly important as it substantially determines the integral aerodynamic loads on bridge decks. For the negative flow incidence angles, the leeward wind barrier significantly increases the absolute values of the lift force coefficient. The leeward wind barrier may actually act as a Gurney flap, e.g. Zanotti and Gibertini (2018), as it increases the pressure on the top surface of the bridge-deck section, decreases the pressure on the bottom surface of the bridge deck and thus enables the flow to remain attached to the bridge-deck section. In case both windward and leeward wind barriers are in place, the lift force coefficient is slightly larger than without the wind barriers, while it is slightly smaller for the windward wind barrier only.

In the proximity of the zero flow incidence angle, the leeward wind barrier may significantly modify the lift force coefficient and change the direction of the integral lift force. In the range of the positive flow incidence angles, all types of the wind barrier contribute to the negative lift force. In some configurations, the wind barrier changes the direction of the lift force from positive to negative, which is particularly exhibited for the leeward wind barrier. The arrangement of wind barriers does not significantly influence the pitch moment coefficient of the studied bridge-decks sections, Figure 39.

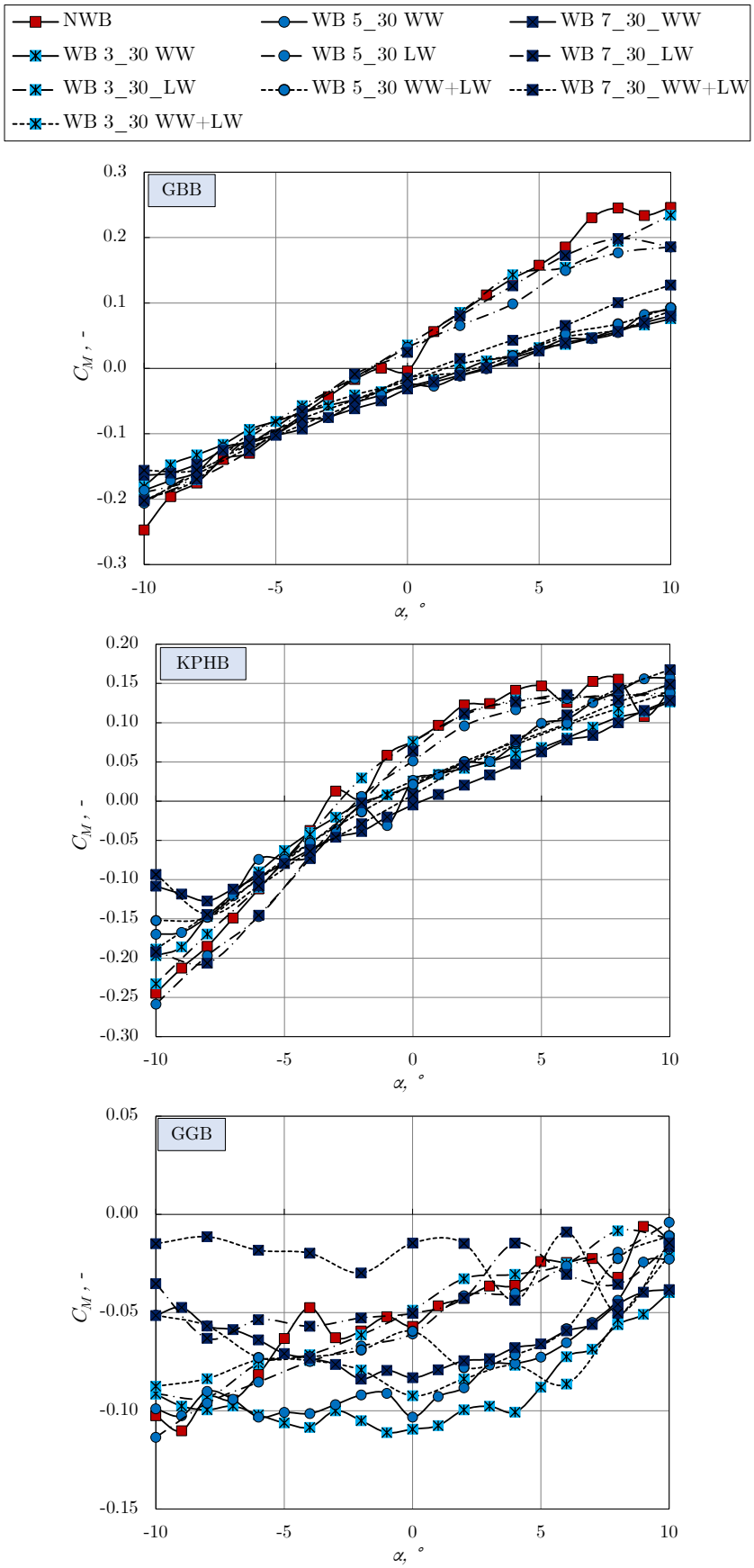

Figure 39: Pitch moment coefficient for various arrangements of wind barriers at various flow incidence angles.

For the negative flow incidence angles, the discrepancies among various types of the wind barrier are small. For the positive flow incidence angles, the leeward wind barrier does not affect the pitch moment coefficient. The windward and both windward and leeward wind barriers may contribute to the negative pitch moment coefficient, but their qualitative influence is still small. This indicates that the orientation and placement of the wind barriers does not affect the torsional divergence type of instability for the bridge-deck sections.

4.3. Galloping stability of bridge-deck sections with wind barriers

The gradient of the lift force coefficient with respect to the flow incidence angle α is reported for all studied configurations in Figure 40 to analyze the galloping sensitivity of the studied bridge-deck sections. The gradient of the lift force coefficient with respect to the flow incidence angle is important for the quasi-steady analysis of the galloping instability. The reduced frequency of galloping oscillations is relatively small, hence the aerodynamic forces acting on the bridge-deck sections may be assumed as acting on the body in the steady flow. The negative slope of the lift force coefficient curve is not favorable, as it yields negative gradient of the lift force coefficient, which is a prerequisite for the dynamic instability in the heave direction.

However, only when the absolute value of the negative gradient in the lift force coefficient is larger than the drag force coefficient at the same flow incidence angle, the necessary condition for the galloping instability is satisfied.

The gradients were fitted using the 4^{th} degree polynomial functions of the lift force coefficient with respect to α.

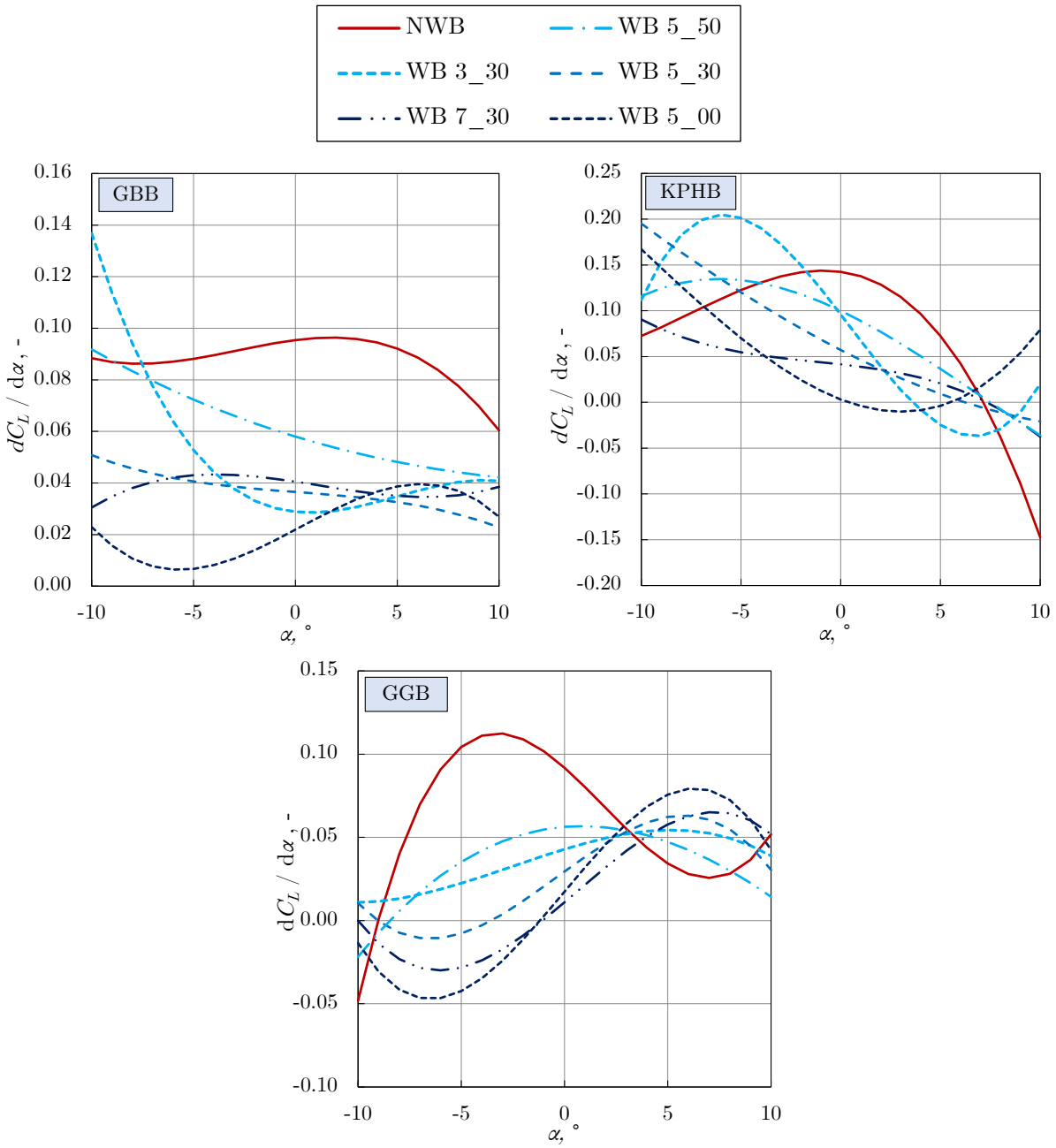

Figure 40: Gradient of the lift force coefficient with respect to the flow incidence angle for all studied bridge-deck sections with the windward wind barrier.

Based on the results for the drag force coefficient (Figure 33) and the gradient of the lift force coefficient with respect to α (Figure 36), the Glauert-Den Hartog criterion for galloping is positive for all studied bridge-deck sections with and without the wind barrier in the entire range of the investigated flow incidence angles.

Even though the gradient of the lift force coefficient exhibits negative values for the Kao-Pin Hsi Bridge at large positive flow incidence angles and the Golden Gate Bridge at negative

flow incidence angles, the absolute values of the gradient are smaller than the drag force coefficient at respective angles, thus the necessary galloping criterion for the bridge-deck sections is not satisfied.

This suggests that wind barriers placed at the windward edge of wide long-span cable-supported bridge decks do not make those bridge decks more sensitive to galloping in comparison with the respective empty bridge decks without wind barriers. The same behavior of the bridge-deck sections was observed in all other arrangements of wind barriers as well, i.e. the studied bridge-deck sections remain stable with respect to galloping no matter which type of the wind barrier is placed on the bridge deck. Those additional results were however not reported for brevity.

4.4. Flutter sensitivity of bridge-deck sections with wind barriers

2DOF FDs are reported with respect to the reduced flow velocity v/fB. They are normalized using the heave natural frequency of oscillation for H_1^*, H_4^*, A_1^*, A_4^* and the pitch natural frequency of oscillation for H_2^*, H_3^*, A_2^*, A_3^*, whereas the natural frequencies of oscillations were determined in the still air.

The obtained results compare relatively well with previous relevant studies on similar empty bridge-deck sections, e.g. Poulsen et al. (1992), Simiu and Scanlan (1996), (shown in diagrams), as well as with Seo and Caracoglia, (2011), Canor et al. (2015) (not shown in diagrams for brevity). Nevertheless, some minor discrepancies are likely due to differences in the bridge-deck section design used in the present thesis in comparison with the bridge-deck sections analyzed in those respective studies. It is important to note that the sign of the indirect FDs reported in Simiu and Scanlan (1996) is changed in order to be compliant with the sign convention adopted in this thesis.

4.4.1. Effects of wind-barrier height and porosity on flutter sensitivity of bridge-deck sections with wind barriers

H_i^* (i = 1, 2, 3) FDs are reported for various heights and porosities of wind barriers in Figure 41, Figure 43 and Figure 44.

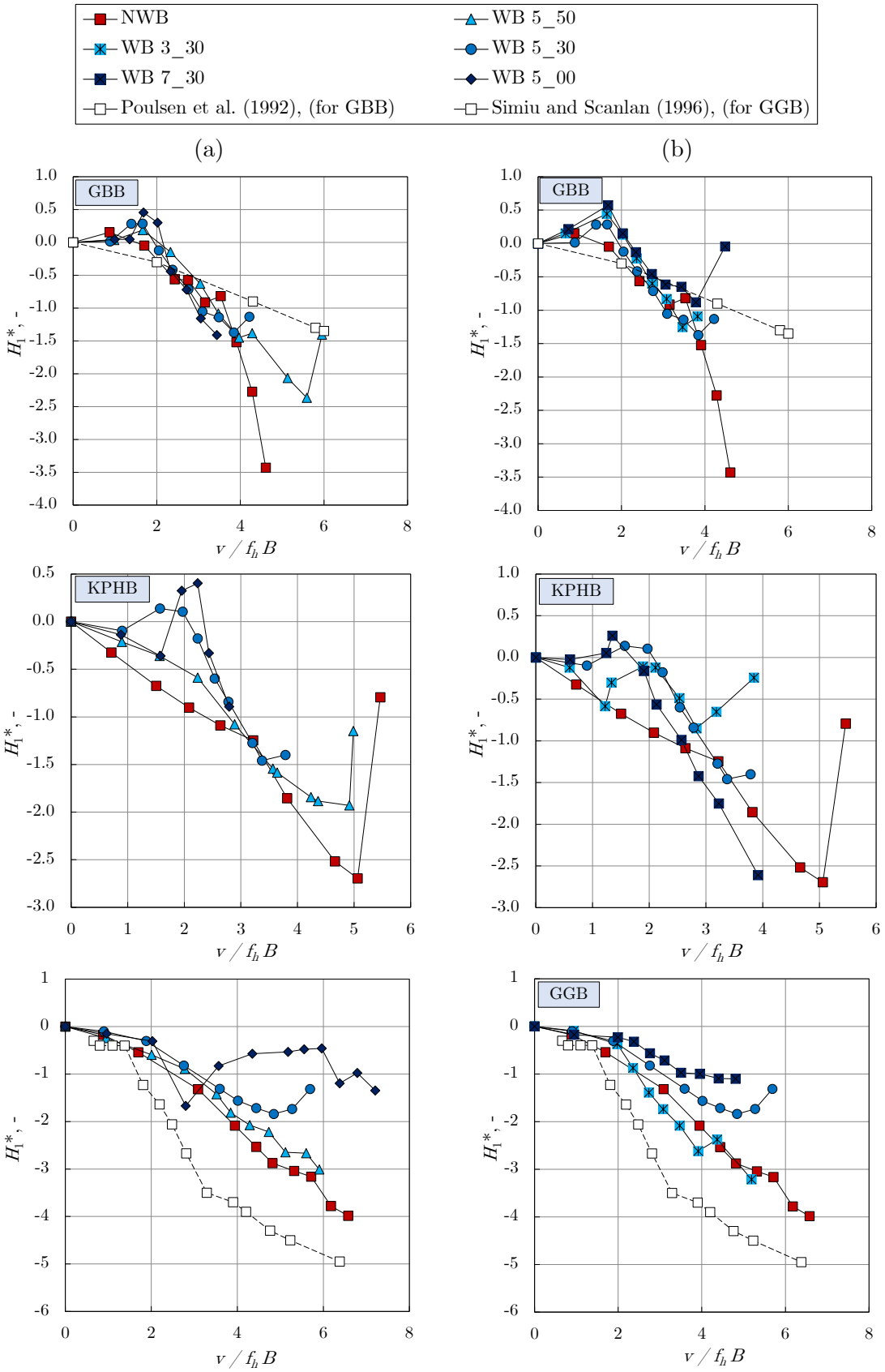

Figure 41: H_1^* FD for bridge-deck sections with:

(a) 5 m high (full-scale) wind barriers of various porosities (0%, 30%, and 50%), (b) 30% porous wind barriers of various full-scale heights (3 m, 5 m, and 7 m).

The direct H_1^* FD is the term in the equation of motion that addresses the gradient of the self-excited lift force with respect to the velocity of a bridge deck in the heave direction. It is the most important FD for the analysis of the heave motion, as it describes the damping behavior in the heave motion due to the aerodynamic self-excited lift forces.

The positive H_1^* values are achieved for the negative aerodynamic damping; hence, this indicates the bridge-deck section susceptibility to the heave dynamic instability. In case the positive H_1^* is so large that the negative aerodynamic damping is larger than the structural damping, the system becomes unstable in the heave motion. The cross-sections of contemporary long-span cable-supported bridges are usually not sensitive to the self-excited instability in the heave motion, Xu (2013). However, wind barriers may dramatically increase the bluffness of the bridge-deck cross-section; hence, it is necessary to perform the tests on such bridges to assure for a safe bridge design.

The studied bridge-deck sections generally remain stable with respect to the heave motion, as H_1^* remains negative except around v/f_hB = 1.5 - 2.5 for the Kao-Pin Hsi Bridge and the Great Belt Bridge, which is more exhibited for less-porous wind barriers, i.e. WB 5_00 and WB 5_30.

This is likely due to the fluctuating lift force that develops only in certain range of flow velocities when the characteristic frequency of vortices shed from the wind barrier is equal to the heave natural frequency of the system. H_1^* becomes negative with the increase in the flow velocity. The effect of decreasing wind-barrier porosity is more exhibited for the Golden Gate Bridge than for two other bridge-deck sections.

As an example, the amplitude spectrum of the airflow velocity in the wake of the Great Belt Bridge with WB 5_00 is reported in Figure 42. The airflow velocity signal was captured 50 mm downstream of the model in 15 mm height with respect to the top surface of the bridge-deck section model. One can see the dominant frequency of the vortices shed from the model f_v = 22 Hz, while the undisturbed airflow velocity in this experiment was v = 10 m/s. This yields the Strouhal number for the bridge-barrier system equal to St = $f_v h/v$ = 0.198 (calculated using the height of the bridge-deck section model also encompassing the model wind-barrier height h = 0.09 m).

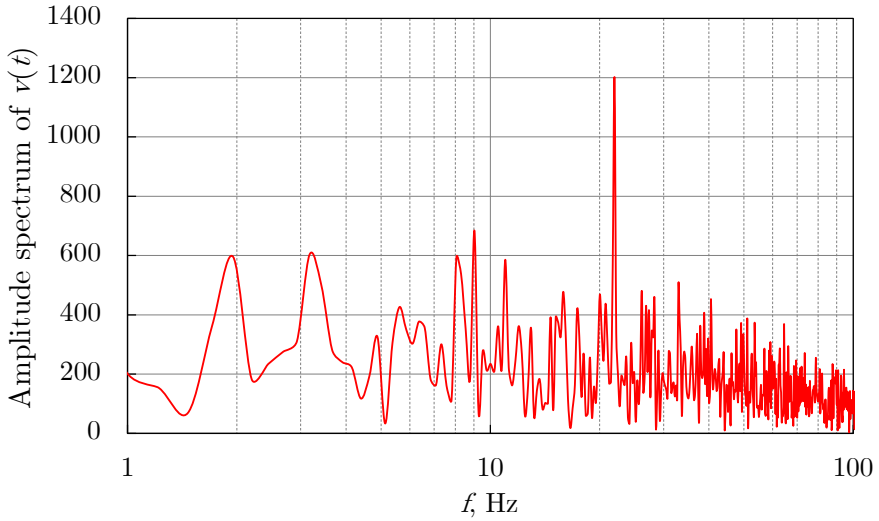

Figure 42: Amplitude spectrum of v(t) for the GBB with WB 5_ 00; measurement position is 50 mm downstream of the bridge-deck section model in 15 mm height with respect to the top surface of the bridge-deck section model.

The natural frequency in the heave motion for this respective configuration in the free-vibration tests is 2.8 Hz; hence, the reduced flow velocity for the vortex shedding to appear (according to Strouhal number equal to 0.198) is approximately 1.5. The trends in H_1^* for this configuration indeed show that the vertical oscillations are present at this particular reduced flow velocity.

The height of the wind barrier does not considerably affect the dynamic stability in the heave direction, as H_1^* is generally negative for all studied bridge-deck sections. Adverse positive values of H_1^* are observed for the Great Belt Bridge and the Kao-Pin Hsi Bridge with wind barriers in place for the reduced flow velocity v/f_hB = 1 - 2, which is likely due to the vortex shedding.

As the reduced flow velocity increases, the vortex shedding frequency increases and this phenomenon vanishes. The effect of increasing wind-barrier height is more exhibited for the Golden Gate Bridge than for two other bridge-deck sections.

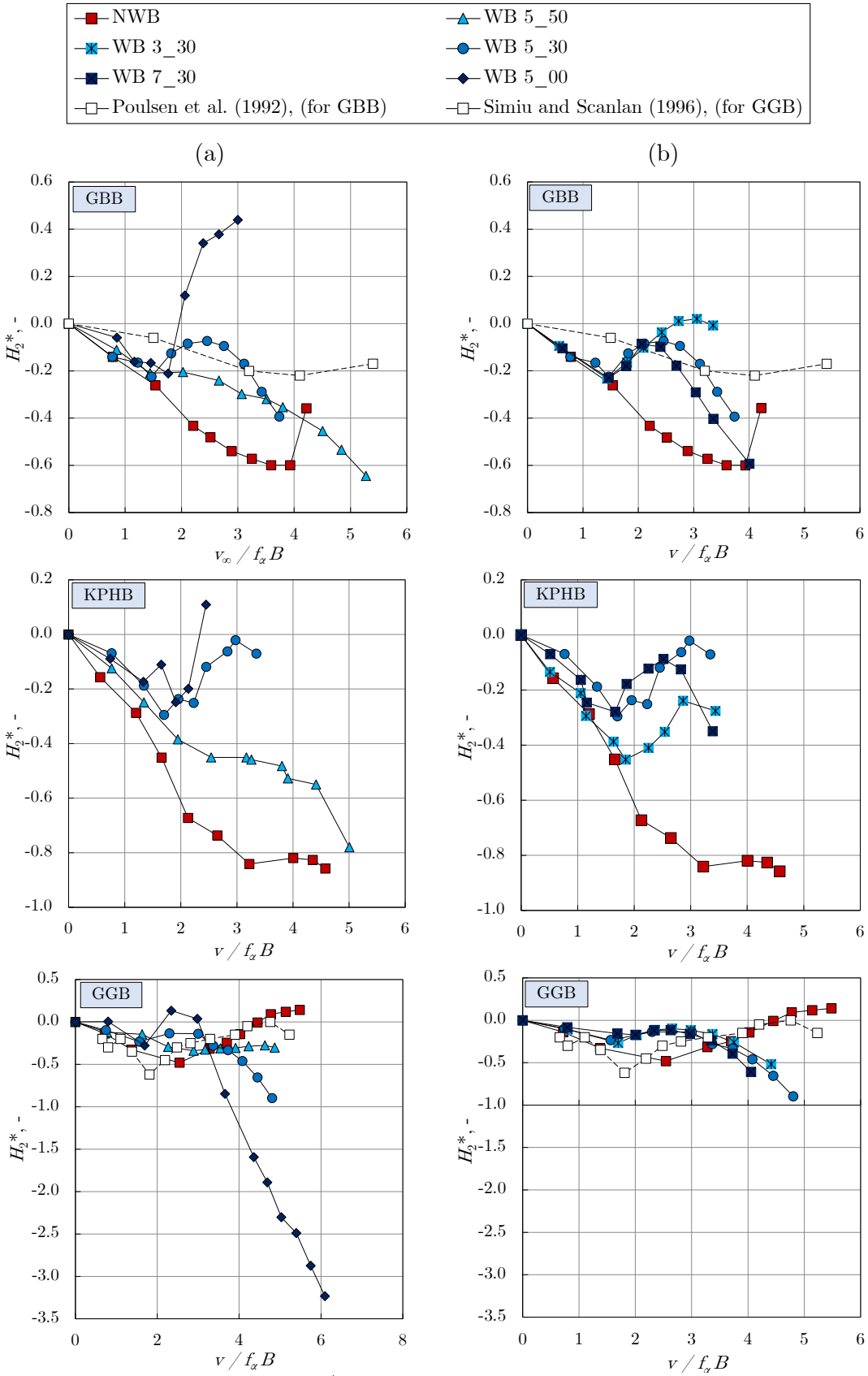

Figure 43: H_2^* FD for bridge-deck sections with:

(a) 5 m high (full-scale) wind barriers of various porosities (0%, 30%, and 50%), (b) 30% porous wind barriers of various full-scale heights (3 m, 5 m, and 7 m).

The indirect H_2^* FD addresses the gradient of the self-excited lift force with respect to the velocity of a bridge deck in the pitch direction.

The influence of the wind-barrier porosity on H_2^* is not the same for three studied bridge-deck sections. In particular, wind barriers contribute to the negative H_2^* for the Golden Gate Bridge, while they contribute to the positive H_2^* for the Kao-Pin Hsi Bridge and the Great Belt Bridge. This is more emphasized for less-porous wind barriers.

The effect of increasing wind-barrier height is more exhibited for the more streamlined Great Belt Bridge than for two other bridge-deck sections.

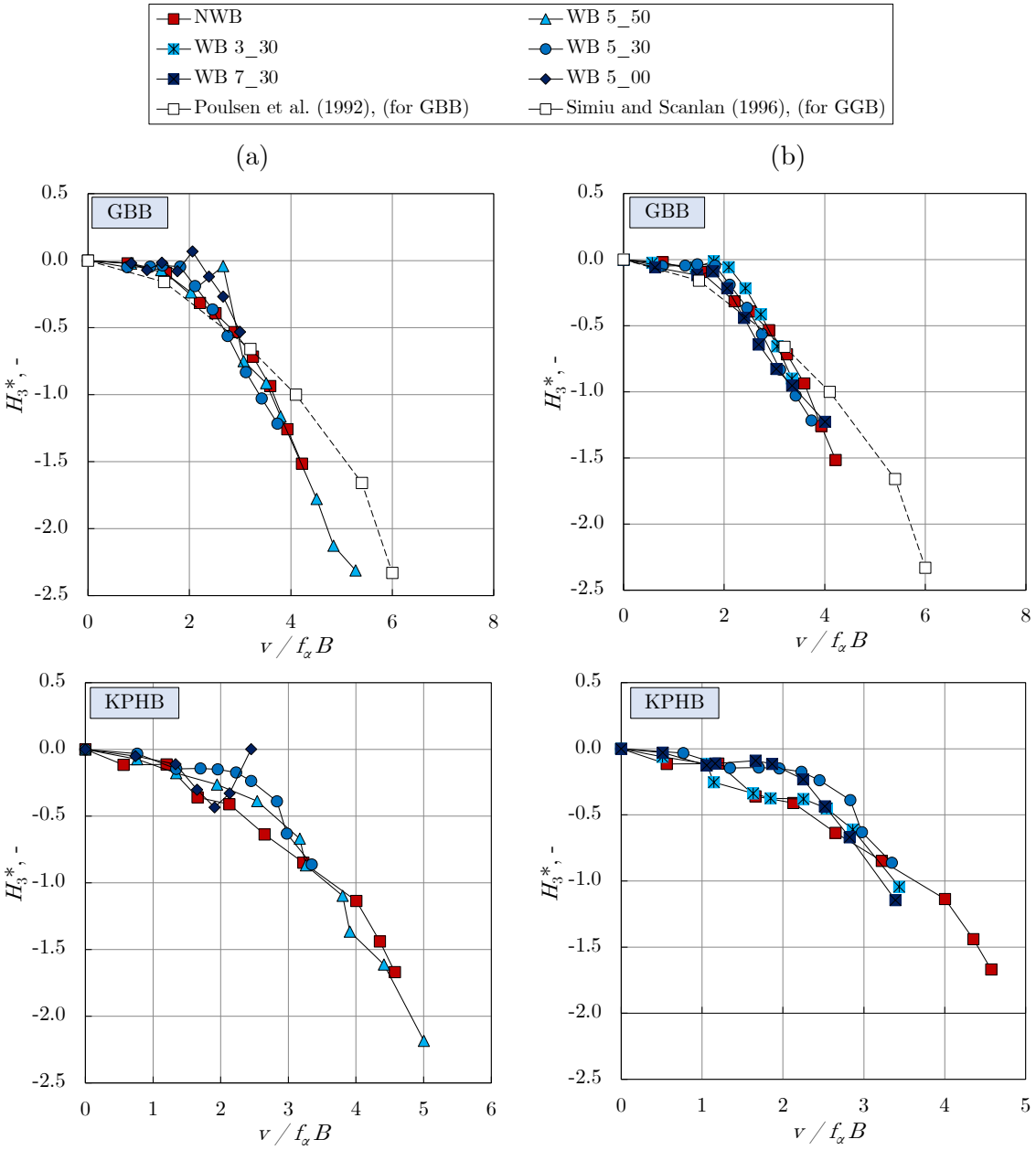

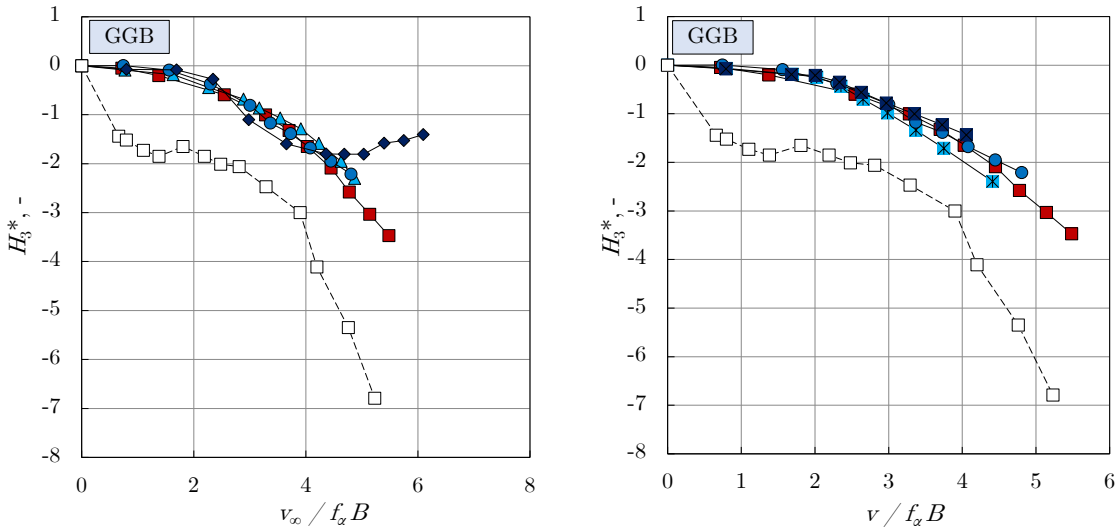

Figure 44: H_3^* FD for bridge-deck sections with: (a) 5 m high (full-scale) wind barriers of various porosities (0%, 30%, and 50%), (b) 30% porous wind barriers of various full-scale heights (3 m, 5 m, and 7 m).

The indirect H_3^* FD addresses the gradient of the self-excited lift force with respect to the pitch angle of a bridge deck.

The obtained results are nearly the same for the empty bridge-deck sections and the bridge-deck sections with wind barriers of all studied porosities. For the Kao-Pin Hsi Bridge and the Golden Gate Bridge, there is a larger discrepancy for the solid wind barrier (WB 5_00) at larger reduced flow velocities in comparison with other configurations. This indicates a slightly smaller influence of the pitch angle on the self-excited lift force for the bridge-deck sections with WB 5_00.

The influence of increasing the wind-barrier height on H_3^* is not that significant, as the results in all studied configurations, including the empty bridge-deck sections, are nearly the same.

The direct H_4^* FD addresses the gradient of the self-excited lift force with respect to the heave displacement of a bridge deck. It has rather unpredictable behavior; hence, it is commonly not analyzed in detail and not shown in diagrams. In fact, H_4^* was not included in the original formulation by Scanlan and Tomko (1971) neither.

There is a strong increase in H_4^* for the Great Belt Bridge with WB 5_50, while for the Golden Gate Bridge the H_4^* absolute values decrease with decreasing the wind-barrier porosity.

While there are no clear indications about the influence of the increasing wind-barrier height on H_4^*, for the Golden Gate Bridge the H_4^* absolute values are smaller for all studied wind-barrier heights in comparison with the empty bridge-deck section.

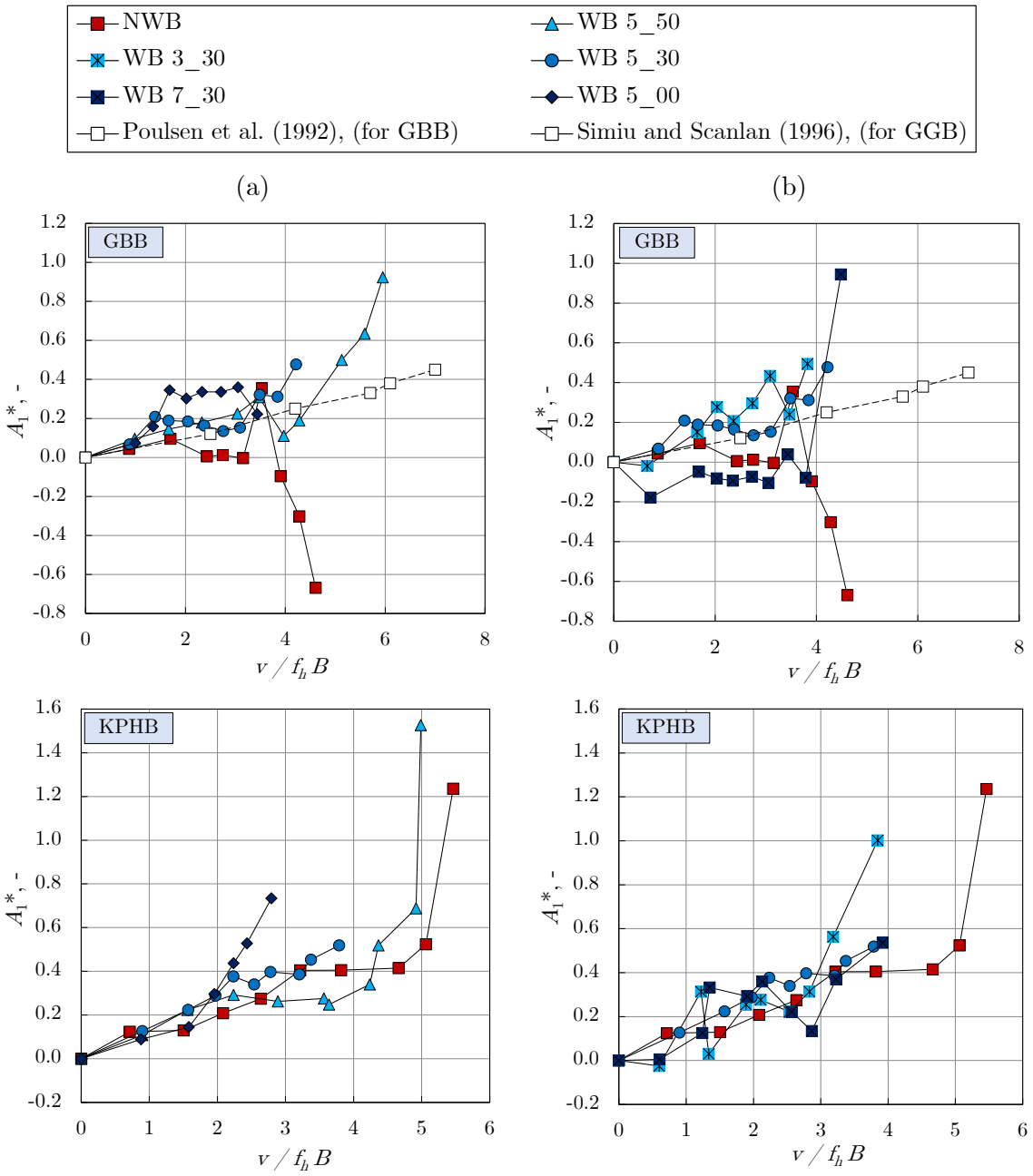

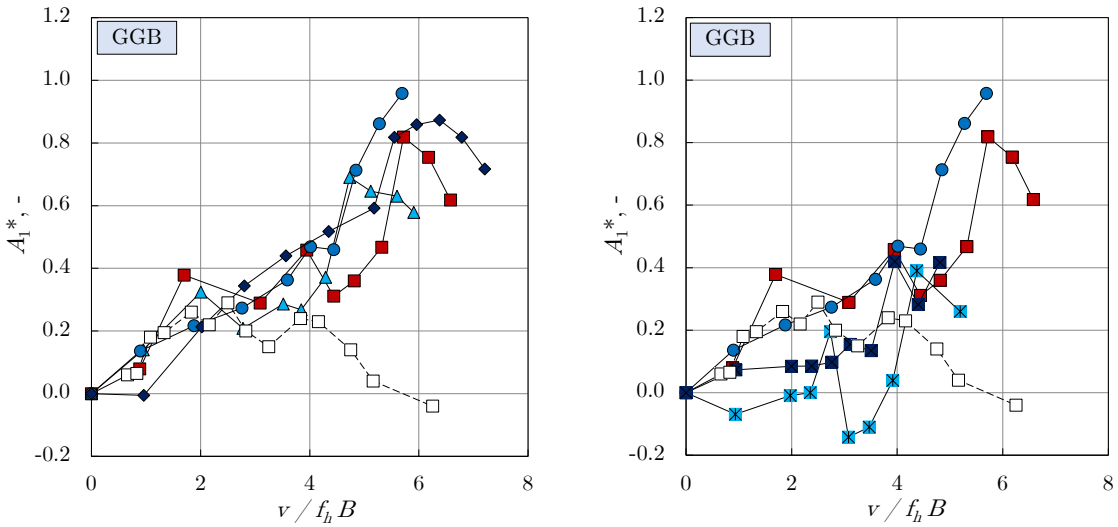

Figure 45: A_1^* FD for bridge-deck sections with: (i) 5 m high (full-scale) wind barriers of various porosities (0%, 30%, and 50%), (ii) 30% porous wind barriers of various full-scale heights (3 m, 5 m, and 7 m).

The indirect A_1^* FD addresses the influence of the heave motion on the self-excited pitch moment. For the Great Belt Bridge, wind barriers have nearly the same trend for all porosities. While these trends are similar to the results of the empty bridge-deck section, the discrepancies in those trends become significant at larger reduced flow velocities $v/f_hB > 4$. For the Kao-Pin Hsi Bridge, it is important to observe a sudden gradient for the solid wind barrier (WB 5_00) at $v/f_hB > 2$. For the Golden Gate Bridge, the results are similar for the empty bridge-deck section and the bridge-deck sections with all studied wind-barrier porosities.

The increasing wind-barrier height does not yield unambiguous systematic changes in the A_1^* trends for any of the studied bridge-deck sections. Nevertheless, there is a sudden increase in A_1^* for the Great Belt Bridge with the highest wind barrier (WB 7_30).

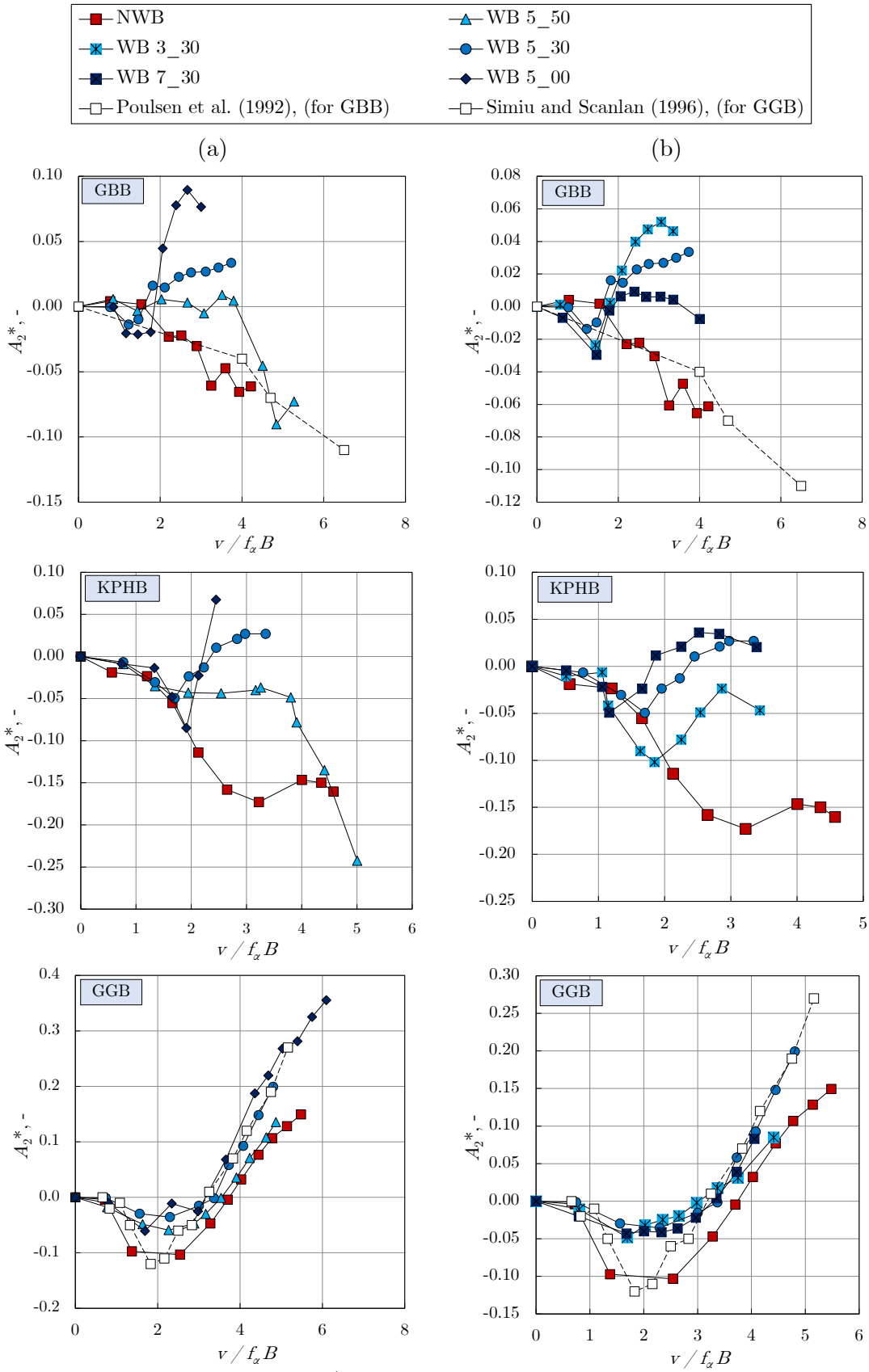

Figure 46: A_2^* FD for bridge-deck sections with:

(a) 5 m high (full-scale) wind barriers of various porosities (0%, 30%, and 50%), (b) 30% porous wind barriers of various full-scale heights (3 m, 5 m, and 7 m).

The A_2^* FD is commonly considered as the most important in the analysis of the bridge-deck dynamic stability. It addresses the influence of the pitch motion frequency on the self-excited pitch moment. A_2^* is related to damping in the pitch motion and is particularly important for the torsional flutter analysis. A_2^* has positive values for the negative aerodynamic damping, which decreases the overall damping of the system and may cause the negative overall damping of the system. In case of the negative overall damping, the divergent oscillations in the torsional direction occur (torsional flutter) and the structure may collapse.

The observed A_2^* trends indicate that wind barriers deteriorate the dynamic stability in the torsional motion, as A_2^* becomes positive, which is particularly exhibited for less-porous wind barriers at larger reduced flow velocities. This indicates that reducing the wind-barrier porosity may trigger the torsional flutter and possibly a collapse of the bridge.

The trends in A_2^* for increasing the wind-barrier height are not the same for all studied bridge-deck sections, as they are combined influenced by the aerodynamic bridge-deck shape.

For the streamlined Great Belt Bridge, reducing the wind-barrier height enhances positive A_2^* values and thus deteriorates the dynamic stability in the torsional motion. For the Kao-Pin Hsi Bridge, increasing the wind-barrier height adversely enhances positive A_2^* values and thus deteriorates the bridge dynamic stability. For the bluff Golden Gate Bridge, increasing the wind-barrier height does not have strong influence on the A_2^* trends, as all the Golden Gate Bridge configurations are susceptible to torsional flutter.

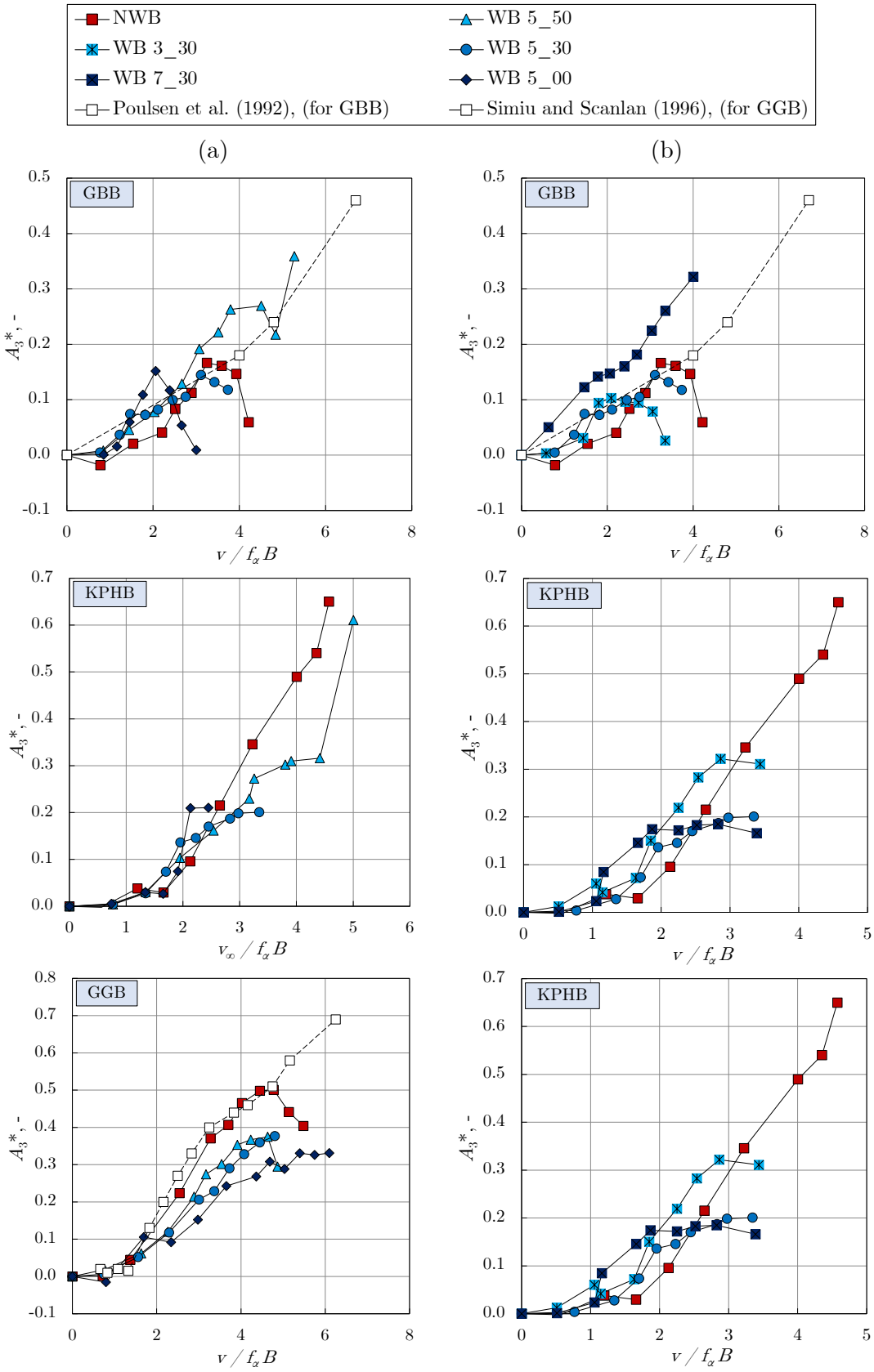

Figure 47: A_3^* FD for bridge-deck sections with:

(a) 5 m high (full-scale) wind barriers of various porosities (0%, 30%, and 50%), (b) 30% porous wind barriers of various full-scale heights (3 m, 5 m, and 7 m).

The direct A_3^* FD addresses the influence of the pitch displacement on the self-excited pitch moment. It is related to the damped frequency in the pitch motion.

A_3^* is generally positive for all studied configurations that suggests a decrease in the damped frequency of the pitch motion. The influence of wind barriers on A_3^* is different for various bridge-deck sections. For the Great Belt Bridge, there is a sudden drop in A_3^* at $v/f_\alpha B = 2$ in accordance with positive A_2^* values at those same reduced velocities. For the Kao-Pin Hsi Bridge, A_3^* is smaller in configurations with wind barriers as compared to the empty bridge-deck section. For the Golden Gate Bridge, there is a decrease in the pitch motion frequency that is less emphasized for less-porous wind barriers.

The influence of the wind-barrier height on the A_3^* trends is least exhibited for the Kao-Pin Hsi Bridge. The drop in A_3^* for the Great Belt Bridge is in accordance with A_2^* turning positive, as it occurs at $v/f_\alpha B = 3$ for WB 3_30. For the Golden Gate Bridge, there is a sudden drop in A_3^* for the WB 3_30 and WB 7_30 configurations.

The influence of the heave displacement on the self-excited pitch moment is rather unpredictable, hence A_4^* is sensitive to the input signal and often not analyzed, and therefore not reported here.

4.4.2. Effects of wind-barrier arrangement on flutter sensitivity of bridge-deck sections with wind barriers

The H_1^* FD for various arrangement of wind barriers is reported in Figure 48.

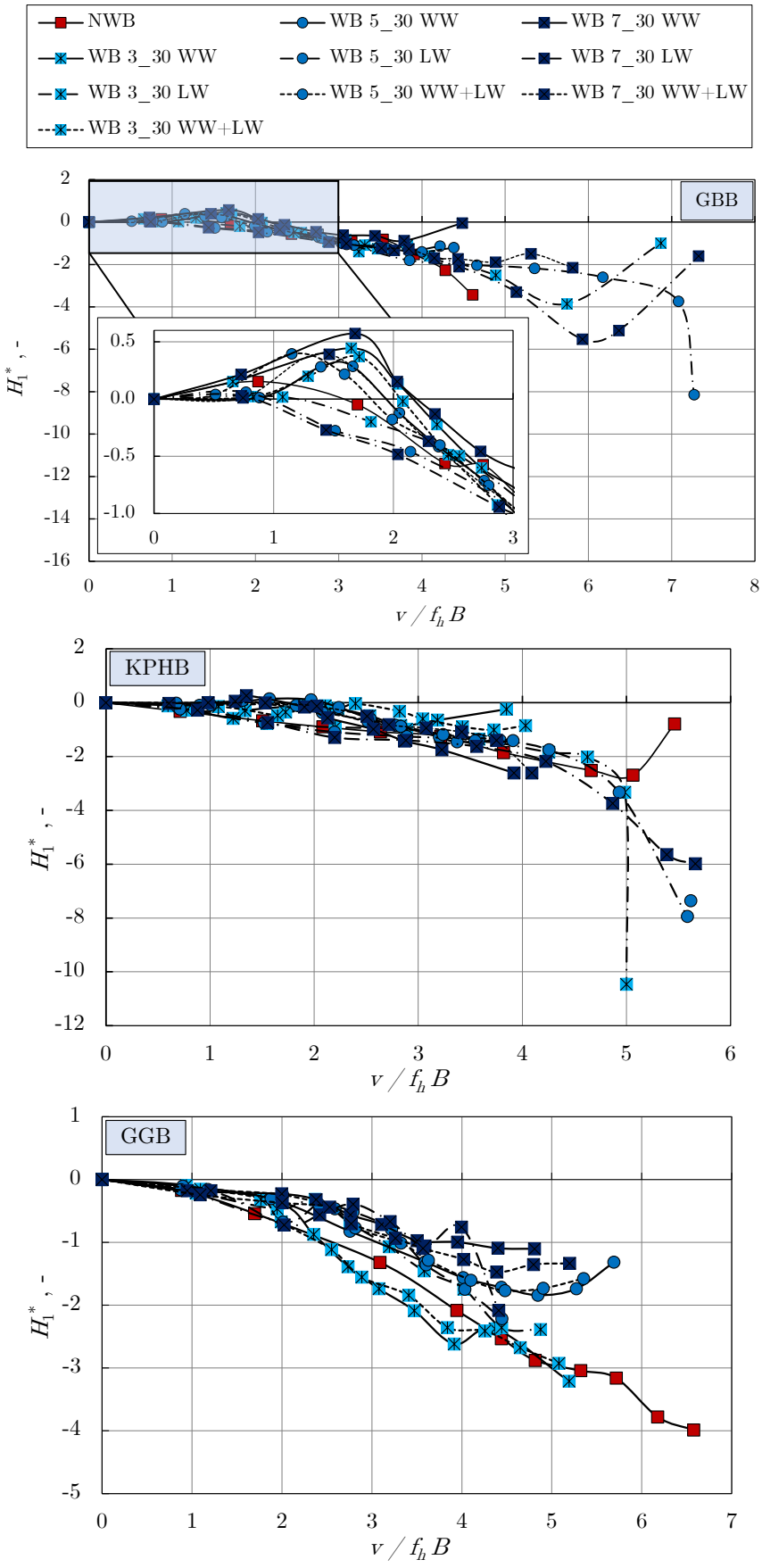

Figure 48: H_1^* FD for bridge-deck sections with various arrangements of wind barriers.

The H_1^* FD is negative for all wind-barrier arrangements at large reduced flow velocities. Positive H_1^* FD is observed for the Great Belt Bridge and the Kao-Pin Hsi Bridge for the windward and both windward and leeward wind barriers only in the range v/f_hB = 1-2. As the flow velocity increases, this phenomenon vanishes. A decrease in the generalized damping in the heave motion in the respective range of reduced flow velocities is reported in Figure 49 for the Great Belt Bridge at various arrangements of 5 m high (full-scale) wind barriers.

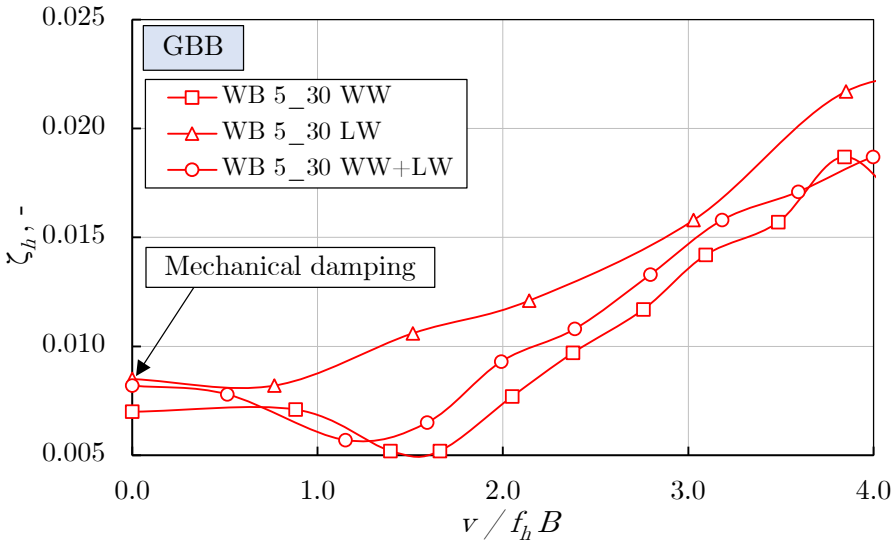

Figure 49: Generalized damping in the heave motion for the Great Belt Bridge and various arrangements of WB 5_30.

A decrease in the generalized damping that may be observed for the windward and both windward and leeward wind barriers, while it is not observed for the leeward wind barrier, is due to the vortex-shedding vibrations. Hence, the windward and both wind barriers may trigger vortex-induced-vibrations at relatively small reduced flow velocities, which may adversely decrease the lifetime of bridge structural components, e.g. Ehsan and Scanlan (1990), Wu and Kareem (2012).

When compared to the results obtained for the empty bridge-deck sections, the leeward wind barrier generally contributes to the negative H_2^* FD, while the windward and both windward and leeward wind barriers contribute to the positive H_2^* FD. The obtained results suggest a rather small influence of the wind-barrier layout on the H_3^* trends. H_2^* and H_3^* FDs are not shown in diagrams.

The windward and both windward and leeward wind barriers proved to deteriorate the most the dynamic stability in the pitch motion, as A_2^* is positive at the smallest reduced flow velocities in those configurations, Figure 50.

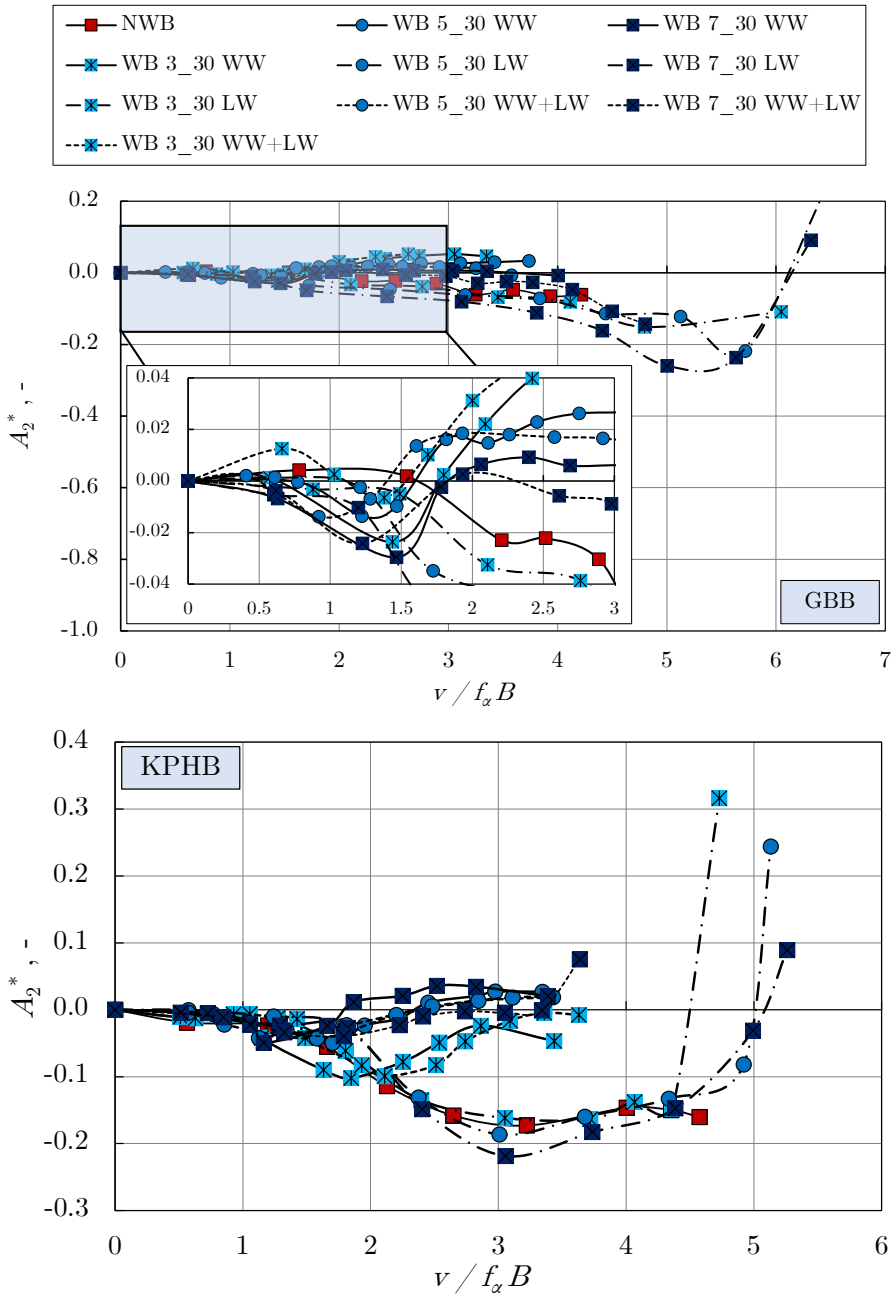

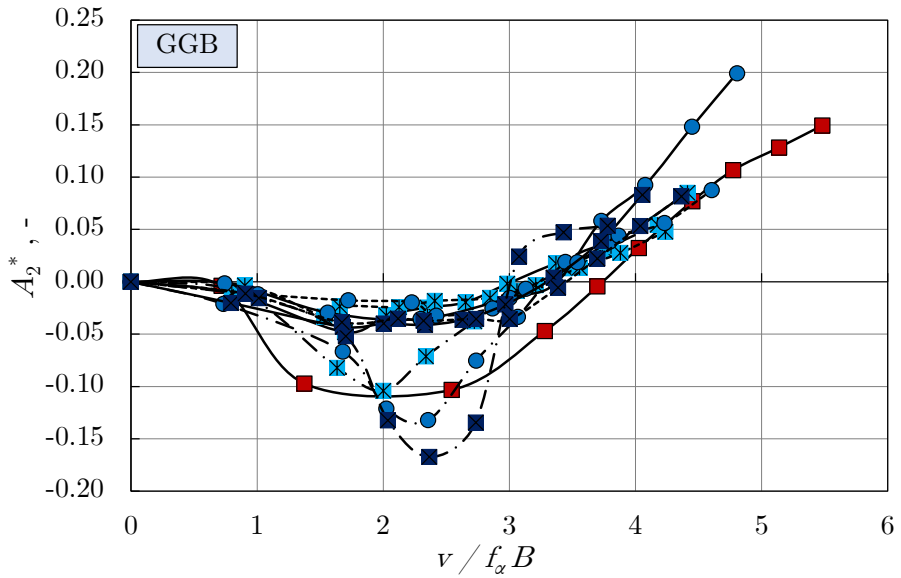

Figure 50: A_2^* FD for bridge-deck sections with various arrangements of wind barriers.

The bridge-deck sections with the leeward wind barrier become dynamically unstable in the torsional motion only at larger reduced flow velocities; hence, the leeward wind-barrier layout proved to be relatively more dynamically stable. A_3^* is generally positive suggesting a decrease in the damped frequency of the pitch motion, Figure 51.

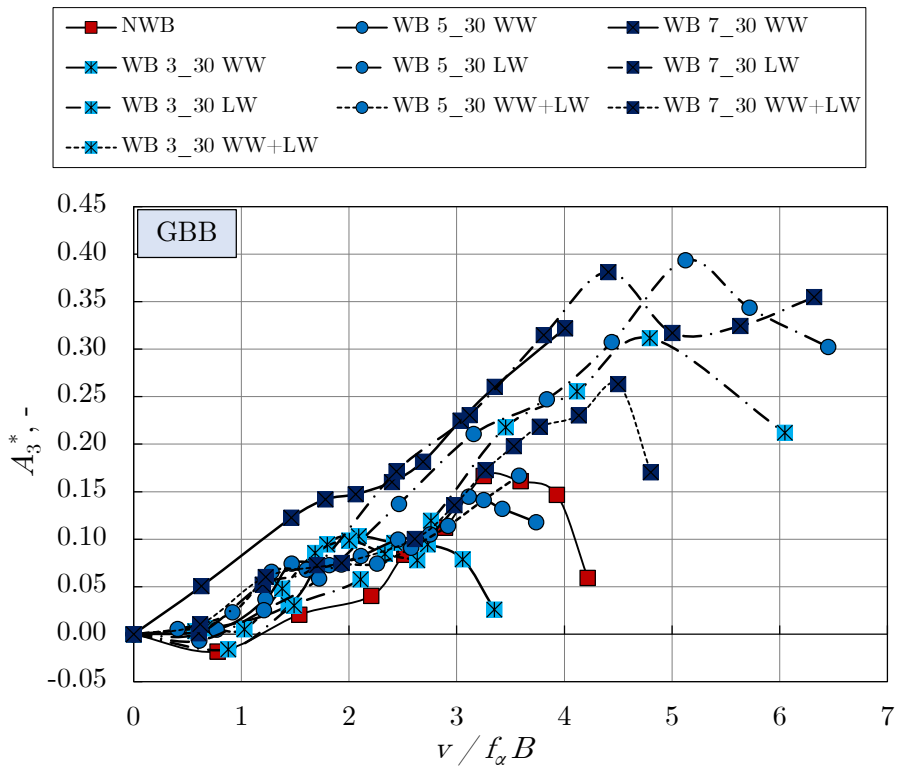

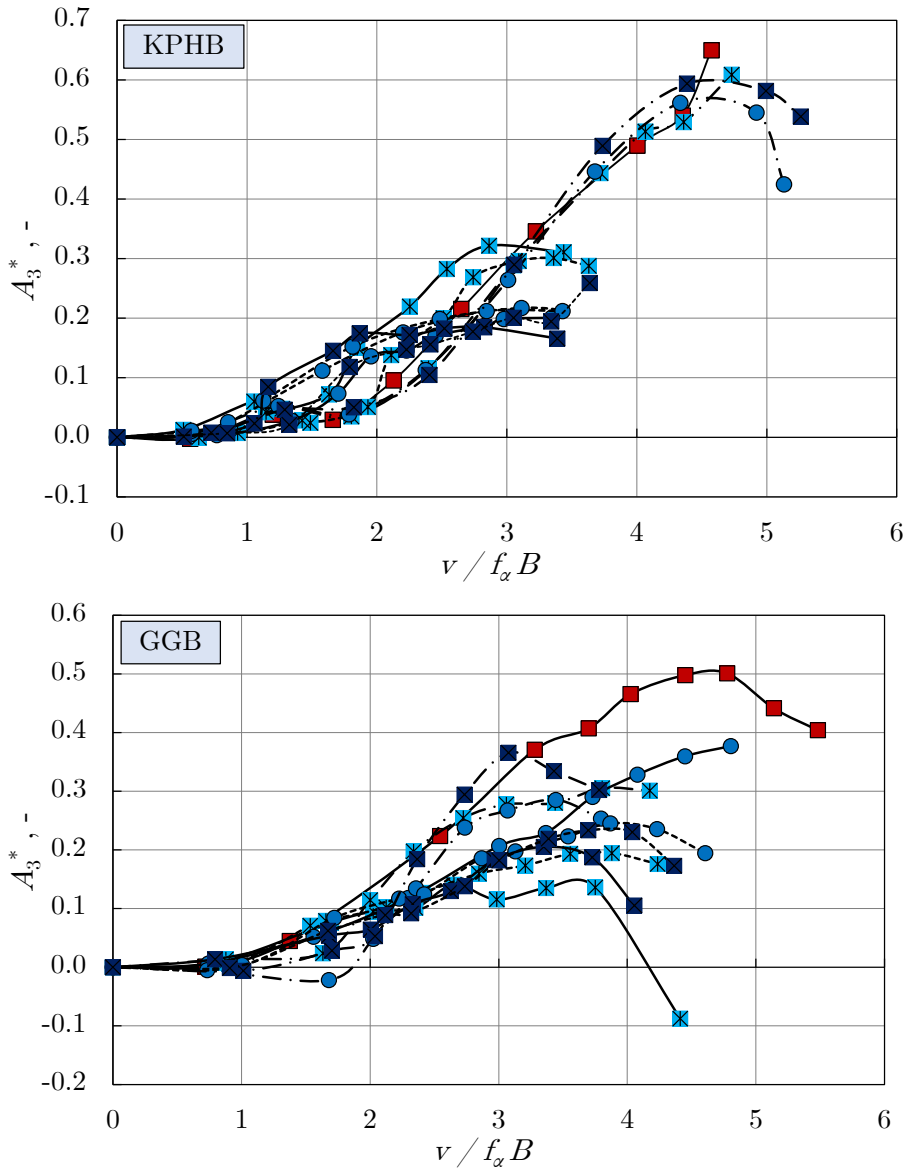

Figure 51: A_3^* FD for bridge-deck sections with various arrangements of wind barriers.

A shift in the trend of A_3^* suggests an instability in the pitch motion, which may be observed in agreement with the A_2^* behavior that is positive in the most of the studied configurations.

4.4.3. Critical flow velocity for bridge-deck flutter

The results for the critical flow velocity for the bridge-deck flutter based on the eigenvalue analysis are reported for wind barriers of various porosities and heights in Table 3 and Table 4, respectively.

Table 3: Critical flow velocities for flutter calculated using the eigenvalue analysis for bridge-deck section models with 5 m high (full-scale) wind barriers of various porosities (0%, 30%, and 50%).

	NWB	WB 5_50	WB 5_30	WB 5_00
GBB	v_{cr} = - m/s* f_{cr} = - Hz*	v_{cr} = 5.38 m/s f_{cr} = 3.27 Hz	v_{cr} = 3.37 m/s f_{cr} = 3.36 Hz	v_{cr} = 2.70 m/s f_{cr} = 3.63 Hz
KPHB	v_{cr} = 5.67 m/s f_{cr} = 3.07 Hz	v_{cr} = 5.29 m/s f_{cr} = 3.17 Hz	v_{cr} = 3.59 m/s f_{cr} = 3.27 Hz	v_{c} = 3.03 m/s f_{cr} = 3.27 Hz
GGB	v_{cr} = 4.58 m/s f_{cr} = 3.30 Hz	v_{cr} = 4.55 m/s f_{cr} = 3.34 Hz	v_{cr} = 4.13 m/s f_{cr} = 3.36 Hz	v_{cr} = 3.76 m/s f_{cr} = 3.39 Hz

*Aeroelastically stable in measured range of velocities.

Wind barriers generally cause the critical flow velocity for flutter to decrease, i.e. for the same bridge-deck section, flutter is expected to occur at smaller flow velocities when the wind barriers are in place in comparison with the empty bridge-deck sections without wind barriers.

The critical flow velocity for flutter decreases as the wind-barrier porosity decreases, i.e. as the wind barriers become more solid. The influence of wind barriers is more exhibited for the Great Belt Bridge and the Kao-Pin Hsi Bridge than it is the case for the Golden Gate Bridge.

These results complement well the trends observed for FDs and confirm that a decrease in the wind-barrier porosity deteriorates the dynamic stability of wide long-span cable-supported bridges.

Table 4: Critical flow velocities for flutter calculated using the eigenvalue analysis for bridge-deck section models with 30% porous wind barriers of various full-scale heights (3 m, 5 m, and 7 m).

	NWB	WB 3_30	WB 5_30	WB 7_30
GBB	v_{cr} = - m/s*	v_{cr} = 2.83 m/s	v_{cr} = 3.37 m/s	v_{cr} = 4.10 m/s
	f_{cr} = - Hz*	f_{cr} = 3.37 Hz	f_{cr} = 3.36 Hz	f_{cr} = 3.27 Hz
KPHB	v_{cr} = 5.67 m/s	v_{cr} = 3.90 m/s	v_{cr} = 3.59 m/s	v_{cr} = 3.04 m/s
	f_{cr} = 3.07 Hz	f_{cr} = 3.18 Hz	f_{cr} = 3.27 Hz	f_{cr} = 3.28 Hz
GGB	v_{cr} = 4.56 m/s	v_{cr} = 4.56 m/s	v_{cr} = 4.13 m/s	v_{cr} = 4.33 m/s
	f_{cr} = 3.30 Hz	f_{cr} = 3.45 Hz	f_{cr} = 3.36 Hz	f_{cr} = 3.41 Hz

*Aeroelastically stable in measured range of velocities.

The critical flow velocity for flutter is combined influenced by the increasing wind-barrier height and the aerodynamic bridge-deck shape. For the streamlined Great Belt Bridge, an increase in the wind-barrier height enhances the bridge dynamic stability, as the critical flow velocity for flutter increases when the wind-barrier height increases. For the semi-bluff Kao-Pin Hsi Bridge, increasing the wind-barrier height causes a decrease in the critical flow velocity for flutter. Increasing the wind-barrier height does not considerably influence the critical flutter velocity for the bluff Golden Gate Bridge.

5.2.1. *Critical flutter velocity for various wind-barrier arrangements*

The results for the critical flow velocity for flutter based on the eigenvalue analysis are reported in Figure 52 and Figure 53 for various arrangements of wind barriers.

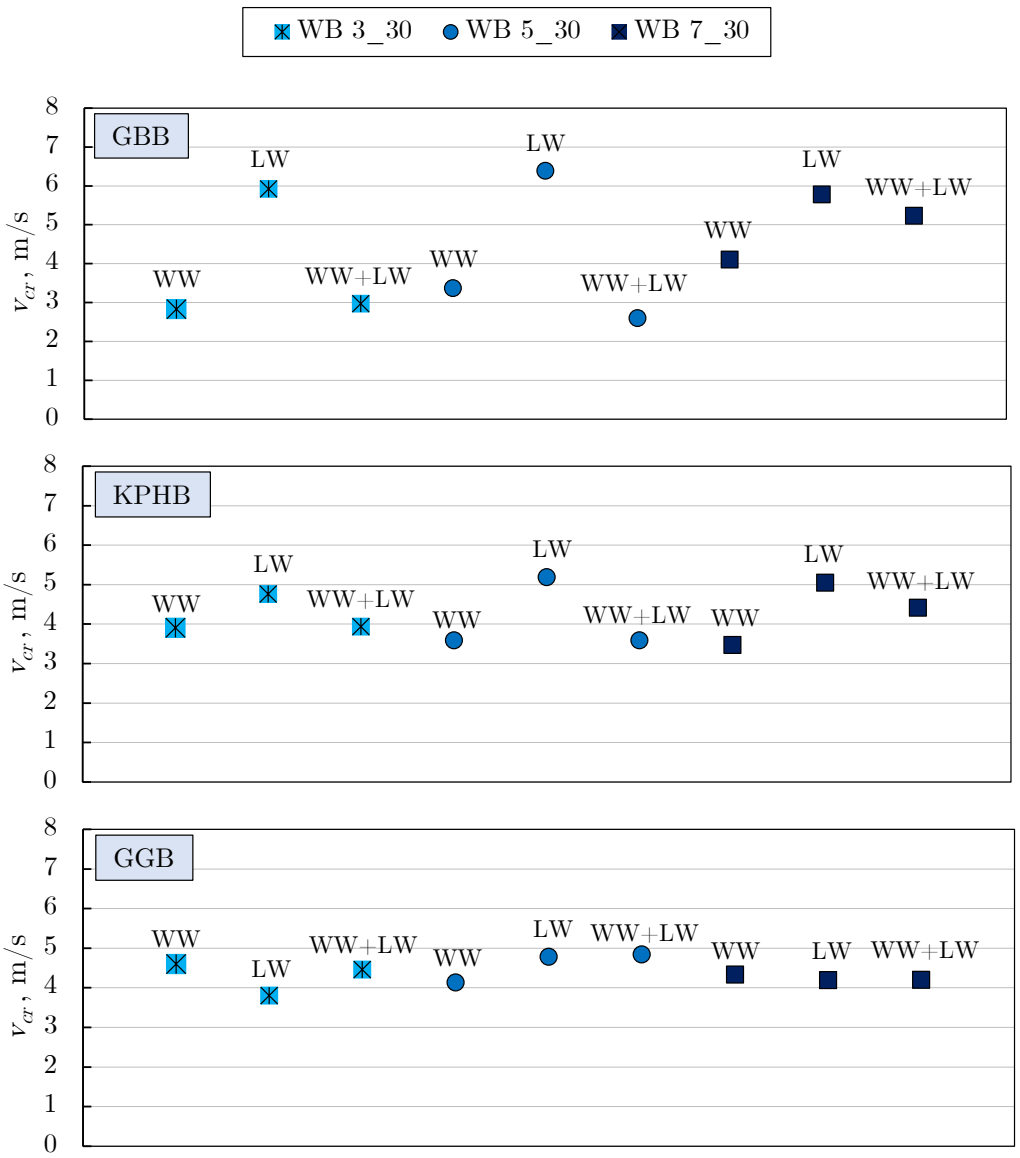

Figure 52: Critical flow velocity for flutter calculated using the eigenvalue analysis for bridge-deck section models and various arrangements of wind barriers.

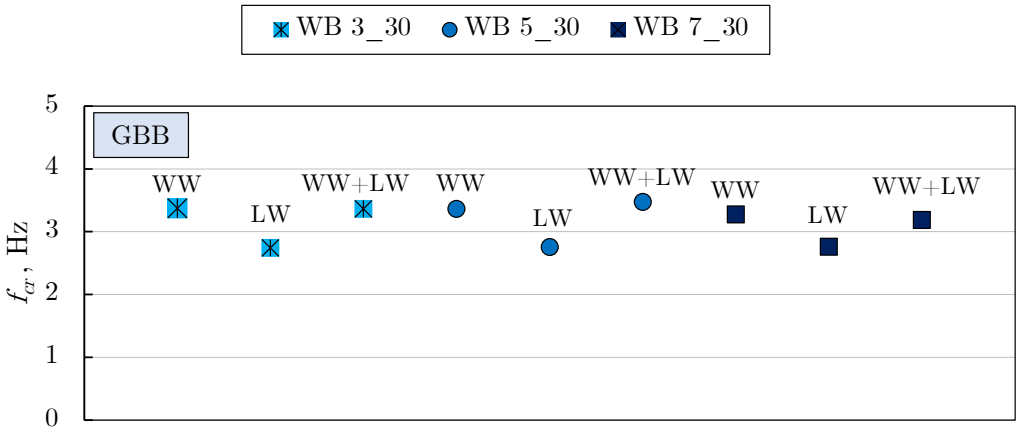

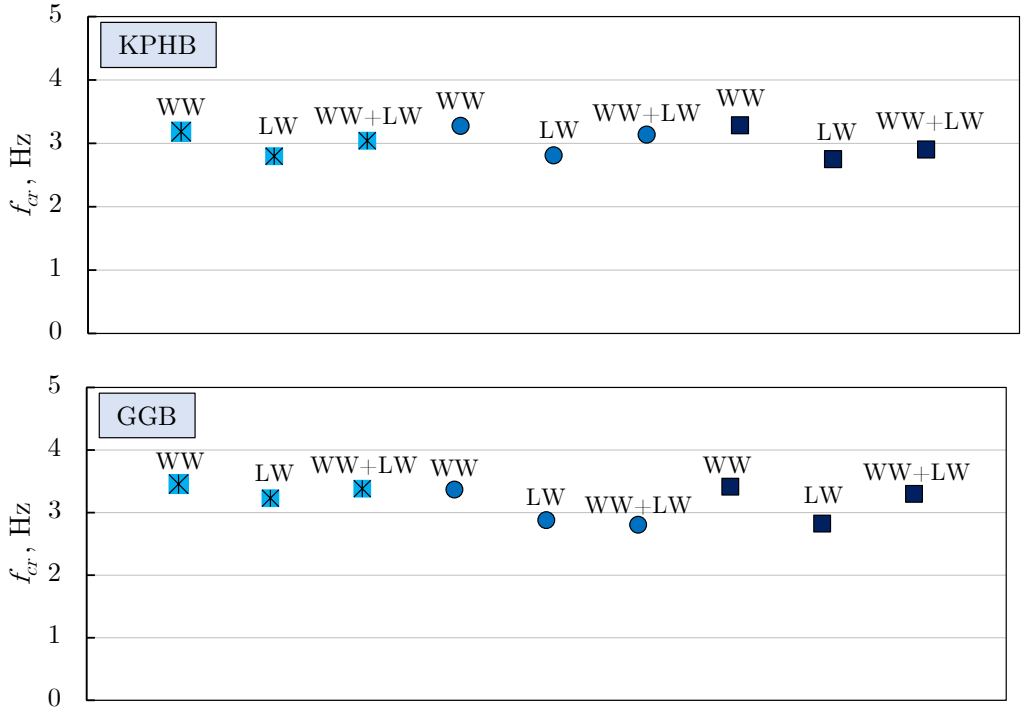

Figure 53: Frequency at critical flow velocity for flutter calculated using the eigenvalue analysis for bridge-deck section models and various arrangements of wind barriers.

The windward wind barrier as well as both windward and leeward wind barriers cause the critical flow velocity for flutter to significantly decrease and the reduced critical frequency to increase. Flutter is expected to occur at smaller flow velocities in those two configurations compared to the bridge-deck sections equipped with the leeward wind barrier only. The windward wind barrier and both windward and leeward wind barriers have approximately equal deteriorating influence on the dynamic stability of the studied bridge-deck sections. These trends are in agreement with the trends observed for FDs.

A percentagewise decrease of the critical flow velocity for flutter for the bridge-deck sections equipped with wind-barriers is reported in Figure 54 in comparison with the respective empty bridge-deck sections (without wind-barriers). These results are reported for Golden Gate and Kao-Pin Hsi bridge-deck sections, and not for Great Belt, because the empty Great Belt bridge-deck sections (without wind-barriers) remained stable with respect to flutter for all the tested flow velocities of our study, so it was not possible to conduct this comparison for Great Belt.

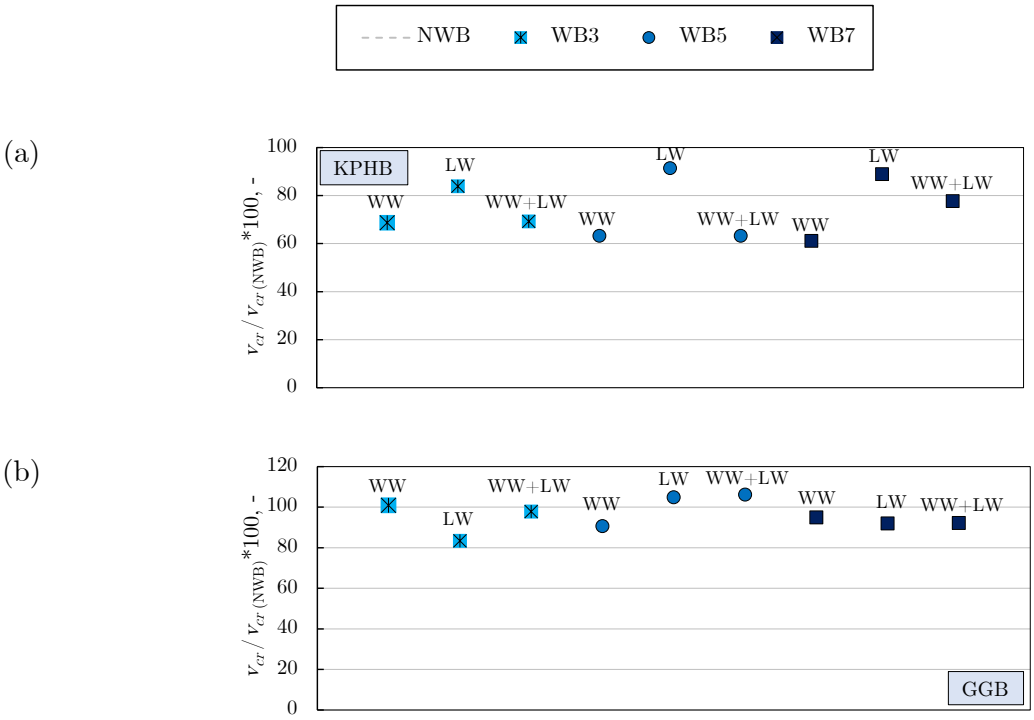

Figure 54: Percentagewise decrease of the critical flow velocity for flutter for the Kao-Pin Hsi and Golden Gate Bridge deck sections when the wind-barriers are in place with respect to the empty bridge-deck sections (without wind-barriers).

The results show that the critical flow velocity for flutter may be decreased up to 40% in case the windward wind barrier and both wind barriers are placed on bridge decks. For the bluff Golden Gate deck section, the critical flow velocity for flutter remained approximately the same in all configurations.

As an example, the diagrams of the numerical solution of the flutter 2DOF equation are provided in Figure 55 for the empty Great Belt Bridge section as well as for various configurations of the 5 m high (full-scale) wind barrier. The intersection of two solutions gives a value of the nondimensional critical flutter frequency K.

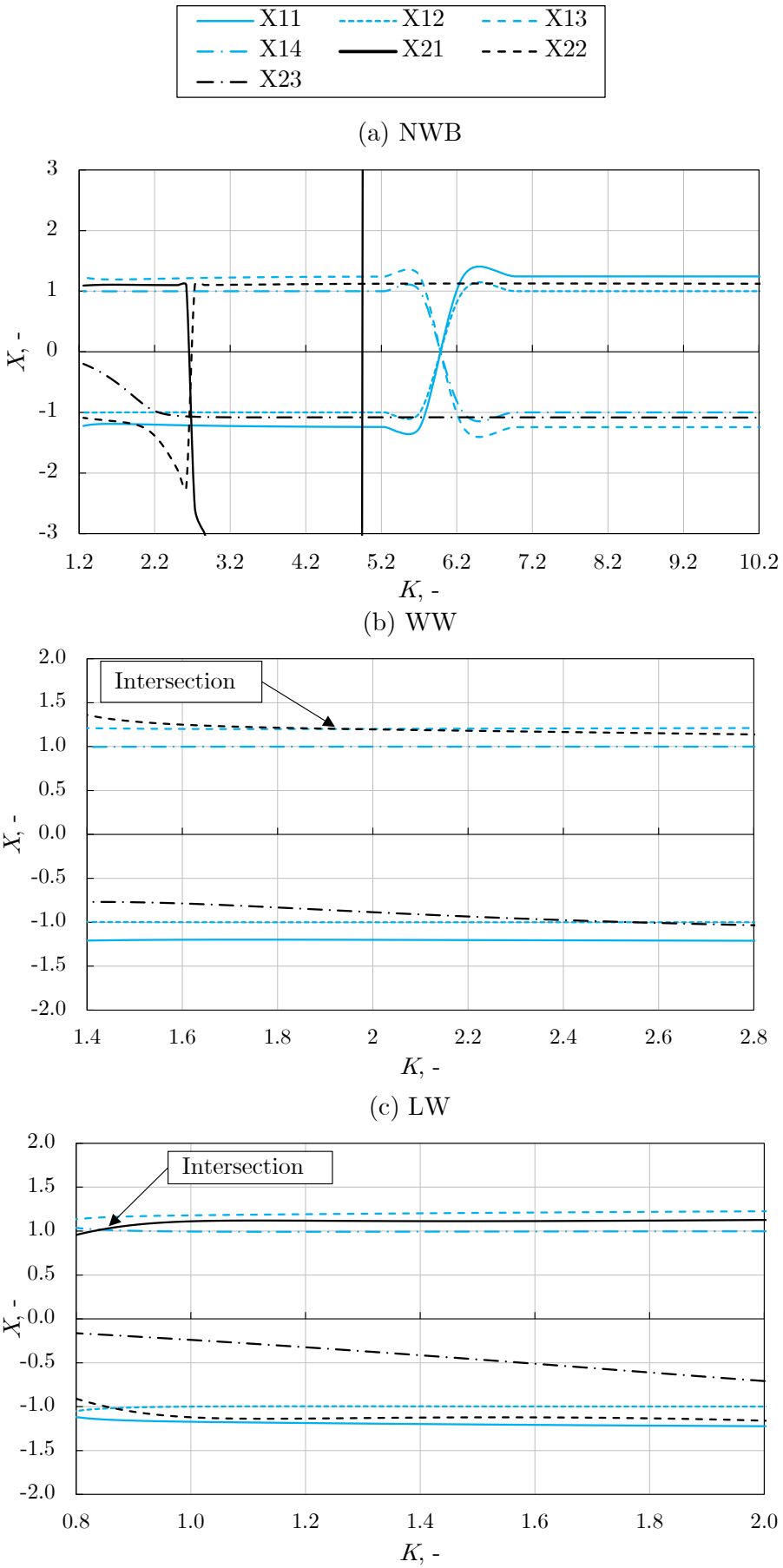

(a) NWB

(b) WW

(c) LW

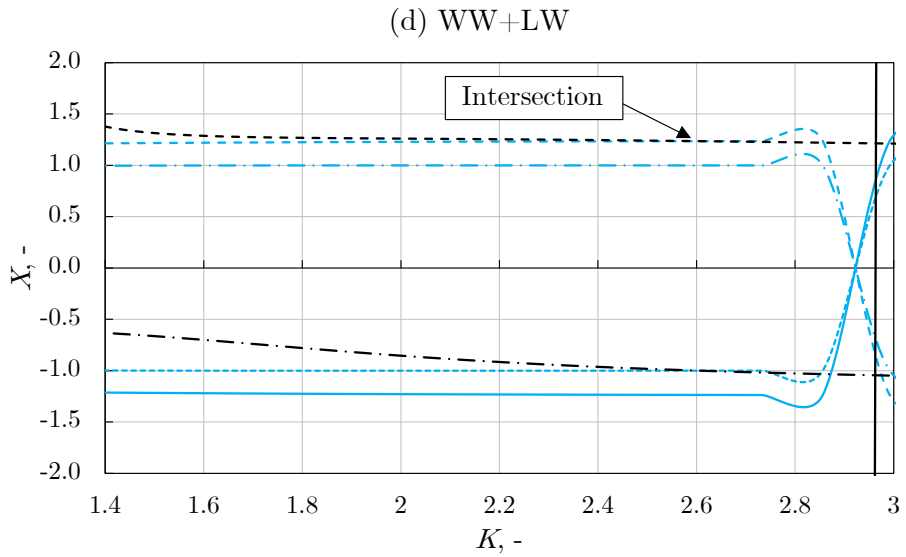

Figure 55: Numerical solutions of the 2DOF flutter equation for the Great Belt Bridge and various configurations of the 5 m high (full-scale) wind barrier.

4.4.4. Effects of incident flow turbulence on flutter sensitivity of bridge-deck sections with wind barriers

The direct H_1^* and A_2^* FDs (the most important FDs for the bridge dynamic stability) are reported in Figure 56.

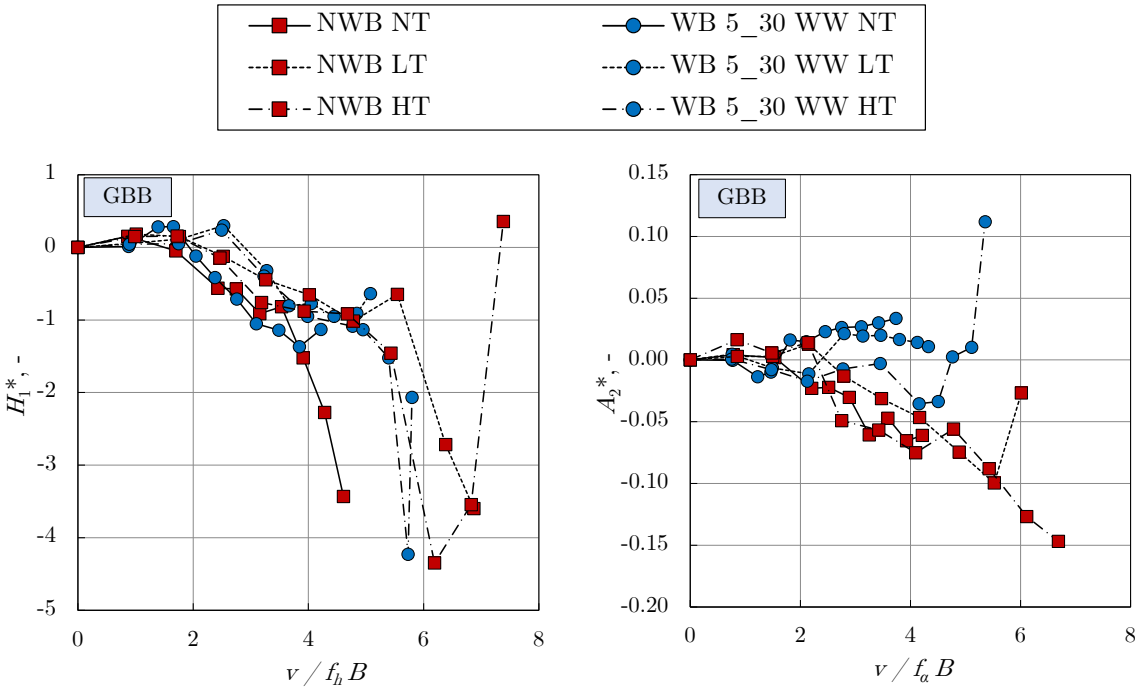

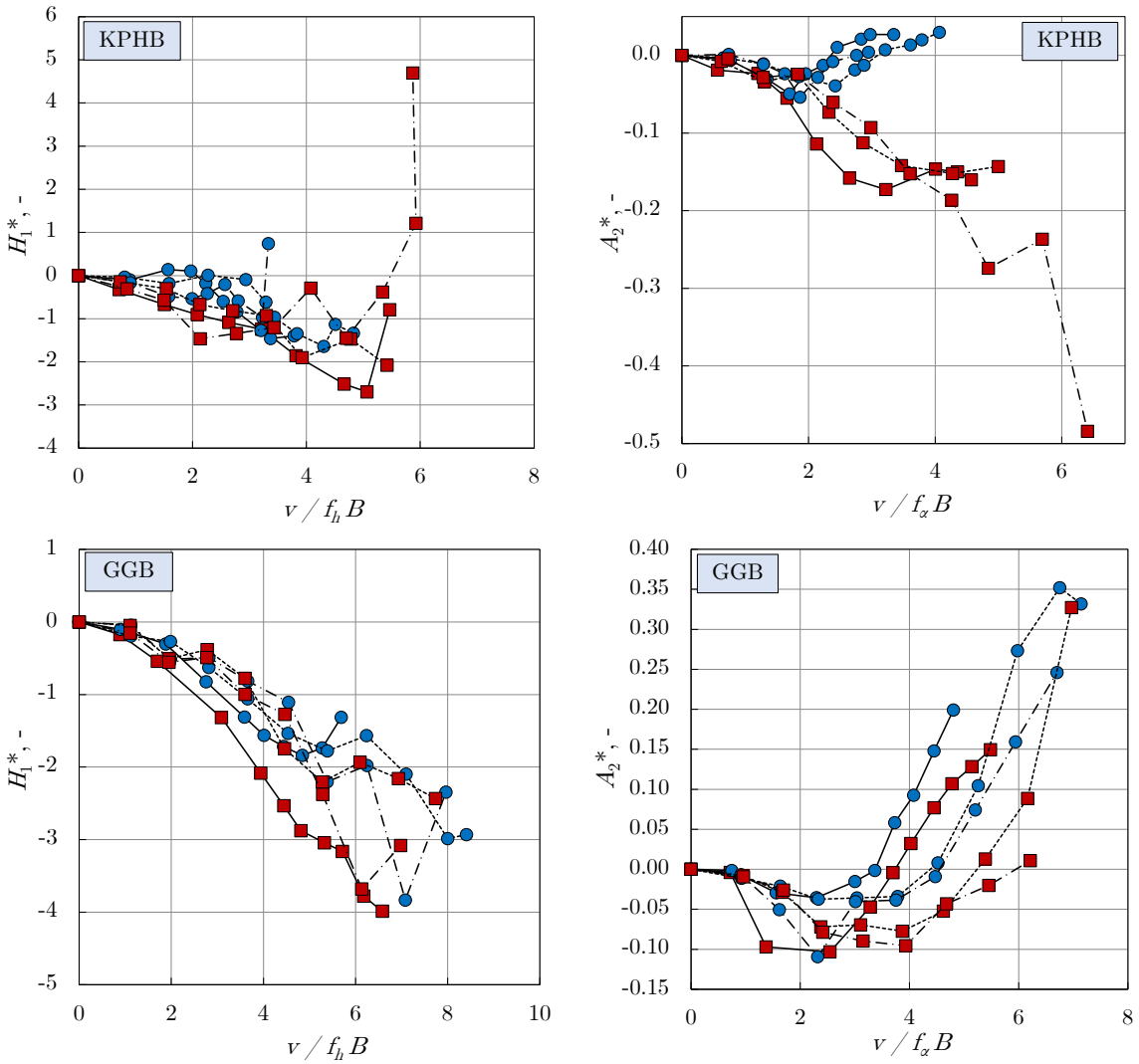

Figure 56: H_1^* and A_2^* FDs for three different turbulence intensities of the freestream flow.

The results for the H_1^* and A_2^* FDs indicate that the turbulence of the freestream flow may have an influence on the flutter susceptibility of cable-supported bridges equipped with wind barriers.

For all three studied bridge-deck section models and the 5_30 windward wind barrier, increasing the turbulence intensity of the freestream flow shifts the positive A_2^* to larger reduced flow velocities. Hence, the turbulence intensity of the freestream flow increases the dynamic stability of bridge decks with wind barriers with respect to the torsional flutter. A_2^* of the empty Great Belt Bridge (streamlined section) and the Kao-Pin Hsi Bridge (semi-bluff section) does not exhibit any particular influence of the turbulence.

The empty Golden Gate Bridge deck, which is bluff even without the wind barrier, experiences a similar influence of the freestream turbulence as A_2^* as well as this bridge-deck section with wind barriers.

The high turbulence intensity of the freestream flow may trigger the heave dynamic instability, as positive H_1^* is observed at large reduced flow velocities for some of the studied configurations.

Conclusions

Contemporary cable-supported bridges are flexible slender structures characterized by relatively low natural frequency and low mechanical damping in the pitch and heave motions, which makes them susceptible to the wind-induced dynamic instability. On the other hand, strong cross-winds on bridges and viaducts may cause dynamic instabilities of vehicles and trains. To protect vehicles from those adverse cross-wind effects in harsh wind conditions, protective wind barriers are commonly placed on bridges. While these barriers proved to be successful in sheltering vehicles and trains from cross-winds, their influence on aerodynamic and aeroelastic characteristics of bridges was previously not analyzed in detail.

The present thesis thus focuses on the effects of roadway wind barriers on aerodynamic characteristics of typical long-span cable-supported bridge decks and their sensitivity to self-excited vibrations. This work was conducted experimentally on the small-scale models in the climatic boundary-layer wind tunnel of the Institute of Theoretical and Applied Mechanics in Prague, Czech Republic. Three bridge-deck sections were studied, (i) streamlined Great Belt Bridge (Denmark), (ii) semi-bluff Kao-Pin Hsi Bridge (Taiwan), (iii) bluff Golden Gate Bridge (USA). Wind barriers of different porosities and heights placed on those bridge-deck sections were studied in various arrangements, i.e. (i) wind barrier at the windward bridge-deck edge only, (ii) wind barrier at the leeward bridge-deck edge only, (iii) wind barrier at both windward and leeward bridge-deck edges.

The analyzed parameters include the aerodynamic force and moment coefficients at various flow incidence angles, the quasi-steady Glauert-Den Hartog criterion for the galloping instability, aeroelastic flutter derivatives, eigenvalue analysis of the flutter instability, and flow characteristics around bridge-deck sections.

Major findings:

- Wind barriers negligibly influence a susceptibility of bridge decks to galloping, i.e. the galloping stability of cable-supported bridges is nearly the same for (a) empty bridge decks without wind barriers and (b) bridge decks equipped with wind barriers;
- The dynamic stability of cable-supported bridges with respect to torsional flutter is substantially deteriorated when wind barriers are placed on bridge decks, which trend

is particularly exhibited for more streamlined bridge decks, whereas bridge decks are more resilient to flutter at larger wind turbulence;

- Wind barriers may trigger vortex-induced vibrations of bridge decks.

Detailed summary of the obtained results:

For the single windward wind barrier, the drag force coefficient of bridge decks increases as the porosity of the wind barrier decreases, and as the height of the wind barrier increases. While this trend is observed for all studied bridge-deck sections, for all of them it is more exhibited at positive flow incidence angles (bridge deck rotated clockwise). The influence of wind barriers on the increase of the drag force coefficient is more exhibited for more streamlined bridge-deck sections. Wind barriers change the trends and absolute values of the lift force coefficient, which characteristic is more exhibited for more solid and higher wind barriers. The pitch moment decreases when the wind barriers are in place, while the influence of the porosity is more dominant than the wind-barrier height.

The arrangement of wind barriers on the bridge-deck sections strongly influences the aerodynamic drag and lift force coefficients. In the proximity of the zero flow incidence angle, all wind-barrier arrangements contribute to the negative lift force, i.e. downforce. For some configurations, due to a presence of wind barriers, the direction of the lift force changes from positive to negative, which is particularly exhibited for the leeward wind barrier. The wind-barrier arrangement does not significantly influence the pitch moment coefficient. Hence, the orientation and placement of wind barriers does not affect the torsional divergence (static aeroelastic phenomenon) of the bridge-deck sections.

Wind barriers in various heights, porosities and arrangements do not adversely affect the galloping sensitivity of bridges, as their galloping stability is achieved in all experiments both in the steady-state approach and dynamic tests. However, a switch from the positive to negative values (and vice versa) of the lift force coefficient gradient that is observed for some configurations may indicate possible critical points for the dynamic stability in the heave motion.

The windward wind barrier makes long-span cable-supported bridges more susceptible to torsional flutter. This is more pronounced for less-porous, i.e. more solid, wind barriers, while the effects of increasing the wind-barrier height are simultaneously influenced by the aerodynamic shape of bridge decks. The streamlined bridge-deck sections are generally more

sensitive to torsional flutter for smaller wind barriers, while the bluff sections are more prone to torsional flutter when designed with higher wind barriers.

From the wind-barrier arrangement point of view, the windward wind barrier and both windward and leeward wind barriers substantially deteriorate the torsional flutter stability of bridge-deck sections, while the influence of the leeward wind barrier on flutter stability of the bridge-deck sections is relatively minor. The windward and both windward and leeward wind barriers may trigger vortex-induced vibrations at relatively low reduced flow velocities, which may adversely shorten the lifetime of bridge structural components. The results of the eigenvalue analysis for the critical flutter flow velocity generally complement well the observed trends in the flutter derivatives.

The mean flow velocities are significantly reduced downstream of wind barriers thus indicating their sheltering effect in agreement with previous studies, while the windward and both windward and leeward wind barriers yield relatively similar fields of the mean flow velocity. The largest flow velocity variance is observed in the shear layer separated from the top of the windward wind barrier. Characteristics of the shear layer determine the fluctuations in the pressure distribution on the top surface of the bridge-deck sections, which may have an important role on the self-excited lift force and the pitch moment, and consequently the dynamic behavior of bridge-deck sections.

The research objectives set for this thesis are achieved and the research hypotheses are satisfied. While wind barriers successfully shelter the vehicles on bridges from cross winds, they proved to deteriorate aerodynamic stability of bridges. Future work on this topic would need to address the optimization of the wind-barrier shape to further enhance its sheltering effects for vehicles and at the same time retain the aerodynamic stability of bridges. This would potentially require using the movable elements of wind barriers, so the porosity of wind barriers may change depending on wind conditions. An influence of stationary and moving vehicles on aerodynamic and aeroelastic characteristics of cable-supported bridges equipped with wind barriers is still not investigated, nor the influence of transient winds, i.e. bora, hurricane, tornado, downburst.

References

[1] T. Miyata, "Historical view of long-span bridge aerodynamics," *J. Wind Eng. Ind. Aerodyn.*, vol. 91, no. 12–15, pp. 1393–1410, 2003.

[2] M. O. L. Hansen, J. N. Sorensen, S. Voutsinas, N. Sorensen, and H. A. Madsen, "State of the art in wind turbine aerodynamics and aeroelasticity," *Prog. Aerosp. Sci.*, vol. 42, no. 4, pp. 285–330, 2006.

[3] W. Shyy *et al.*, "Recent progress in flapping wing aerodynamics and aeroelasticity," *Prog. Aerosp. Sci.*, vol. 47, no. 7, pp. 284–327, 2010.

[4] A. Kareem and T. Wu, "Wind-induced effects on bluff bodies in turbulent flows: Nonstationary, non-Gaussian and nonlinear features," *J. Wind Eng. Ind. Aerodyn.*, vol. 122, pp. 21–37, 2013.

[5] N. Yoon, C. Chung, Y. H. Na, and S. Shin, "Control reversal and torsional divergence analysis for a high-aspect-ratio wing," *J. Mech. Sci. Technol.*, vol. 26, no. 12, pp. 3921–3931, 2012.

[6] Z. T. Zhang, Y. J. Ge, and Y. X. Yang, "Torsional stiffness degradation and aerostatic divergence of suspension bridge decks," *J. Fluids Struct.*, vol. 40, pp. 269–283, 2013.

[7] A. Larsen, "Aerodynamic aspects of the final design of the 1624 m suspension bridge across the Great Belt," *J. Wind Eng. Ind. Aerodyn.*, vol. 48, no. 2–3, pp. 261–285, 1993.

[8] M. Matsumoto, "Vortex shedding of bluff bodies: A review," *J. Fluids Struct.*, vol. 13, no. 7–8, pp. 791–811, 1999.

[9] G. Diana, F. Resta, M. Belloli, and D. Rocchi, "On the vortex shedding forcing on suspension bridge deck," *J. Wind Eng. Ind. Aerodyn.*, vol. 94, no. 5, pp. 341–363, 2006.

[10] E. Simiu and R. H. Scanlan, *Wind Effects on Structures: Fundamentals and Applications to Design*. John Wiley & Sons, New York, USA, 1996.

[11] H. Ruscheweyh, M. Hortmanns, and C. Schnakenberg, "Vortex-excited vibrations and galloping of slender elements," *J. Wind Eng. Ind. Aerodyn.*, vol. 65, no. 1–3, pp. 347–352, 1996.

[12] L. Carassale, A. Freda, and M. Marre-Brunenghi, "Effects of free-stream turbulence and corner shape on the galloping instability of square cylinders," *J. Wind Eng. Ind. Aerodyn.*, vol. 123, pp. 274–280, 2013.

[13] C. Mannini, A. M. Marra, and G. Bartoli, "VIV-galloping instability of rectangular cylinders: Review and new experiments," *J. Wind Eng. Ind. Aerodyn.*, vol. 132, pp. 109–124, 2014.

[14] C. H. Nguyen, A. Freda, G. Solari, and F. Tubino, "Experimental investigation of the aeroelastic behavior of a complex prismatic element," *Wind Struct.*, vol. 20, no. 5, pp. 683–699, 2015.

[15] T. Argentini, S. Omarini, A. Zasso, and M. Petrangeli, "Aerodynamic tailoring of a bluff deck section subjected to inclined winds due to the complex orography of the construction site," in *XV Conference of the Italian Association for Wind Engineering In-Vento*, 2018.

[16] Y. L. Xu, *Wind Effects on Cable-Supported Bridges*. John Wiley & Sons Singapore Pte. Ltd., 2013.

[17] A. Larsen and G. L. Larose, "Dynamic wind effects on suspension and cable-stayed bridges," *J. Sound Vib.*, vol. 334, no. 1, pp. 2–28, 2015.

[18] A. Jain, N. P. Jones, and R. H. Scanlan, "Coupled Flutter and Buffeting Analysis of Long-Span Bridges," *J. Struct. Eng.*, vol. 122, no. 7, pp. 716–725, 1996.

[19] P. Dunn and J. Dugundji, "Nonlinear stall flutter and divergence analysis of cantilevered graphite/epoxy wings," *AIAA J.*, vol. 30, no. 1, pp. 153–162, 1992.

[20] M. Matsumoto, Y. Daito, F. Yoshizumi, Y. Ichikawa, and T. Yabutani, "Torsional flutter of bluff bodies," *J. Wind Eng. Ind. Aerodyn.*, vol. 67–71, pp. 871–882, 1997.

[21] R. H. Scanlan and J. J. Tomko, "Airfoil and bridge deck flutter derivatives," *J. Eng.*

Mech. Div., vol. 97, no. 6, pp. 1717–1737, 1971.

[22] M. Shinozuka, C.-B. Yun, and H. Imai, "Identification of Linear Structural Dynamic Systems," *J. Eng. Mech. Div.*, vol. 108, no. 6, pp. 1371–1390, 1982.

[23] H. Yamada, T. Miyata, and H. Ichikawa, "Measurement of Aerodynamic Coefficients by System identification methods," *J. Wind Eng. Ind. Aerodyn.*, vol. 42, no. 1–3, pp. 1255–1263, 1992.

[24] P. Sarkar, "New identification methods applied to the response of flexible bridges to wind," Johns Hopkins University, 1993.

[25] M. Gu, R. Zhang, and H. Xiang, "Identification of flutter derivatives of bridge decks," *J. Wind Eng. Ind. Aerodyn.*, vol. 84, no. 2, pp. 151–162, 2000.

[26] Q. Ding, Z. Y. Zhou, L. Zhu, and H. Xiang, "Identification of flutter derivatives of bridge decks with free vibration technique," *J. Wind Eng. Ind. Aerodyn.*, vol. 98, no. 12, pp. 911–918, 2010.

[27] M. Matsumoto, Y. Kobayashi, and H. Shirato, "The influence of aerodynamic derivatives on flutter," *J. Wind Eng. Ind. Aerodyn.*, vol. 60, pp. 227–239, 1996.

[28] M. Falco, A. Curami, and A. Zasso, "Nonlinear effects in sectional model aeroelastic parameters identification," *J. Wind Eng. Ind. Aerodyn.*, vol. 42, no. 1–3, pp. 1321–1332, 1992.

[29] T. Theodorsen, "General theory of aerodynamic instability and the mechanism of flutter," Langley Field, VA, 1935.

[30] J. Holmes, *Wind Loading of Structures*. Taylor & Francis, 2015.

[31] M. Gu, R. Zhang, and H. Xiang, "Parametric study on flutter derivatives of bridge decks," *Eng. Struct.*, vol. 23, no. 12, pp. 1607–1613, 2001.

[32] R. H. Scanlan and W.-H. Lin, "Effects of Turbulence on Bridge Flutter Derivatives," *J. Eng. Mech. Div.*, vol. 104, no. 4, pp. 719–733, 1978.

[33] P. Sarkar, N. P. Jones, and R. H. Scanlan, "Identification of Aeroelastic Parameters of

Flexible Bridges," *J. Eng. Mech.*, vol. 120, no. 8, pp. 1718–1742, 1994.

[34] J. D. Raggett, "Wind study Golden Gate Bridge," Golden Gate Bridge, Highway and Transportation District, 2007.

[35] G. Diana, Y. Yamasaki, A. Larsen, D. Rocchi, S. Giappino, T. Argentini, A. Pagani, M. Villani, C. Somaschini, and M. Portentoso, "Construction stages of the long span suspension Izmit Bay Bridge: Wind tunnel test assessment," *J. Wind Eng. Ind. Aerodyn.*, vol. 123, pp. 300–310, 2013.

[36] F. Y. Xu, B. B. Li, C. S. Cai, and Z. Zhang, "Experimental Investigations on Aerostatic Characteristics of Bridge Decks under Various Conditions," *J. Bridg. Eng.*, vol. 19, no. 7, p. 04014024, 2014.

[37] F. Xu, L. Zhu, X. Ge, and Z. Zhang, "Some new insights into the identification of bridge deck flutter derivatives," *Eng. Struct.*, vol. 75, pp. 418–428, 2014.

[38] N. Nikitas, J. H. G. Macdonald, and J. B. Jakobsen, "Identification of flutter derivatives from full-scale ambient vibration measurements of the Clifton Suspension Bridge," *Wind Struct.*, vol. 14, no. 3, pp. 221–238, 2011.

[39] Y. Han, S. Liu, J. X. Hu, C. S. Cai, J. Zhang, and Z. Chen, "Experimental study on aerodynamic derivatives of a bridge cross-section under different traffic flows," *J. Wind Eng. Ind. Aerodyn.*, vol. 133, pp. 250–262, 2014.

[40] Y. Han, S. Liu, C. S. Cai, J. Zhang, S. Chen, and X. He, "The influence of vehicles on the flutter stability of a long-span suspension bridge," *Wind Struct.*, vol. 20, no. 2, pp. 275–292, 2015.

[41] S. Pospíšil, A. Buljac, H. Kozmar, S. Kuznetsov, M. Macháček, and R. Král, "Influence of Stationary Vehicles on Bridge Aerodynamic and Aeroelastic Coefficients," *J. Bridg. Eng.*, vol. 22, no. 4, 2017.

[42] H. Wang, T. Tao, R. Zhou, X. Hua, and A. Kareem, "Parameter sensitivity study on flutter stability of a long-span triple-tower suspension bridge," *J. Wind Eng. Ind. Aerodyn.*, vol. 128, pp. 12–21, 2014.

[43] A. Jain, N. P. Jones, and R. H. Scanlan, "Effect of modal damping on bridge aeroelasticity," *J. Wind Eng. Ind. Aerodyn.*, vol. 77–78, pp. 421–430, 1998.

[44] K. N. Bakis, D. J. N. Limebeer, M. S. Williams, and J. M. R. Graham, "Passive aeroelastic control of a suspension bridge during erection," *J. Fluids Struct.*, vol. 66, no. 543–570, 2016.

[45] F. Dorigatti, M. Sterling, D. Rocchi, M. Belloli, A. D. Quinn, C. J. Baker, and E. Ozkan, "Wind tunnel measurements of crosswind loads on high sided vehicles over long span bridges," *J. Wind Eng. Ind. Aerodyn.*, vol. 107–108, pp. 214–224, 2012.

[46] T. Argentini, E. Ozkan, D. Rocchi, L. Rosa, and A. Zasso, "Cross-wind effects on a vehicle crossing the wake of a bridge pylon," *J. Wind Eng. Ind. Aerodyn.*, vol. 99, no. 6–7, pp. 734–740, 2011.

[47] Y. Zhou and S. Chen, "Vehicle ride comfort analysis with whole-body vibration on long-span bridges subjected to crosswind," *J. Wind Eng. Ind. Aerodyn.*, vol. 155, pp. 126–140, 2016.

[48] N. Chen, Y. Li, B. Wang, Y. Su, and H. Xiang, "Effects of wind barrier on the safety of vehicles driven on bridges," *J. Wind Eng. Ind. Aerodyn.*, vol. 143, pp. 113–127, 2015.

[49] H. Kozmar, L. Procino, A. Borsani, and G. Bartoli, "Sheltering efficiency of wind barriers on bridges," *J. Wind Eng. Ind. Aerodyn.*, vol. 107–108, pp. 274–284, 2012.

[50] C. R. Chu, C. Y. Chang, C. J. Huang, T. R. Wu, C. Y. Wang, and M. Y. Liu, "Windbreak protection for road vehicles against crosswind," *J. Wind Eng. Ind. Aerodyn.*, vol. 116, pp. 61–69, 2013.

[51] M. Telenta, J. Duhovnik, F. Kosel, and V. Šajn, "Numerical and experimental study of the flow through a geometrically accurate porous wind barrier model," *J. Wind Eng. Ind. Aerodyn.*, vol. 124, pp. 99–108, 2014.

[52] H. Kozmar, L. Procino, A. Borsani, and G. Bartoli, "Optimizing height and porosity of roadway wind barriers for viaducts and bridges," *Eng. Struct.*, vol. 81, pp. 49–61,

2014.

[53] W. Guo, H. Xia, R. Karoumi, T. Zhang, and X. Li, "Aerodynamic effect of wind barriers and running safety of trains on high-speed railway bridges under cross winds," *Wind Struct.*, vol. 20, no. 2, pp. 213–236, 2015.

[54] M. Ogueta-Gutiérrez, S. Franchini, and G. Alonso, "Effects of bird protection barriers on the aerodynamic and aeroelastic behaviour of high speed train bridges," *Eng. Struct.*, vol. 81, pp. 22–34, 2014.

[55] N. P. Jones, R. H. Scanlan, P. P. Sarkar, and L. Singha, "The effect of section model details on aeroelastic parameters," *J. Wind Eng. Ind. Aerodyn.*, vol. 54–55, no. C, pp. 45–53, 1995.

[56] C. Mannini, G. Sbragi, and G. Schewe, "Analysis of self-excited forces for a box-girder bridge deck through unsteady RANS simulations," *J. Fluids Struct.*, vol. 63, pp. 57–76, 2016.

[57] S. Avila-Sanchez, O. Lopez-Garcia, A. Cuerva, and J. Meseguer, "Characterisation of cross-flow above a railway bridge equipped with solid windbreaks," *Eng. Struct.*, vol. 126, pp. 133–146, 2016.

[58] S. Laima, H. Li, W. Chen, and J. Ou, "Effects of attachments on aerodynamic characteristics and vortex-induced vibration of twin-box girder," *J. Fluids Struct.*, vol. 77, no. February, pp. 115–133, 2018.

[59] Y. Yang, R. Zhou, Y. Ge, and L. Zhang, "Experimental studies on VIV performance and countermeasures for twin-box girder bridges with various slot width ratios," *J. Fluids Struct.*, vol. 66, pp. 476–489, 2016.

[60] F. Y. Xu, B. Bin Li, C. L. Huang, and Z. Zhang, "Comparative Analysis on Aerostatic Coefficients of Bridge Deck Based on Wind Tunnel Test," *Appl. Mech. Mater.*, vol. 29–32, pp. 377–382, 2010.

[61] C. Dyrbye and S. O. Hansen, *Wind Loads on Structures*. Chichester, UK: John Wiley & Sons, 1996.

[62] J. Wu, Y. Zhou, and S. Chen, "Wind-induced performance of long-span bridge with modified cross-section profiles by stochastic traffic," *Eng. Struct.*, vol. 41, pp. 464–476, 2012.

[63] L. Singh, N. P. Jones, R. H. Scanlan, and O. Lorendeaux, "Identification of lateral flutter derivatives of bridge decks," *J. Wind Eng. Ind. Aerodyn.*, vol. 60, pp. 81–89, 1996.

[64] F. Y. Xu, X. Y. Ying, and Z. Zhang, "Three-Degree-of-Freedom Coupled Numerical Technique for Extracting 18 Aerodynamic Derivatives of Bridge Decks," *J. Struct. Eng.*, vol. 140, no. 11, pp. 1–13, 2014.

[65] F. Y. Xu, T. Wu, X. Y. Ying, and A. Kareem, "Higher-order Self-Excited Drag Forces on Bridge Decks," *J. Eng. Mech.*, vol. 142, no. 3, pp. 1–11, 2016.

[66] X. Zhang and J. M. W. Brownjohn, "Some considerations on the effects of the P-derivatives on bridge deck flutter," *J. Sound Vib.*, vol. 283, no. 3–5, pp. 957–969, 2005.

[67] F. Xu, "System Decoupling Approach for 3-DOF Bridge Flutter Analysis," *J. Struct. Eng.*, vol. 141, no. 7, pp. 1–12, 2015.

[68] A. Chen, X. He, and H. Xiang, "Identification of 18 flutter derivatives of bridge decks," *J. Wind Eng. Ind. Aerodyn.*, vol. 90, no. 12–15, pp. 2007–2022, 2002.

[69] G. Bartoli, S. Contri, C. Mannini, and M. Righi, "Toward an Improvement in the Identification of Bridge Deck Flutter Derivatives," *J. Eng. Mech.*, vol. 135, no. 8, pp. 772–785, 2009.

[70] R. Král, "Numerical and experimental solutions of self-induced instability of bridge girders," Institute of Theoretical and Applied Mechanics Prague, 2011.

[71] M. Plut, "Experiments on flow and turbulence in the climatic wind tunnel," University of Zagreb: Faculty of Mechanical Engineering and Naval Architecture, 2013.

[72] L. Bruno and G. Mancini, "Importance of deck details in bridge aerodynamics," *Struct. Eng. Int. J. Int. Assoc. Bridg. Struct. Eng.*, vol. 12, no. 4, pp. 289–294, 2002.

[73] R. H. Scanlan, "Some observations on the state of bluff-body aeroelasticity," *J. Wind Eng. Ind. Aerodyn.*, vol. 69–71, pp. 77–90, 1997.

[74] D. Allori, G. Bartoli, and C. Mannini, "Wind tunnel tests on macro-porous structural elements: A scaling procedure," *J. Wind Eng. Ind. Aerodyn.*, vol. 123, pp. 291–299, 2013.

[75] H. Kozmar, K. Butler, and A. Kareem, "Transient cross-wind aerodynamic loads on a generic vehicle due to bora gusts," *J. Wind Eng. Ind. Aerodyn.*, vol. 111, pp. 73–84, 2012.

[76] H. Kozmar, K. Butler, and A. Kareem, "Downslope Gusty Wind Loading of Vehicles on Bridges," *J. Bridg. Eng.*, vol. 20, no. 11, pp. 1–11, 2015.

[77] G. S. West and C. J. Apelt, "The effects of tunnel blockage and aspect ratio on the mean flow past a circular cylinder with Reynolds numbers between 104 and 105," *J. Fluid Mech.*, vol. 114, no. April, pp. 361–377, 1982.

[78] R. J. Adrian, "Particle-Imaging Techniques for Experimental Fluid Mechanics," *Annu. Rev. Fluid Mech.*, vol. 23, pp. 261–304, 1991.

[79] C. E. Willert and M. Gharib, "Digital particle image velocimetry," *Exp. Fluids*, vol. 10, no. 4, pp. 181–193, 1991.

[80] J. P. Den Hartog, "Transmission Line Vibration Due to Sleet," *Trans. Am. Inst. Electr. Eng.*, vol. 51, pp. 1074–1076, 1932.

[81] R. Král, S. Pospíšil, and J. Náprstek, "Experimental Set-Up for Advanced Aeroelastic Tests on Sectional Models," *Exp. Tech.*, vol. 40, no. 1, pp. 3–13, 2016.

[82] C. Mannini and G. Bartoli, "Aerodynamic uncertainty propagation in bridge flutter analysis," *Struct. Saf.*, vol. 52, no. PA, pp. 29–39, 2015.

[83] G. Diana, F. Resta, and D. Rocchi, "A new numerical approach to reproduce bridge aerodynamic non-linearities in time domain," *J. Wind Eng. Ind. Aerodyn.*, vol. 96, no. 10–11, pp. 1871–1884, 2008.

[84] M. Noda, H. Utsunomiya, F. Nagao, M. Kanda, and N. Shiraishi, "Effects of oscillation amplitude on aerodynamic derivatives," *J. Wind Eng. Ind. Aerodyn.*, vol. 91, no. 1–2, pp. 101–111, 2003.

[85] N. K. Poulsen, A. Damsgaard, and T. A. Reinhold, "Determination of flutter derivatives for the Great Belt Bridge," *J. Wind Eng. Ind. Aerodyn.*, vol. 41, no. 1–3, pp. 153–164, 1992.

[86] G. Diana, D. Rocchi, T. Argentini, and S. Muggiasca, "Aerodynamic instability of a bridge deck section model: Linear and nonlinear approach to force modelling," *J. Wind Eng. Ind. Aerodyn.*, vol. 98, no. 6–7, pp. 363–374, 2010.

[87] S. A. Coleman and C. J. Baker, "An experimental study of the aerodynamic behaviour of high sided lorries in cross winds," *J. Wind Eng. Ind. Aerodyn.*, vol. 53, no. 3, pp. 401–429, 1994.

[88] R. H. Reinhold, M. Brinch, and A. Damsgaard, "Wind tunnel tests for the Great Belt Link," in *Proceedings of the 1st International Symposium on Aerodynamics of Large Bridges*, 1992.

[89] A. Zanotti and G. Gibertini, "Experimental assessment of an active L-shaped tab for dynamic stall control," *J. Fluids Struct.*, vol. 77, pp. 151–169, 2018.

[90] D. W. Seo and L. Caracoglia, "Estimation of torsional-flutter probability in flexible bridges considering randomness in flutter derivatives," *Eng. Struct.*, vol. 33, no. 8, pp. 2284–2296, 2011.

[91] T. Canor, L. Caracoglia, and V. Denoël, "Application of random eigenvalue analysis to assess bridge flutter probability," *J. Wind Eng. Ind. Aerodyn.*, vol. 140, pp. 79–86, 2015.

[92] B. F. Ehsan and R. H. Scanlan, "Vortex induced vibrations of flexible bridges," *J. Eng. Mech.*, vol. 116, no. 6, pp. 1392–1411, 1990.

[93] T. Wu and A. Kareem, "An overview of vortex-induced vibration (VIV) of bridge decks," *Front. Struct. Civ. Eng.*, vol. 6, no. 4, pp. 335–347, 2012.

Curriculum vitae

Andrija Buljac was born in Sinj, Croatia on February 24th, 1991. He completed the elementary school in Hrvace, the secondary school in Sinj and enrolled at the Faculty of Mechanical Engineering and Naval Architecture, University of Zagreb in 2009. He completed the Engineering Modeling and Computer Simulations undergraduate program in 2013 Magna Cum Laude with the BSc thesis on computational fluid dynamics of car aerodynamics. In 2013, he enrolled in the Engineering Modeling and Computer Simulations graduate program of the Faculty of Mechanical Engineering and Naval Architecture, University of Zagreb. He graduated in 2014 Summa Cum Laude with the MSc thesis on the effects of vehicles on the dynamic stability of long-span cable-supported bridges and started his PhD studies in the same year. During his studies he was awarded with the Davorin Bazjanac award for the top undergraduate students, AMAC-UK academic award for the PhD students, the award of the Faculty of Mechanical Engineering and Naval Architecture, University of Zagreb for the best PhD student as well as numerous grants for research stays and scientific conferences. He published nine peer-reviewed journal articles and ten conference contributions.

Bibliography

A) Peer-reviewed journal papers

A1. Džijan I., Pašić A., Buljac A. and Kozmar H. (2019) Aerodynamic forces acting on a race car for various ground clearances and rake angles. Journal of Applied Fluid Mechanics 12 (2), 361-368.

A2. Majdandžić Lj., Buljić D., Buljac A. and Kozmar H. (2018) Aerodynamic design of a solar road vehicle. International Journal of Automotive Technology 19 (6), 949-957.

A3. Buljac A., Kozmar H., Pospišil S. and Machaček M. (2017) Flutter and galloping of cable-supported bridges with porous wind barriers. Journal of Wind Engineering and Industrial Aerodynamics 171, 304-318.

A4. Buljac A., Kozmar H., Pospišil S. and Machaček M. (2017) Aerodynamic and aeroelastic characteristics of typical bridge decks equipped with wind barriers at the windward bridge-deck edge. Engineering Structures 137, 310-322.

A5. Pospišil S., Buljac A., Kozmar H., Kuznetsov S., Machaček M. and Kral R. (2017) Influence of stationary vehicles on bridge aerodynamics and aeroelasticity. Journal of Bridge Engineering 22, 05016012-1-05016012-13.

A6. Pavlović B., Pavičević M., Buljac A., Džijan I. and Kozmar H. (2017) Design Curves for Gas Pressure Drop in Excess Flow Safety Valve. Journal of Pipeline Systems Engineering and Practice 8, 06017005-1-06017005-5.

A7. Buljac A., Džijan I., Korade I., Krizmanić S. and Kozmar H. (2016) Automobile aerodynamics influenced by airfoil-shaped rear wing. International Journal of Automotive Technology 17, 377-385.

A8. Buljac A., Kozmar H. and Džijan I. (2016) Aerodynamic characteristics of underbody and wings for a generic open-wheel race car. Transactions of Famena 40, 19-34.

A9. Buljac A., Pospišil S., Kozmar H., Kuznetsov S. and Kral R. (2016) Flutter derivatives of the Kao-Pin Hsi cable-supported bridge. Applied Mechanics and Materials 821, 172-179.

B) Conference papers

B1. Buljac A., Kozmar H., Yang W. and Kareem, A. (2019) Dynamic response of floating offshore wind turbines to concurrent wind, wave and currents action. The 15th International Conference on Wind Engineering, Beijing, China. Accepted for oral presentation.

B2. Buljac A., Kozmar H., Yang W. and Kareem, A. (2018) Wind, wave and sea current loads on offshore wind turbines. In-Vento 2018, XV Conference of the Italian Association for Wind Engineering, Naples, Italy.

B3. Buljac A., Kozmar H., Machaček M. and Pospišil S. (2018) Self-excited vibrations of a bridge deck with single and double wind barriers. XV Conference of the Italian Association for Wind Engineering, Naples, Italy.

B4. Buljac A., Kozmar H., Yang W. and Kareem, A. (2018) Experimental Study of Environmental Loads on a Monopole-supported Offshore Wind Turbine. 9th International Congress of Croatian Society of Mechanics, Split, Croatia.

B5. Džijan I., Pašić A., Buljac A. and Kozmar H. (2018) Computational modelling of aerodynamic loads on two race cars at various distances. International Symposium on Computational Wind Engineering, Seoul, South Korea.

B6. Buljac A., Kozmar H., Pospišil S. and Machaček M. (2017) Flutter and galloping of bridge decks with roadway wind barriers. 7th European-African Conference on Wind Engineering, Liege, Belgium.

B7. Buljac A., Kozmar H., Pospišil S., Machaček M. and Kral R. (2016) Dynamic stability of the Golden Gate Bridge deteriorated by roadway wind barriers. 8th International Colloquium on Bluff Body Aerodynamics and Applications, Boston, USA.

B8. Pospišil S., Buljac A., Kuznetsov S. and Kozmar H. (2015) Influence of vehicles on bridge flutter and galloping. Symposium on Progress in Wind Engineering and Structural Dynamics, Taipei, Taiwan.

B9. Buljac A., Pospišil S., Kozmar H., Kuznetsov S. and Kral R. (2015) Comparison of flutter derivatives for Kao-Pin Hsi Bridge and flat plate. 21st International Conference Engineering Mechanics, Svratka, Czech Republic.

B10. Buljac A., Pospišil S., Kozmar H., Kuznetsov S. and Kral R. (2015) Influence of vehicles on bridge aeroelastic stability. 8th International Congress of Croatian Society of Mechanics, Opatija, Croatia.

Appendix

Technical drawings

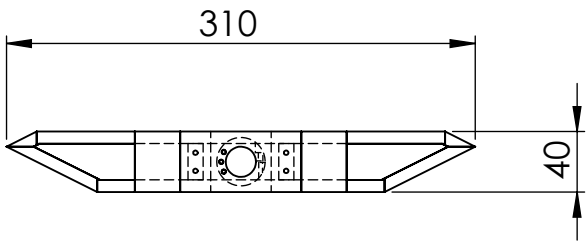

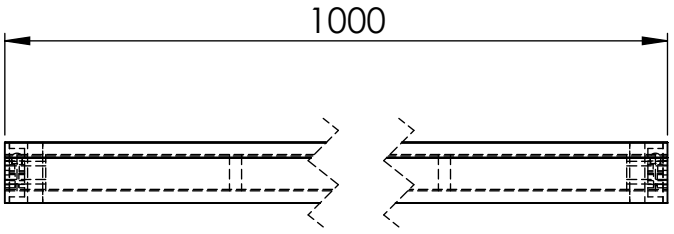

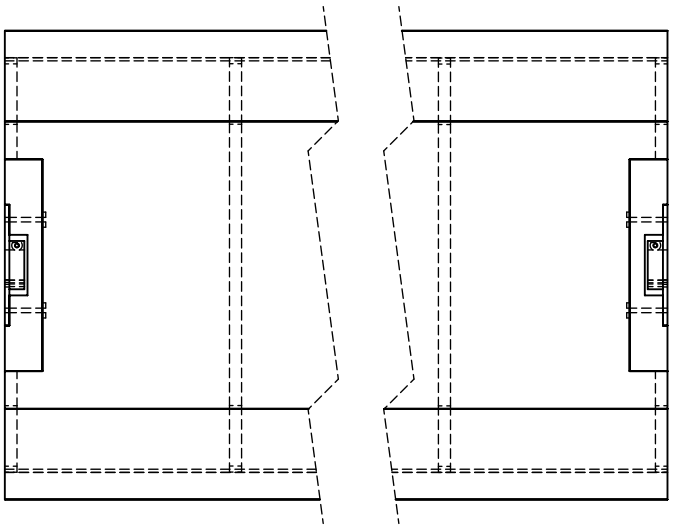

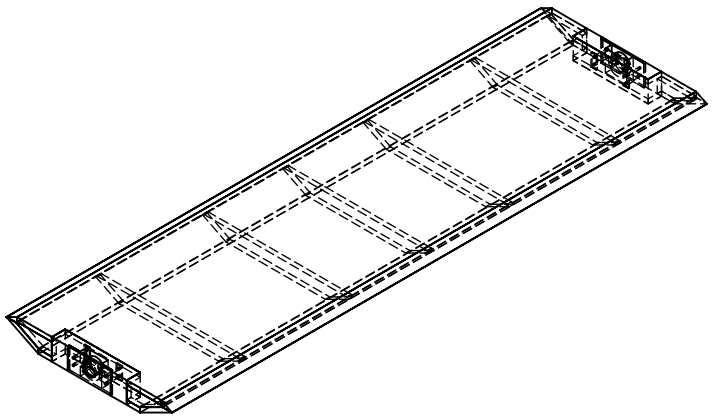

UNLESS OTHERWISE SPECIFIED: DIMENSIONS ARE IN MILLIMETERS SURFACE FINISH: TOLERANCES: LINEAR: ANGULAR:	FINISH:	DEBURR AND BREAK SHARP EDGES	DO NOT SCALE DRAWING / REVISION

	NAME	SIGNATURE	DATE
DRAWN			
CHK'D			
APPV'D			
MFG			
Q.A			

TITLE:

MATERIAL:

DWG NO. Great Belt Bridge

A4

WEIGHT:

SCALE:1:5

SHEET 1 OF 1

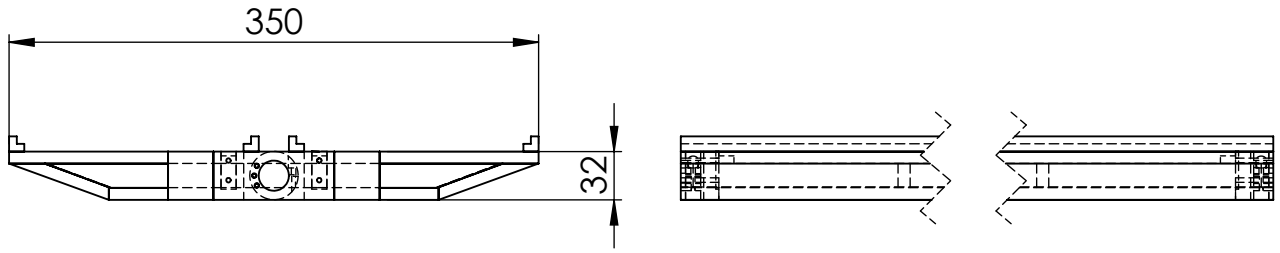

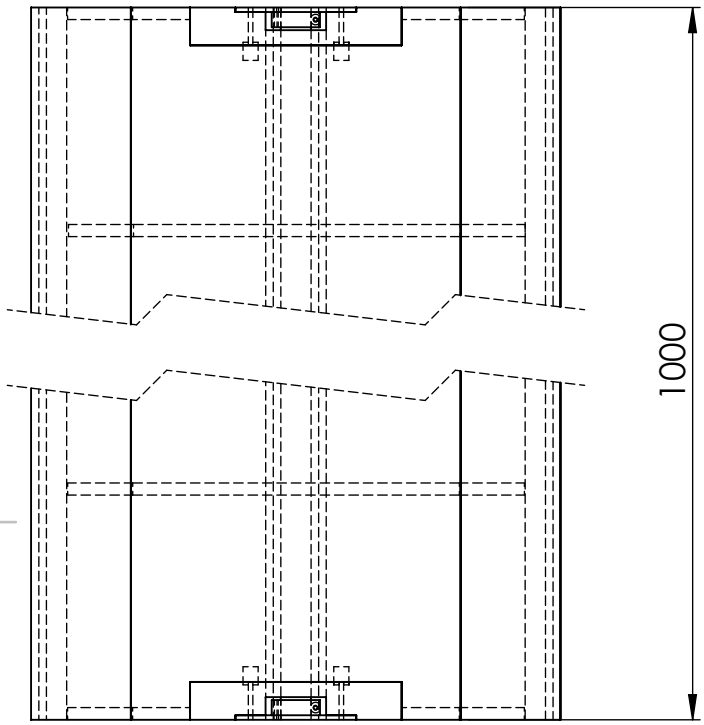

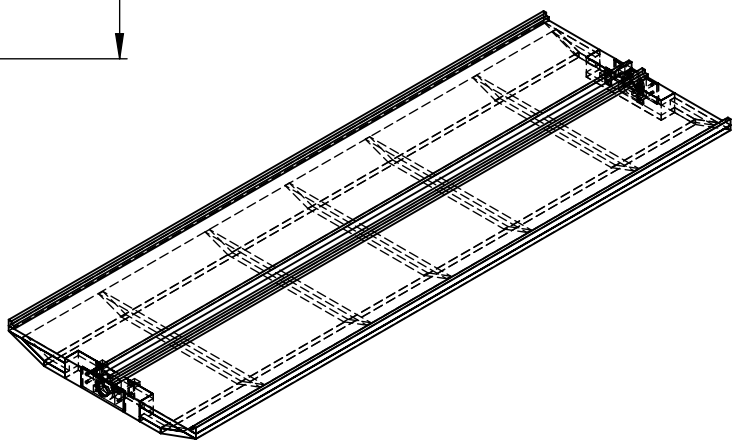

UNLESS OTHERWISE SPECIFIED: DIMENSIONS ARE IN MILLIMETERS SURFACE FINISH: TOLERANCES: LINEAR: ANGULAR:	FINISH:	DEBURR AND BREAK SHARP EDGES	DO NOT SCALE DRAWING / REVISION

	NAME	SIGNATURE	DATE
DRAWN			
CHK'D			
APPV'D			
MFG			
Q.A			

TITLE:

MATERIAL:

DWG NO. Kao Pin Hsi Bridge

A4

WEIGHT:

SCALE:1:5

SHEET 1 OF 1

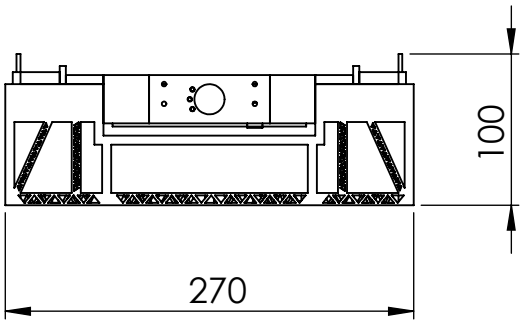

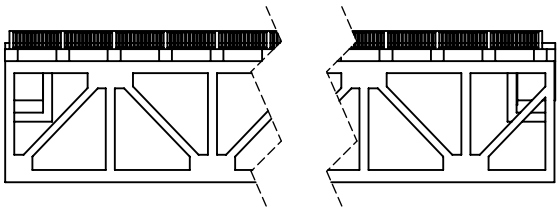

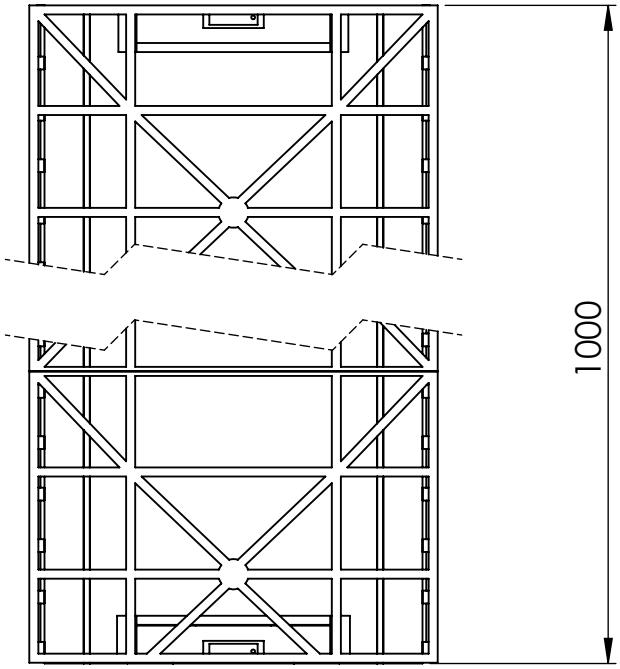

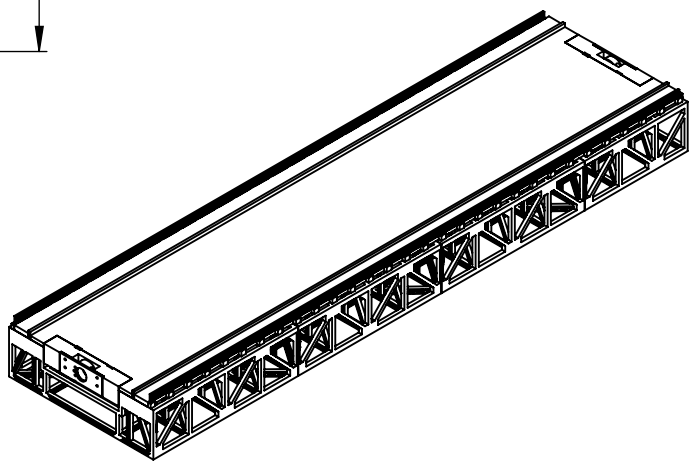

UNLESS OTHERWISE SPECIFIED: DIMENSIONS ARE IN MILLIMETERS SURFACE FINISH: TOLERANCES: LINEAR: ANGULAR:	FINISH:		DEBURR AND BREAK SHARP EDGES	DO NOT SCALE DRAWING	REVISION		
	NAME	SIGNATURE	DATE				TITLE:
DRAWN							
CHK'D							
APPV'D							
MFG							
Q.A				MATERIAL:			DWG NO. Golden Gate Bridge
							A4
				WEIGHT:		SCALE:1:5	SHEET 1 OF 1

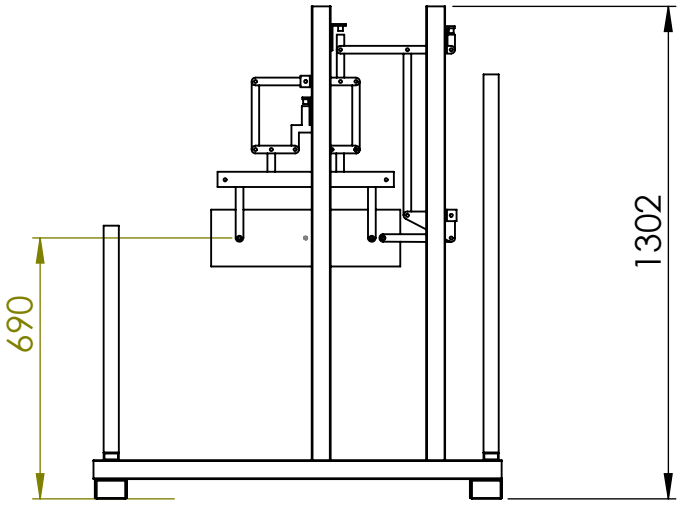

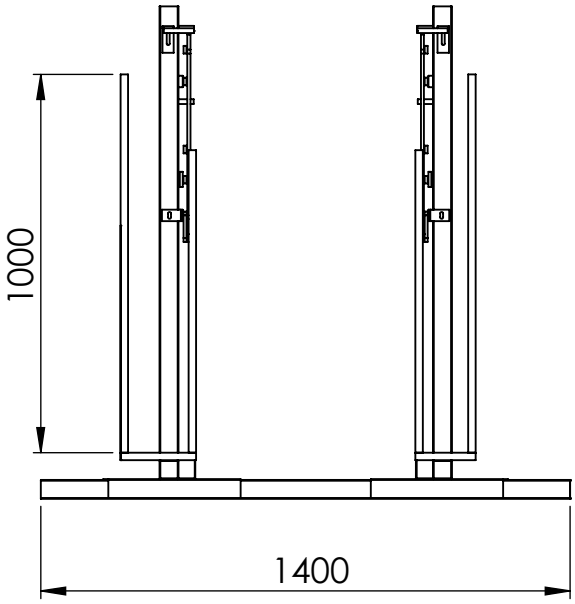

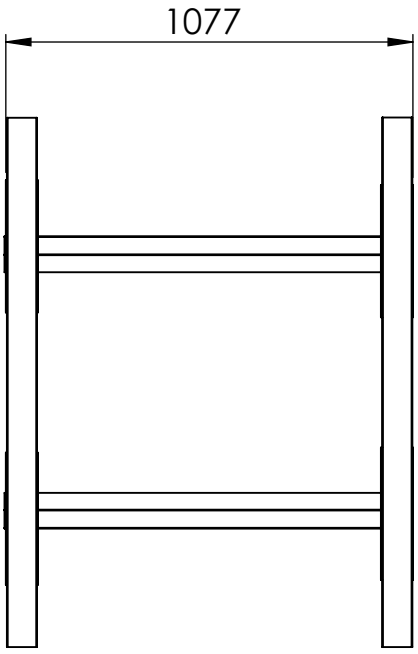

UNLESS OTHERWISE SPECIFIED: DIMENSIONS ARE IN MILLIMETERS SURFACE FINISH: TOLERANCES: LINEAR: ANGULAR:	FINISH:	DEBURR AND BREAK SHARP EDGES	DO NOT SCALE DRAWING / REVISION

	NAME	SIGNATURE	DATE
DRAWN			
CHK'D			
APPV'D			
MFG			
Q.A			

TITLE:

MATERIAL:

DWG NO. Force balance

A4

WEIGHT:

SCALE:1:20

SHEET 1 OF 1

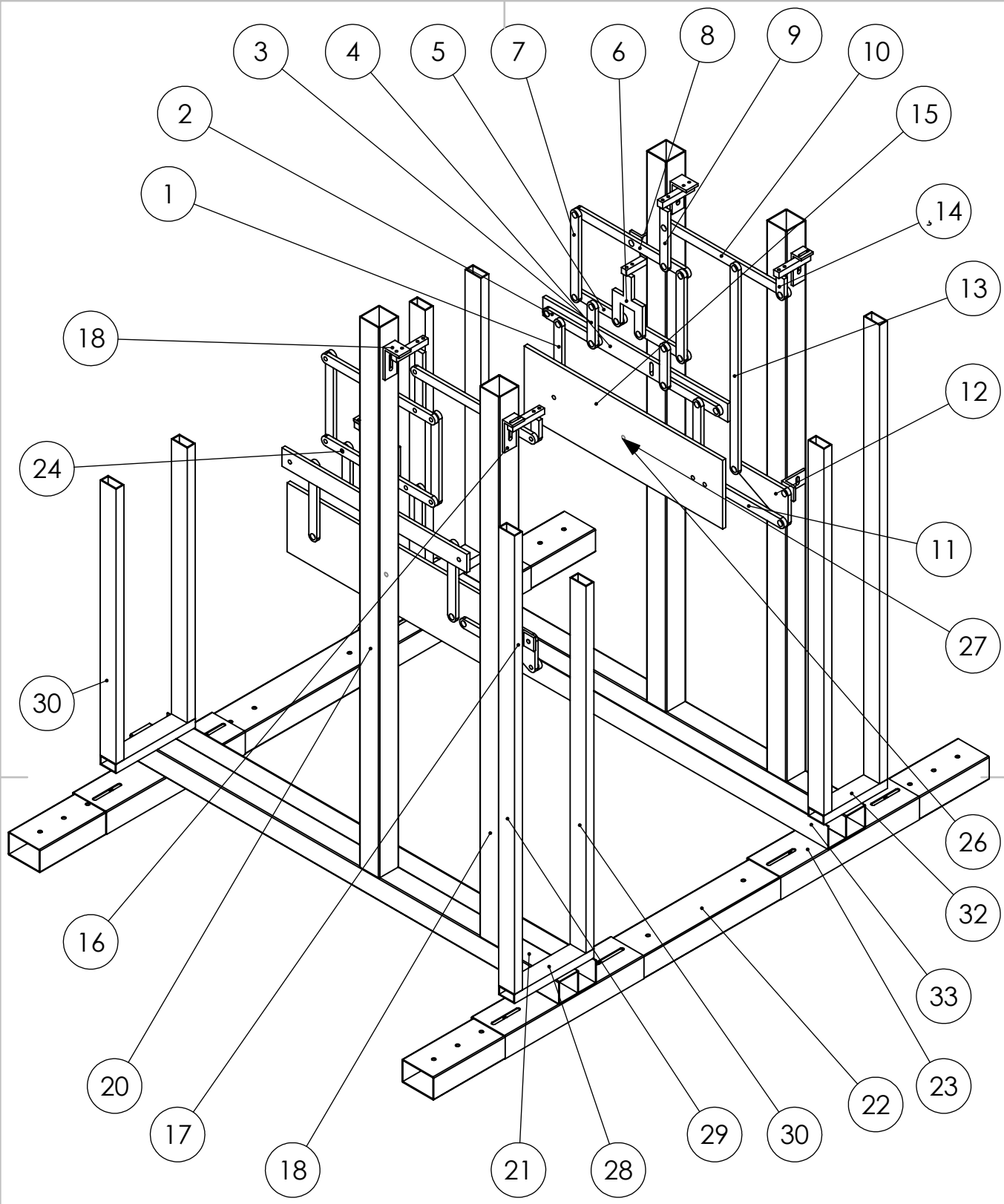

UNLESS OTHERWISE SPECIFIED: DIMENSIONS ARE IN MILLIMETERS SURFACE FINISH: TOLERANCES: LINEAR: ANGULAR:	FINISH:	DEBURR AND BREAK SHARP EDGES	DO NOT SCALE DRAWING / REVISION

	NAME	SIGNATURE	DATE
DRAWN			
CHK'D			
APPV'D			
MFG			
Q.A			

TITLE:

MATERIAL:

DWG NO. Force balance mechanism

A4

WEIGHT:

SCALE:1:20

SHEET 1 OF 2

ITEM NO.	PART NAME	DRAWING NUMBER	QTY.
1	Alu_beam_Part1	000-001	4
2	Alu_beam_Part2	000-002	4
3	Alu_beam_Part3	000-003	4
4	Fixing_Part4	000-004	2
5	Alu_beam_Part5	000-005	4
6	Alu_beam_Part6	000-006	2
7	Alu_beam_Part7	000-007	4
8	Alu_beam_Part8	000-008	2
9	Alu_beam_Part9	000-009	2
10	Alu_beam_Part11	000-011	2
11	Alu_beam_Part12	000-012	2
12	Alu_beam_Part13	000-013	2
13	Alu_beam_Part14	000-014	2
14	Alu_beam_Part15	000-015	2
15	Steel_mount_Part16	000-016	4
16	Steel_mount_Part17	000-017	4
17	Steel_mount_Part18	000-018	2
18	Steel_beam_Part19	000-019	2
19	Steel_beam_Part20	000-020	2
20	Steel_beam_Part21	000-021	2
21	Steel_beam_Part22	000-022	2
22	Steel_mount_Part23	000-023	4
23	Moving_joint_Part24	000-024	36
24	Fixing_joint_Part24	000-025	14
25	Bridge_mount_Part26	000-026	2
26	Bridge_mount_Part27	000-027	2
27	Steel_beam_Part28	000-028	2
29	Steel_beam_Part29	000-029	2
29	Steel_beam_Part30	000-030	2
30	Steel_beam_Part31	000-031	4
31	Steel_beam_Part32	000-032	2
32	Steel_beam_Part33	000-033	2

UNLESS OTHERWISE SPECIFIED:
DIMENSIONS ARE IN MILLIMETERS
SURFACE FINISH:
TOLERANCES:
LINEAR:
ANGULAR:

FINISH:

DEBURR AND BREAK SHARP EDGES

DO NOT SCALE DRAWING

REVISION

	NAME	SIGNATURE	DATE
DRAWN			
CHK'D			
APPV'D			
MFG			
Q.A			

TITLE:

MATERIAL:

DWG NO. Force balance mechanism

A4

WEIGHT:

SCALE:1:20

SHEET 2 OF 2